

---

Electronic Thesis and Dissertation Repository

---

9-11-2020 12:00 PM

## The development of bacterial magnetic resonance imaging for microbiota analyses

Sarah C. Donnelly, *The University of Western Ontario*

Supervisor: Burton, Jeremy P., *The University of Western Ontario*

Co-Supervisor: Goldhawk, Donna E., *The University of Western Ontario*

A thesis submitted in partial fulfillment of the requirements for the Master of Science degree in Microbiology and Immunology

© Sarah C. Donnelly 2020

Follow this and additional works at: <https://ir.lib.uwo.ca/etd>



Part of the [Bacteria Commons](#), [Medical Biophysics Commons](#), and the [Medical Microbiology Commons](#)

---

### Recommended Citation

Donnelly, Sarah C., "The development of bacterial magnetic resonance imaging for microbiota analyses" (2020). *Electronic Thesis and Dissertation Repository*. 7381.

<https://ir.lib.uwo.ca/etd/7381>

This Dissertation/Thesis is brought to you for free and open access by Scholarship@Western. It has been accepted for inclusion in Electronic Thesis and Dissertation Repository by an authorized administrator of Scholarship@Western. For more information, please contact [wlsadmin@uwo.ca](mailto:wlsadmin@uwo.ca).

## **Abstract**

Current microbial analyses to assess either the commensal microbiota or microorganism infection and disease typically require *ex vivo* techniques that risk contamination and are not undertaken in real time. The possibilities for employing imaging techniques in the microbiology field is becoming more prominent as studies expand on the use of positron emission tomography, ultrasound and numerous microscopy techniques. However, magnetic resonance imaging (MRI), a non-invasive *in vivo* modality that can produce real-time results is falling behind. Here, we examined the feasibility of detecting bacteria using clinical field strength MRI. Commensal, probiotic and uropathogenic *Escherichia coli* were scanned by 3 Tesla MRI where signal was related to the number of colony-forming units as well as total cellular iron and manganese content as determined by mass spectrometry. Various microbes commonly found in the human gut and urogenital tract were also assessed by MRI. *Lactobacillus* spp. displayed significantly higher transverse relaxation rates than other species, despite their low iron usage, potentially due to high manganese content. High MR relaxivity may enable detection of lactobacilli amidst host tissues, therefore, we assessed the potential to distinguish the MR signatures of two distinct cell types within mixed samples. With clinical field strength MRI, we were able to detect as few as  $\sim 26 \times 10^6$  colony-forming units of *Lactobacillus crispatus* ATCC33820 per  $\text{mm}^3$ . In the future, MRI may allow for non-invasive evaluation of health or dysbiosis in the human microbiota as well as potential applications in tracking the dispersion and persistence of bacteria in broad applications from probiotic use, infection to tumour tracking.

## **Keywords**

Magnetic resonance imaging (MRI), bacterial detection, bacterial tracking, iron homeostasis, manganese homeostasis, microbiota, urinary tract infection, *E. coli*, *Lactobacillus crispatus*, MagA

## **Summary (lay abstract)**

Background: Bacteria inhabit various niches throughout the human body. These bacteria can promote health, but in some cases specific bacteria can overgrow and be harmful to the host. We would like to use magnetic resonance imaging (MRI) to visualize and track these bacteria within their preferred environments to learn more about human-bacterial and bacterial-bacterial interactions in health and disease.

Hypotheses: Different bacterial types will appear differently on images from MRI. Adding the iron uptake gene *magA* to *E. coli* will make it easier to detect by MRI.

Methods: We imaged various bacteria and strains of *E. coli* found in the human gut and urogenital tract using MRI. We then cloned a gene (*magA*) which incorporates magnetic properties into an *E. coli* strain and then assessed its influence on bacterial MRI detection. We measured the concentrations of iron and manganese in all our bacteria since these metals can impact MRI. Finally, we imaged dilutions of *Lactobacillus crispatus*, a bacterium that we found to be very visible by MRI and mixed it with human bladder cells to see if we could distinguish the two cell types within a mixed sample.

Results and Significance: Different *E. coli* strains and bacteria have unique magnetic resonance signatures due to differences in metal content. In the future we hope to use MRI to identify and track bacteria within the human host.

## **Co-Authorship Statement**

All portions of this thesis were exclusively written by S. C. Donnelly with advice and editing from D. E. Goldhawk, J. P. Burton and N. Gelman. In Chapter 2, *magA* was cloned into pET28a<sup>+</sup> by R. S. Flannagan. D. E. Heinrichs provided *Staphylococcus aureus* iron acquisition mutants and bacterial iron handling and cloning expertise. N. Gelman and F. S. Prato provided software and expertise on magnetic resonance physics. K. Quiaoit prepared the pcDNA3.1MycHisA<sup>+</sup>/*Ha-magA* construct.

## **Acknowledgments**

I would like to thank everyone who has helped along the way in completing my M.Sc. and throughout my educational career. Therefore, I would like to briefly acknowledge some of the people who helped me achieve this academic milestone.

First, I would like to thank my supervisors Dr. Jeremy Burton and Dr. Donna Goldhawk. Jeremy, thank you for always doing your best to keep my research moving forward and reminding me to look at the big picture. Donna, thank you for always answering my questions and helping me think through unexpected results. Thank you both for your patience, support and guidance along the way.

Next, I would like to thank my advisory committee, Dr. David Heinrichs and Dr. Neil Gelman for all the advice and resources you have provided me to help in my study. Dr. Heinrichs, thank you for providing me with the iron acquisition mutants to help expand my study. Neil, thank you for helping me through the physics portions of my project and for always contributing to the discussion when I obtained unexpected results.

I would also like to thank the members of the Burton, Goldhawk and Reid labs (past and present) who have helped to create a great environment to conduct research. Thanks for your advice on my research, and for suggesting alternative methods various experiments, I truly appreciate it. Thank you to Dr. Ron Flannagan for his advice, technical expertise and helping troubleshoot when I experienced cloning difficulties. I'd like to thank Dr. Frank Prato and Dr. Gregor Reid for their out of the box ideas and constant feedback on how to improve my research. Shannon Seney, thank you for always being around to answer my questions, train me on new techniques and keep the lab running smoothly. Thanks to Praveen Dassanayake, Daisy Sun, Emiley Watson, Scarlett Puebla Barragán, Hannah Wilcox, Johnny Chmiel and many others in the lab who have acted as my sounding boards and made research life more enjoyable. Many thanks to John Butler, Heather Biernaski, Lynn Keenlside and Jeff Warner for their technical assistance during this project.

Finally, thank you to my family and my husband for their unconditional love and support throughout my life. Mike, thank you for always being around to cheer me up. Thank you for

being understanding and driving me to and from the lab at all hours when I had to start or induce a culture or move a partially solidified phantom to the fridge. Thank you for pretending to listen to me explain my project and new findings as well as practicing for presentations. Overall, thank you for believing in me and always being there to listen, support and encourage me; I could not have achieved this without you!

# **Table of Contents**

<u>Abstract</u> .....	ii
<u>Lay Abstract</u> .....	iii
<u>Co-Authorship Statement</u> .....	iv
<u>Acknowledgments</u> .....	v
<u>Table of Contents</u> .....	vii
<u>List of Tables</u> .....	xi
<u>List of Figures</u> .....	xii
<u>List of Appendices</u> .....	xiv
<u>List of Abbreviations</u> .....	xvi
<u>Chapter 1: Introduction</u> .....	1
<u>1.1 Bacteriology</u> .....	1
1.1.1 Human microbiota .....	1
1.1.2 Urinary tract infection .....	2
1.1.3 Bacterial metal homeostasis .....	3
<u>1.2 Imaging applications in bacteriology</u> .....	5
1.2.1 Advanced microscopy techniques in microbiome research .....	5
1.2.2 Bioluminescence and bacteria .....	6
1.2.3 Bacterial tracking via ultrasound .....	6
1.2.4 Positron emission tomography applications in microbiology .....	7

1.2.5 Bacteriology and magnetic resonance imaging .....	10
<u>1.3 Magnetic resonance imaging</u> .....	13
1.3.1 Sequences .....	16
1.3.2 Effect of metals and contrast enhancement on MRI .....	17
1.3.3 Magnetosomes, MagA and their applications in molecular imaging .....	18
<u>1.4 Rationale</u> .....	21
<u>1.5 Hypotheses</u> .....	22
<u>1.6 Objectives</u> .....	22
<u>1.7 References</u> .....	23
<u>Chapter 2: Characterizing the magnetic resonance signal in different <i>Escherichia coli</i> strains with and without MagA expression</u> .....	30
<u>2.1 Introduction</u> .....	30
<u>2.2 Methods</u> .....	32
2.2.1 Reagents .....	32
2.2.2 Bacterial strains and culture conditions .....	32
2.2.3 Cloning .....	34
2.2.4 Magnetic resonance imaging .....	41
2.2.5 Protein preparation and quantification .....	47
2.2.6 Inductively-coupled plasma mass spectrometry .....	47
2.2.7 Examining MagA expression .....	48



2.2.8 Statistical analyses .....	49
<u>2.3 Results</u> .....	50
2.3.1 MR relaxation rates of <i>E. coli</i> BL21(DE3) .....	50
2.3.2 MR relaxation rates of various <i>E. coli</i> strains .....	53
2.3.3 Fe and Mn quantification in <i>E. coli</i> strains .....	56
2.3.4 Correlation between metal content and MR measures in <i>E. coli</i> strains .....	58
2.3.5 MagA expression in <i>E. coli</i> BL21(DE3) .....	61
2.3.6 Effect of MagA expression in <i>E. coli</i> BL21(DE3) on MR measures and content of metal ions .....	64
<u>2.4 Discussion</u> .....	69
<u>2.5 Conclusions</u> .....	72
<u>2.6 References</u> .....	72
<u>Chapter 3: Characterizing the magnetic resonance signal of urinary isolates including <i>Lactobacillus crispatus</i></u> .....	77
<u>3.1 Introduction</u> .....	77
<u>3.2 Methods</u> .....	80
3.2.1 Reagents .....	80
3.2.2 Bacterial strains and culture conditions .....	80
3.2.3 Tissue culture conditions .....	81
3.2.4 Magnetic resonance imaging .....	81
3.2.5 Protein preparation and quantification .....	86

3.2.6 Inductively-coupled plasma mass spectrometry .....	86
3.2.7 Statistical analyses .....	86
<u>3.3 Results</u> .....	87
3.3.1 MR relaxation rates of commensal, probiotic and pathogenic bacteria of the urogenital tract .....	87
3.3.2 Fe and Mn quantification in various bacterial species .....	91
3.3.3 Measuring MR relaxivity of <i>L. crispatus</i> ATCC33820 .....	94
3.3.4 MRI signal from mixtures of human bladder cells and <i>L. crispatus</i> .....	101
3.3.5 Effect of iron acquisition mutations on MR relaxation rates and cellular iron and manganese content .....	108
<u>3.4 Discussion</u> .....	112
<u>3.5 Conclusions</u> .....	115
<u>3.6 References</u> .....	116
<u>Chapter 4: Summary</u> .....	122
4.1 <u>Summary</u> .....	122
4.2 <u>Future Directions</u> .....	124
4.3 <u>References</u> .....	125
<u>Appendices</u> .....	128
<u>Curriculum Vitae</u> .....	155

## **List of Tables**

Table 1. Potential for imaging modalities in bacteriology .....	12
Table 2. <i>E. coli</i> strains assessed in this study using MRI .....	33
Table 3. pET28a <sup>+</sup> /HA-magA-myc cloning primers .....	36
Table 4. pET28a <sup>+</sup> /HA-magA-myc sequencing primers .....	40
Table 5. Longitudinal relaxation rates of <i>E. coli</i> strains .....	55
Table 6. Pearson correlation of <i>E. coli</i> R2 measurements with iron, manganese, strain and classification. ....	59
Table 7. Pearson correlation of <i>E. coli</i> R2* measurements with iron, manganese, strain and classification .....	60
Table 8. Longitudinal relaxation rates for various bacterial species .....	90
Table 9. Longitudinal relaxation rates for serially diluted <i>L. crispatus</i> ATCC33820 .....	97
Table 10. Longitudinal relaxation rates of mixed samples of 5637 bladder cell and <i>L. crispatus</i> ATCC33820.....	104
Table 11. R2/R2* ratios for <i>L. crispatus</i> ATCC33820 dilutions.....	107
Table 12. Longitudinal relaxation rates for <i>S. aureus</i> USA300 and iron acquisition mutants .....	110

## **List of Figures**

Figure 1: Effect of MRI on magnetization.....	15
Figure 2: Vector map of pcDNA3.1 <i>MycHisA</i> <sup>+</sup> / <i>HA-magA</i> .....	35
Figure 3: pET28a <sup>+</sup> / <i>HA-magA-myc</i> vector map .....	39
Figure 4: MRI cell phantom.....	43
Figure 5: Workflow for MR phantom preparation .....	44
Figure 6: Representative slice and MR image .....	46
Figure 7: <i>E. coli</i> BL21(DE3) display high transverse relaxivity .....	51
Figure 8: Relaxation rates of BL21(DE3) packed into wells at different relative centrifugal forces.....	52
Figure 9: <i>Escherichia coli</i> are detectable by MRI .....	54
Figure 10: Content of iron and manganese varies between <i>E. coli</i> strains .....	57
Figure 11: Diagnostic digests of pET28a <sup>+</sup> / <i>HA-magA-myc</i> compared to empty vector .....	62
Figure 12: Western blot of MagA expression in <i>E. coli</i> BL21(DE3) .....	63
Figure 13: MagA expression does not improve MR detection of <i>E. coli</i> BL21(DE3) and diminishes cell viability .....	66
Figure 14: Manganese, but not iron content varies in MagA-expressing <i>E. coli</i> BL21(DE3) .....	68
Figure 15: Representative slice and MR image .....	84
Figure 16: MR measurements of different bacterial species vary widely .....	88
Figure 17: Elemental iron and manganese content vary widely between bacterial species ...	92

Figure 18: Transverse relaxivity of serially diluted <i>L. crispatus</i> ATCC33820 .....	96
Figure 19: MR measures of <i>L. crispatus</i> ATCC33820 are moderately correlated to number of live cells .....	98
Figure 20: MR measures vs. fraction of cells (f) for serially diluted <i>L. crispatus</i> ATCC33820 .....	99
Figure 21: Percent of <i>L. crispatus</i> ATCC33820 cells (f) are moderately correlated to number of live cells .....	100
Figure 22: Signal intensity decays mono-exponentially with echo time (TE) in mixed samples of 5637 bladder cells and <i>L. crispatus</i> ATCC33820.....	102
Figure 23: Transverse relaxation rates in serial dilutions of 5637 bladder cells and <i>L. crispatus</i> ATCC33820.....	103
Figure 24: Transverse relaxivity vs. fraction of bacterial cells (f) for <i>L. crispatus</i> ATCC33820 serially diluted in 5637 bladder cells .....	105
Figure 25: R2* and R2 vs. fraction of bacterial cells (f) for <i>L. crispatus</i> ATCC33820 serially diluted in 5637 bladder cells or gelatin.....	106
Figure 26: Transverse relaxation rates for <i>S. aureus</i> USA300 iron mutants grown under iron-replete and iron depleted conditions .....	109
Figure 27: Iron and manganese content in <i>S. aureus</i> USA300 iron acquisition mutants grown in iron depleted conditions .....	111

## **List of Appendices**

Appendix 1: Impact of bacterial growth media on MR measures .....	128
Appendix 2: Total cellular iron and manganese do not reliably predict transverse relaxivity .....	129
Appendix 3: Amplified <i>HA-magA-myc</i> .....	130
Appendix 4: Qualitative differential protein expression following induction of MagA expression in <i>E. coli</i> BL21(DE3).....	131
Appendix 5: Longitudinal relaxation rates for MagA expressing <i>E. coli</i> BL21(DE3).....	132
Appendix 6: Representative transverse relaxation decay curves for <i>L. crispatus</i> ATCC33820 diluted in gelatin .....	133
Appendix 7: Transverse and longitudinal relaxation rates for washed or unwashed <i>E. coli</i> BL21(DE3) .....	134
Appendix 8: Transverse and longitudinal relaxation rates of <i>E. coli</i> strains .....	135
Appendix 9: ICP-MS iron and manganese content of <i>E. coli</i> strains .....	138
Appendix 10: Transverse and longitudinal relaxation rates of MagA-expressing <i>E. coli</i> BL21(DE3) .....	140
Appendix 11: ICP-MS iron and manganese content of MagA-expressing <i>E. coli</i> BL21(DE3) .....	142
Appendix 12: Transverse and longitudinal relaxation rates of various bacterial species .....	143
Appendix 13: ICP-MS iron and manganese content of various bacterial species .....	146
Appendix 14: Transverse and longitudinal relaxation rates of <i>L. crispatus</i> ATCC33820 diluted in gelatin.....	148

Appendix 15: Transverse relaxation rates of *L. crispatus* ATCC33820 diluted in 5637 bladder cells ..... 150

Appendix 16: Transverse and longitudinal relaxation rates of *S. aureus* USA300 iron acquisition and storage mutants in iron-replete and iron-deplete growth conditions..... 152

Appendix 17: ICP-MS iron and manganese content of *S. aureus* USA300 iron acquisition and storage mutants in iron-replete and iron-deplete growth conditions ..... 154

## List of Abbreviations

ABC	ATP-binding cassette
ANOVA	Analysis of variance
B <sub>0</sub>	Main MR magnetic field
BCA	Bicinchoninic acid assay
BHI	Brain-heart infusion broth
BLI	Bioluminescence imaging
CFUs	Colony-forming units
[ <sup>18</sup> F]-FDG	[ <sup>18</sup> F]fluoro-deoxyglucose
FISH	Fluorescence in situ hybridization
FOV	Field of view
<i>fnA</i>	Ferritin A
Fur	Ferric uptake regulator
GRE	Gradient echo
HA	Hemagglutinin
ICP-MS	Inductively-coupled plasma mass spectrometry
IPTG	Isopropyl-β-D-thiogalactopyranoside
IR	Inversion recovery
LB	Lysogeny broth
<i>magA</i>	Putative iron transport gene
MAI	Magnetosome genomic island
MALDI-TOF IMS	Matrix-assisted laser desorption ionization-time of flight imaging mass spectrometry
MR	Magnetic resonance
MRI	Magnetic resonance imaging
MRS	deMan, Rogosa and Sharpe broth
MTB	Magnetotactic bacteria



M.W.	Molecular weight
NMR	Nuclear magnetic resonance
OD <sub>600</sub>	Optical density at 600 nm
PCR	Polymerase chain reaction
PBS	Phosphate-buffered saline
PET	Positron emission tomography
R1	Longitudinal relaxation rate
R2*	Transverse relaxation rate
R2	Irreversible component of transverse relaxation rate
R2'	Reversible component of transverse relaxation rate
RF	Radiofrequency
RIPA	Radioimmunoprecipitation assay buffer
ROI	Region of interest
<i>sbn</i>	Siderophore biosynthesis operon; Staphyloferrin B
SD	Standard deviation
SDS-PAGE	Sodium dodecyl sulfate-polyacrylamide gel electrophoresis
SE	Spin echo
SEM	Standard error of the mean
<i>sfa</i>	Staphyloferrin A
spp.	Species
SUV	Standardized uptake value
T	Tesla
T1	Longitudinal relaxation time
T2*	Transverse relaxation time
T2	Irreversible component of transverse relaxation time
T2'	Reversible component of transverse relaxation time
TE	Echo time
TR	Repetition time

TI	Inversion time
UPEC	Uropathogenic <i>E. coli</i>
US	Ultrasound
UTE	Ultrashort echo time
UTI	Urinary tract infection
WT	Wildtype

# **Chapter 1: Introduction**

## **1.1 Bacteriology**

### **1.1.1 Human microbiota**

Bacterial-host interactions are important, but probably none more so or more complex than the human microbiome-human relationship. The microbiome has now been shown to have numerous roles, including protecting us from pathogens, producing metabolites for energy and playing a major part of our homeostasis, amongst other functions<sup>1</sup>. Microbiome research has flourished over the last decade as researchers uncovered the multitude of roles that gut bacteria play in host pathways. Although much has been elucidated, there is still much to learn in terms of bacterial dispersion, interactions, and growth *in vivo* that may contribute to the maintenance of a healthy microbiome, and, in some cases, disease. The launch of the Human Microbiome Project led to a shift to high-throughput technologies, providing easier and faster identification of microbes and the roles they play in the microbiome<sup>2</sup>, but these samples are still being removed from their niche for analysis and these complex microbiome interactions are difficult to replicate outside of the host<sup>1</sup>. Currently, *ex vivo* analyses are necessary to explore how the microbial imbalances may alter host signaling pathways to cause disease or dysbiosis<sup>2</sup>. Yet, *in vivo* microbiome analyses would be beneficial to complement current *ex vivo* analyses and to elucidate the factors involved in disease manifestation and progression.

### **Urinary bacterial communities**

The bladder and urinary tract were previously thought to be sterile in healthy individuals, but we now know that is untrue<sup>3</sup>. In healthy individuals, the lower urinary system is dominated by species of lactobacilli and most frequently, members of the *Lactobacillus crispatus* species. While the microbiota of the urinary system is more complex than the absence or presence of these commensal microbes in health or disease, it represents a much simpler microbiota to

commence studies with than that of other sites in the body, with lower microbial diversity and reasonable densities, enabling more rapid human studies in this area. Our study will focus mainly on the urinary microbiota as this niche will be an ideal starting point for *in vivo* bacterial detection by MRI. Not only will the low microbial diversity allow for more simple analysis of future *in vivo* microbial samples, but the lack of gas pockets and motion compared to other microenvironments (like the human gut) will be helpful for minimizing imaging artifacts.

Bacterial-host interactions, function, and the dispersion of microbes *in vivo* are not well-studied in disease, especially not in those where our model organism (*Escherichia coli*) is typically prevalent, such as urinary tract infection (UTI) or in the microbiome where it has a sustained presence. There is still much to learn in microbiome research, and complementing *ex vivo* analyses with *in vivo* imaging may be beneficial for observing the true nature of bacterial growth, dispersion, and behaviour.

### **1.1.2 Urinary tract infection**

Studies show that a significant portion of patients in hospitals require urinary catheters and over half of these patients will experience UTI<sup>4</sup>, especially in cases of long-term catheterization<sup>5</sup>. UTI recurrence is common and usually becomes chronic since biofilm formation allows the bacteria to become more resistant to antibiotics, host defenses and shearing forces, which in turn allow them to survive and re-colonize the urinary tract<sup>5</sup>. Differences in attachment between bacterial species and strains are prompted by catheter composition. Although many catheters are currently made of silicone, other materials and coatings are being studied to prevent bacterial attachment<sup>5</sup>. Other research has explored if there is an ideal antibiotic to delay biofilm formation on catheters and potential for flushing catheters with this antibiotic before insertion may minimize UTIs<sup>6</sup>.

Although *E. coli* are commonly found in the human gut as commensal microbiota, they are the most common culprits of urinary infection due to their tendency to form biofilms. When transitioning from a planktonic form to a biofilm-forming bacteria, the cells must change their gene expression, especially of their virulence factors<sup>4</sup> to promote adherence<sup>7</sup>. It is important to study *E. coli* behaviours and dispersion during planktonic growth as well as during and following biofilm production to elucidate new pathways that can be targeted by molecular imaging. These

changes in growth form may lead to differences in contrast by molecular imaging or help explain any unexpected results. Due to the interest in *E. coli*'s biofilm structure, researchers have undertaken various *ex vivo* studies using imaging techniques, including matrix-assisted laser desorption ionization-time of flight imaging mass spectrometry (MALDI-TOF IMS)<sup>7</sup> and magnetic resonance imaging (MRI)<sup>8</sup>.

In UTI, type I pili are important for adherence, but not necessary for biofilm formation, especially under anaerobic conditions, indicative that this virulence factor is temporally regulated during biofilm formation<sup>7</sup>. Hadjifrangiskou *et al.* (2012) reiterate the importance of type I pili, as well as flagella and curli (a bacterial protein that acts as an extracellular matrix) which are necessary but not sufficient for biofilm formation<sup>4</sup>, indicative that further examination of biofilm-associated genes is warranted. Some work has been done using nuclear magnetic resonance (NMR) to study biofilms *in situ*, particularly to observe metabolism in intact, live biofilms<sup>9</sup>. Another study of interest looked at substrate transport into biofilms through diffusion using NMR. Here they found that relaxation rates were reduced within the biofilm due to the relative immobility of fluids especially around the boundary of the biofilm<sup>8</sup>. The researchers were able to use these magnetic resonance (MR) measures to map the location of the biofilm's boundary, the biofilm thickness and area, as well as the diameter of the catheter's lumen where liquid is still able to flow and shearing stress by flow is active<sup>8</sup>. Overall, these methods may be useful for complementing the analysis of biofilm structure and composition by molecular imaging.

### **1.1.3 Bacterial metal homeostasis**

#### **Iron**

Iron uptake and storage is tightly regulated in *E. coli*; however, these regulatory mechanisms may be impacted by biofilm formation, bacteria-bacteria interactions, or bacteria-host interactions. *Escherichia coli* require approximately  $10^{-5} - 10^{-7}$  M iron to grow optimally, this works out to anywhere from  $10^5 - 10^6$  iron atoms per bacterial cell<sup>10</sup>. Like all prokaryotes, *E. coli* use ferritin proteins to store intracellular iron in a readily available form for use in metabolism while preventing the iron from interacting with reactive oxygen species and causing cell damage and toxicity<sup>11</sup>. These bacteria also produce bacterioferritins which act similarly to ferritins and

are commonly co-expressed<sup>11</sup>. Iron uptake in *E. coli* is tightly regulated through ferric uptake regulator (Fur): when Fur binds free iron, it responds by repressing the transcription of iron uptake genes<sup>11, 12</sup>. A previous study using Mossbauer microscopy found that intracellular iron in *E. coli* is stored in aggregates of ferritin, and soluble iron accounts for less than 1% of the total cellular iron<sup>13</sup>. The iron uptake and storage of these bacteria are important to keep in mind as we consider the possibility of labelling them for molecular imaging.

Though all *E. coli* are rod shaped, there is some strain to strain size variation<sup>14</sup> and even intrastrain size variation<sup>15</sup>. Differences in iron acquisition genes and metabolic needs of strains may explain variability in cellular iron content since, as discussed above, iron acquisition genes are virulence factors contributing to bacterial pathogenesis. For example, certain UPEC encode siderophores such as salmochelin and aerobactin on their pathogenicity islands to improve survival in low iron environments<sup>16</sup>. Although these high affinity, low molecular weight ferric chelators are more plentiful in pathogenic bacteria, many bacteria encode genes involved with active iron uptake to enable their survival in low iron environments. Gram negative bacteria use outer membrane receptors paired with periplasmic shuttling proteins and ATP-binding cassette (ABC) transporters in their inner membrane to facilitate the uptake of siderophore-acquired iron<sup>10</sup>. Gram positive bacteria use a similar ABC transporter tethered to their membrane via a lipoprotein<sup>17</sup>.

## Manganese

Iron and manganese uptake are linked in UPEC expressing the *sitABCD* operon within their pathogenicity island(s)<sup>18</sup>. The genes in this operon include those encoding iron and manganese uptake proteins that are regulated by transcription factors involved in the Fur system as well as the MntR manganese regulator<sup>19</sup>. The combined regulation of iron and manganese uptake and enormous genetic intrastrain variability supports the similarity in trends between iron and manganese content in UPEC strains, but not necessarily in the lab or commensal *E. coli* strains. Although manganese is not as crucial a cofactor for many bacteria, it can act as a substrate for some metalloproteins in iron deplete conditions<sup>20</sup>. However, manganese is unable to activate many metalloproteins, rendering them useless<sup>20</sup>. Manganese uptake is mediated by MntH, so to limit manganese import in high Mn conditions, manganese-bound MntR represses the

transcription of this importer<sup>20</sup>. Many bacteria also produce manganese efflux pumps, like MntP found in *E. coli*. MntS expression is also repressed by manganese-bound MntR and it has been suggested that when expressed, MntS may inhibit MntP, thereby decreasing Mn efflux and effectively increasing intracellular manganese content<sup>20</sup>.

While iron is critical in most bacteria, manganese is critical for the growth and survival of lactobacilli<sup>21</sup>. Manganese is an important cofactor for many enzymes in lactobacilli, including lactate dehydrogenase, RNA polymerase and xylose isomerase<sup>22</sup>.

Both the iron and manganese handling capabilities of different bacteria are important to consider when exploring the possible applications of imaging bacteria by MRI.

## **1.2 Imaging applications in bacteriology**

The use of molecular imaging techniques has vastly expanded over the last decade, with an emphasis on greater interdisciplinary use, extending into cancer research, cell biology and microbiology. Here, we highlight the various imaging applications in microbiology to date and how we can apply imaging more effectively in the future.

### **1.2.1 Advanced microscopy techniques in microbiome research**

Microscopy is one of the most broadly used techniques, however there are many different subtypes that can be used to visualize minute subcellular structures, through fluorescence microscopy and confocal microscopy. A recent study using fluorescence in situ hybridization (FISH)<sup>23</sup> to explore bacterial dispersion in the gut microbiome within gnotobiotic mice found that bacteria within the microbiota are very dynamic, with rapid turnover and cellular shedding preventing aggregations and homogeneous bacterial dispersion<sup>23</sup>. Earle *et al.* (2015) also used FISH to explore the factors that influence bacterial dispersion in the gut microbiome *in vivo*. Though their imaging was done after sacrificing their mice, their study was still important in defining the relationship between luminal mucus thickness and proximity of bacteria to the epithelium<sup>24</sup>. In their gnotobiotic mice, the group also found that presence of *Helicobacter pylori*

within the microbiota was correlated to increased mitotic figures and more proliferative, and potentially cancerous, gastric cells were commonly found around *H. pylori*. Finally, they were able to visualize a near homogeneous mixture of bacteria after allowing the community to stabilize, with few large bacterial clumps, but most clumping caused by *Bacteroides*<sup>24</sup>, commonly the most abundant genus within the human gut. These FISH studies are great tools for exploring bacterial dispersion and interactions combining both highly specific fluorescence imaging techniques with high resolution confocal technology. Current FISH studies are conducted post-mortem, but perhaps future technological advancements will enable live non-invasive imaging.

## **1.2.2 Bioluminescence and bacteria**

Bioluminescence imaging (BLI) studies are informative but applications are limited since infections are caused by non-bioluminescent bacteria<sup>25, 26</sup> and poor spatial resolution caused by light scattering. Nonetheless, imaging luciferase reporter genes is commonly used in small animals, including mouse studies tracking bacteria over the course of infection<sup>27</sup>. Rodea *et al.* (2017) used BLI to learn about enterotoxigenic *E. coli* pathogenicity and colonization. By constitutively expressing the luciferase operon in these pathogens, the group was able to visualize bacterial adherence and persistence in the murine colon over time though they expressed troubles with the poor penetration depth<sup>27</sup>. Merrit *et al.* (2016) did not encounter such issues as they used BLI to visualize the oral microbiota and biofilm formation, where penetration depth is negligible. Here they expressed luciferase genes in several common oral *Streptococcus* spp., quantifying as anywhere from  $10^2$  -  $10^4$  CFUs<sup>28</sup>, demonstrating the great sensitivity of this technique.

## **1.2.3 Bacterial tracking via ultrasound**

Few studies are exploring the applications for US in bacteriology. Shapiro *et al.* (2014) examined the potential for gas vesicles to provide photoacoustic contrast using purified gas vesicles from two distinct bacterial sources. They found a 3.7 - 4.5-fold increase in US contrast in comparison to a linear scattering reference material<sup>29</sup>. This was followed up by Bourdeau *et al.* (2018) genetically engineered *E. coli* to express acoustic reporter genes in the form gas vesicle genes



from *Bacillus megaterium*. Once expressing these genes, the *E. coli* were injected into the lumen of a murine colon, followed by photoacoustic (US) imaging and BLI to track the bacteria *in vivo*.<sup>30</sup> As few as  $5 \times 10^7$  cells/mL could be detected, which they calculated to approximately 100 bacterial cells per voxel. Finally, they assessed their acoustic reporter genes in *Salmonella typhimurium* for future tumour tracking applications and were able to track the bacterial cells by US, but not BLI<sup>30</sup>, suggesting US may be superior to BLI for some applications.

US has also been applied to biofilm studies, with researchers causing gas bubble build up on biofilm surfaces to improve their detection<sup>31</sup>. Gas vesicles bound to TRITC-labelled streptavidin bound to biofilm surfaces proportionally to the size of the biofilm. They suggest that their technology could be used to detect both early- and late-stage biofilm formation *in vivo*<sup>31</sup>. These findings would be interesting to apply to urological studies where many UTIs and catheter or stent fouling is caused by biofilm formation.

## **1.2.4 Positron emission tomography applications in microbiology**

Positron emission tomography is a highly specific method that uses radionuclides to detect tissues or molecules of interest, generally through receptor mediated interactions. Recently, this modality has been the most widely explored for interdisciplinary bacteriology applications. The most common clinically relevant PET tracer is [18F]fluoro-deoxyglucose ([<sup>18</sup>F]-FDG), a glucose analog that enters cells, becomes phosphorylated and trapped, leading to <sup>18</sup>F accumulation within the cell, which can then be measured. More metabolically active cells – including cancer cells or proliferating immune cells – take up more of the tracer than background tissues, leading to a higher standardized uptake value (SUV). PET is becoming increasingly useful in microbiological studies to detect sites of inflammation or infection, to follow bacterial localization *in vivo*, and more recently to explore the gut microbiota. For example, Garrido et al. (2014) used [<sup>18</sup>F]-FDG to monitor infection and treatment of *Staphylococcus aureus* biofilms *in vivo* in catheters implanted subcutaneously in mice<sup>26</sup>. Here, they detected an increase in tracer uptake (or SUV) following infection and decreased SUV following treatment with rifampin, but they found that they were unable to distinguish the signal from bacteria compared to inflammatory cells<sup>26</sup>. This brings to question whether [<sup>18</sup>F]-FDG is the proper probe for detecting bacteria. In 2017, Heuker et al. also evaluated the potential to use [<sup>18</sup>F]-FDG to detect live bacterial infections<sup>32</sup>. This in

in vitro study used a variety of Gram-positive and Gram-negative bacterial isolates incubated with the radiotracer and assessed uptake with microPET and by using a gamma-counter. They found differences in uptake between bacterial species as well as differences in rates of uptake, where *Streptococcus pyogenes* displayed the highest tracer uptake. They also determined that viable bacteria were able to take up more tracer than heat-killed bacteria<sup>32</sup>, but they did not take into account the inflammatory cells that would be present *in vivo* and that other groups already showed contribute significantly to [<sup>18</sup>F]-FDG uptake. Since [<sup>18</sup>F]-FDG is not bacteria-specific, Mills et al. (2015) used a phosphorylated form, [<sup>18</sup>F]-fluorodeoxyglucose-6-phosphate ([<sup>18</sup>F]-FDG-6-P) that was shown to enter Gram-positive and Gram-negative bacteria through universal hexose phosphate transporters (UHPTs) that are not present in mammalian cells<sup>33</sup>. This radiotracer results in more specific uptake at sites of infection over sites of inflammation alone (hereby referred to as sterile inflammation). The authors used *S. aureus* UHPT-deficient mutants to confirm the necessity of UHPT for tracer uptake as well as to confirm that various mammalian cells were unable to transport the probe across their lipid bilayer. They found less [<sup>18</sup>F]-FDG-6-P uptake in mammalian cells compared to [<sup>18</sup>F]-FDG, producing a lower background signal with this new probe and higher SUV ratio in infected vs. uninfected mouse flanks<sup>33</sup>. This study also used a bioluminescent *S. aureus* strain for their mouse studies to verify their PET data<sup>33</sup>. Although [<sup>18</sup>F]-FDG-6-P was not taken up by any of the cancer cell lines they evaluated, there is a possibility for tracer uptake by mammalian cells<sup>33</sup>, thereby limiting the probe's utility for bacterial-specific uptake and due to its potential homing to sites of sterile inflammation.

Earlier studies aiming to image infection mostly targeted immune cells rather than the microbes themselves. In 1990, Fischmann et al. prepared pentetic acid (DTPA) bound chemotactic peptide analogs radiolabeled with <sup>111</sup>I<sup>34</sup>. These probes were able to bind chemokine receptors on human innate immune cells and reveal localization at the site of infection as immune cells migrated toward their target<sup>34</sup>. The main issue with these probes, as discussed earlier, is their inability to distinguish infection from inflammation alone, leading to a push for microbe-specific probe generation. Early bacteria-targeting studies evaluated probes such as 1-(2'-deoxy-2'-fluoro-β-D-arabinofuranosyl)-5-[<sup>125</sup>I] iodouracil ([<sup>125</sup>I]FIAU)<sup>35</sup> and [<sup>18</sup>F]-2'-Fluoro-2'-deoxy 1h-D-arabionofuranosyl-5-ethyl-uracil ([<sup>18</sup>F]FEAU)<sup>36</sup>. In 2005, Bettegowda et al. assessed the single-photon emission computed tomography (SPECT) probe [<sup>125</sup>I]FIAU in murine *E. coli* infections and found that it could be used to detect both Gram-positive and Gram-negative bacterial

species. They also used *Clostridium novyi*-NT intravenous infusion in mice along with the radiotracer to visualize tumours by SPECT<sup>35</sup>. A more recent study using [<sup>125</sup>I]FIAU to look at lung infections found that although the tracer uptake was specific to infection over sterile inflammation, the sensitivity was quite low<sup>37</sup>. Pullambhatla et al (2012) could only visualize bacterial burdens above 10<sup>9</sup> CFUs/mL<sup>37</sup>, 1000 – 10,000-fold higher than the threshold for bacterial infection. Brader et al. (2008) compared [<sup>18</sup>F]FEAU to both [<sup>18</sup>F]-FDG and [<sup>125</sup>I]FIAU to image *E. coli* Nissle 1917 localization to tumour sites<sup>36</sup>. They found a linear correlation between [<sup>18</sup>F]FEAU accumulation and the number of viable bacteria, however [<sup>18</sup>F]-FDG showed more accumulation at the tumour site (where *E. coli* were present). Although the background signal for both [<sup>18</sup>F]FEAU and [<sup>125</sup>I]FIAU were better than for [<sup>18</sup>F]-FDG<sup>36</sup>, there are currently much better options as new radiotracers are being produced.

In the search for a better bacterial-specific PET tracer, Ning et al. (2014) produced a new probe, <sup>18</sup>F labelled maltohexaose (MH18F), that targets the maltodextrin transporter present on all bacteria<sup>38</sup>. This new probe was able to detect as few as 10<sup>5</sup> CFUs of *E. coli*, resulting in a more sensitive method of imaging bacteria *in vivo* for detecting earlier stages of infection. In general, 10<sup>5</sup> – 10<sup>6</sup> CFUs/mL of bacteria are considered the threshold for infection. Researchers showed that MH18F produced a 30-fold increase in SUV in infected tissues compared to uninfected tissues, whereas [<sup>18</sup>F]-FDG only produced a 1.5-fold difference<sup>38</sup>, demonstrating the added utility of a bacteria-specific probe for microbial imaging. There was also a significantly decreased SUV in sodium azide-treated (non-metabolically active) bacteria compared to healthy bacteria<sup>38</sup>. Gowrishankar et al. (2014) used a similar novel PET tracer, 6-[<sup>18</sup>F]-fluoromaltose, that was also able to enter bacteria through the maltodextrin transporter<sup>39</sup>. This study also found that the maltodextrin-based probes are specific to bacteria, both Gram-negative and Gram-positive, but unable to be taken up by tumour cell lines. They also found that macrophage-internalized *Listeria monocytogenes* was unable to take up the tracer until it became extracellular again. SUV was increased significantly *in vivo* in a mouse *E. coli* induced myositis model compared to uninfected controls, and SUV was only increased in live bacteria, not in the heat-killed controls<sup>39</sup>. No changes were seen in sterile inflammation compared to uninfected mice as well as little gut accumulation, providing lower background signal. The 6-[<sup>18</sup>F]-fluoromaltose probe was

deemed sensitive to  $10^6$  CFUs<sup>39</sup>, meaning it is slightly less sensitive than the MH18F probe, but still able to detect the clinical threshold for most infections.

More recently, Neumann et al. (2017) evaluated different PET probes that take advantage of the amino acids specific to bacterial peptidoglycan synthesis. They found that [<sup>14</sup>C] D-Met was the best candidate for bacterial targeting since both Gram-positive and Gram-negative bacteria incorporate it selectively over the L-Met enantiomer<sup>40</sup>. The transpeptidases that use D-Met as a substrate for peptidoglycan synthesis are promiscuous and allow radionuclides to be incorporated without slowing down cell wall synthesis. Neumann et al. found that [<sup>14</sup>C] D-Met was not taken up by heat-killed bacteria or in a model of sterile inflammation, but SUV was much higher in *E. coli* or *S. aureus* murine myositis models<sup>40</sup>. High background in the respiratory and gastrointestinal tracts limits the utility for monitoring infections in these areas<sup>40</sup>, however it may be useful to image the microbiota in those areas to learn more about those bacterial interactions and activities.

## 1.2.5 Bacteriology and magnetic resonance imaging

In a bacterial MRI study, the researchers were able to define the boundaries of biofilms using T2-weighted MR images<sup>8</sup>. Hill et al. (2011) also used MRI to explore iron loading in planktonic *E. coli* Nissle through overexpression of iron storage proteins including ferritin and bacterioferritin. Here they found both in vitro and in vivo that increased iron storage leads to higher iron uptake – possibly by siderophores – and increased R2 relaxivity<sup>41</sup>. One weakness of the study was use of a 7T MRI system which is not currently approved for clinical use. We propose that further advances can be exploited by using MRI at 3T to obtain more clinically relevant data and provide ease in translation from the lab to the clinic.

Hoerr et al. (2013) wanted to label *S. aureus* cells with iron oxide nanoparticles to monitor infection. They started by labelling *E. coli* where the negatively charged lipopolysaccharide on the bacterial outer membrane enabled easy labelling with the positively charged nanoparticle<sup>42</sup>. *In vitro* MRI at 9.4T was performed at various time points post-labelling to assess dilution of the label. This label dilution was important for tracking infection over time in their *in vivo* mouse model. For labelled *S. aureus*, a blooming artifact was evident in T2\*-weighted images<sup>42</sup> due to

local field inhomogeneities. Overall in this study they were able to reliably detect  $10^5$  CFUs<sup>42</sup>, right at clinically relevant bacterial levels.

**Table 1. Potential for imaging modalities in bacteriology**

Modality	Resolution	Potential applications	Benefits	Limitations	References
MRI	1 mm	<ul style="list-style-type: none"> <li>Tracking iron-labelled bacteria, or those with high MR relaxivity</li> <li>Multimodality imaging</li> </ul>	<ul style="list-style-type: none"> <li>Non-invasive</li> <li>High sensitivity</li> <li>Potential for imaging bacteria without labelling</li> </ul>	<ul style="list-style-type: none"> <li>Low specificity</li> <li>Expensive</li> <li>Can be time consuming</li> </ul>	8, 41, 42
PET	3 – 5 mm	<ul style="list-style-type: none"> <li>Detection of specific bacterial species</li> <li>Multimodality imaging</li> </ul>	<ul style="list-style-type: none"> <li>Non-invasive</li> <li>High specificity and sensitivity</li> </ul>	<ul style="list-style-type: none"> <li>Require radioisotopes</li> <li>Must label target</li> <li>Expensive</li> </ul>	26, 32, 33, 35-37, 39, 40
US	0.1 mm	<ul style="list-style-type: none"> <li>Deep tissue bacterial tracking</li> </ul>	<ul style="list-style-type: none"> <li>Non-invasive</li> <li>Deep penetration depth</li> <li>High spatial resolution</li> <li>Accessible</li> </ul>	<ul style="list-style-type: none"> <li>Low specificity</li> <li>Requires bacterial labelling for good resolution</li> </ul>	29-31
FISH	< 1 mm	<ul style="list-style-type: none"> <li>Exploring bacterial interactions and dispersion</li> </ul>	<ul style="list-style-type: none"> <li>High specificity and sensitivity</li> </ul>	<ul style="list-style-type: none"> <li><i>Ex vivo</i></li> <li>Low penetration depth</li> <li>Require fluorescence labelling</li> </ul>	23, 24
BLI	> 5 mm	<ul style="list-style-type: none"> <li>Multimodality imaging</li> <li>Superficial bacterial detection and tracking <i>in vivo</i></li> </ul>	<ul style="list-style-type: none"> <li>High specificity</li> </ul>	<ul style="list-style-type: none"> <li>Target must express bioluminescence genes</li> <li>Superficial imaging only</li> </ul>	27, 28

### **1.3 Magnetic resonance imaging**

MRI uses magnetic fields and radiofrequency (RF) radiation to detect the magnetic moment of protons, a magnetic property that can be measured. Each proton has a magnetic moment. In the absence of a magnetic field, the direction of these magnetic moments are randomly distributed so there is no net magnetization produced<sup>43</sup>. An MRI scanner incorporates a large magnet that produces a magnetic field referred to as  $B_0$ . This  $B_0$  field is often aligned with the Z-direction of a coordinate system that is used to describe the process of image formation, where the XY-plane is perpendicular to the direction of the magnet bore. When placed in a magnetic field, the magnetic moment associated with the protons in tissues precesses around  $B_0$ , with the Z-component of the magnetic moment aligned either parallel or antiparallel to  $B_0$ . The parallel condition is slightly favoured leading to an overall net magnetization in the direction of  $B_0$ <sup>43</sup>. To produce an image this net magnetization is manipulated by a series of RF fields and magnetic field gradients. The RF fields rotate the net magnetization away from the Z-axis so that a component of the net magnetization lies in the XY plane. Linear magnetic field gradients can then be used to encode the position of protons within the sample to create an image<sup>43</sup>. After the application of the RF fields to perturb the magnetization, the proton magnetic moments take some time to return to their original distribution and alignment in the Z direction and for the coherence of the magnetization to decay within the XY-plane (Figure 1). The rate of realignment can vary depending on the environment of the proton. Examples of different proton environments would be water trapped in a cell and water in extracellular fluid.

The time for the net magnetization vector to return to its equilibrium state aligned with  $B_0$  is characterized by a time constant T1 that is called the longitudinal relaxation time constant. This time constant is affected by the energy exchange between protons with the surrounding magnetic and thermal environment. The loss of phase coherence of the transverse (XY) component of the magnetization is characterized by the transverse relaxation time constant, which represents the time to decay to 1/e of its initial value<sup>43</sup>. There are three different types of transverse relaxation, known as T2\*, T2 and T2', that will be discussed in this thesis. It is often convenient to refer to the associated relaxation rates ( $R_2 = 1/T_2$ ,  $R_2^* = 1/T_2^*$ ,  $R_2' = 1/T_2'$ ).  $R_2^*$  is the total transverse relaxation rate, and is equal to the sum of the other two rates ( $R_2^* = R_2 + R_2'$ .)  $R_2$  is often called the irreversible transverse relaxation rate because that part of the decay can not be reversed with

RF refocusing pulses (see spin-echo sequence below), whereas  $R2'$  is reversible. Transverse relaxation is especially impacted by magnetic field inhomogeneities from iron<sup>44</sup>. Clustering of magnetic nanoparticles causes a decrease in both  $R2$  and  $R2'$  relaxation as the magnetic particles generate local magnetic fields that cause the surrounding protons to dephase<sup>45</sup>. This means that the net magnetization in the XY-plane disappears faster than it would in the absence of iron. These measurements affected by iron labelling can be exploited for imaging bacteria *in vivo*. These relaxation rates, or relaxivity, increase with increased levels of iron.

Magnetic resonance imaging (MRI) is a non-invasive *in vivo* molecular imaging technique with high spatial resolution and depth of penetration, but it has poor specificity<sup>46</sup>. However, it is still one of the most frequently employed clinical imaging modalities since it does not require the use of radioisotopes<sup>46</sup>. The greater the magnetic field strength, the greater the resultant net magnetization vector within the sample because the number of protons with magnetic moments that align along  $B_0$  increases proportional to  $B_0$ .



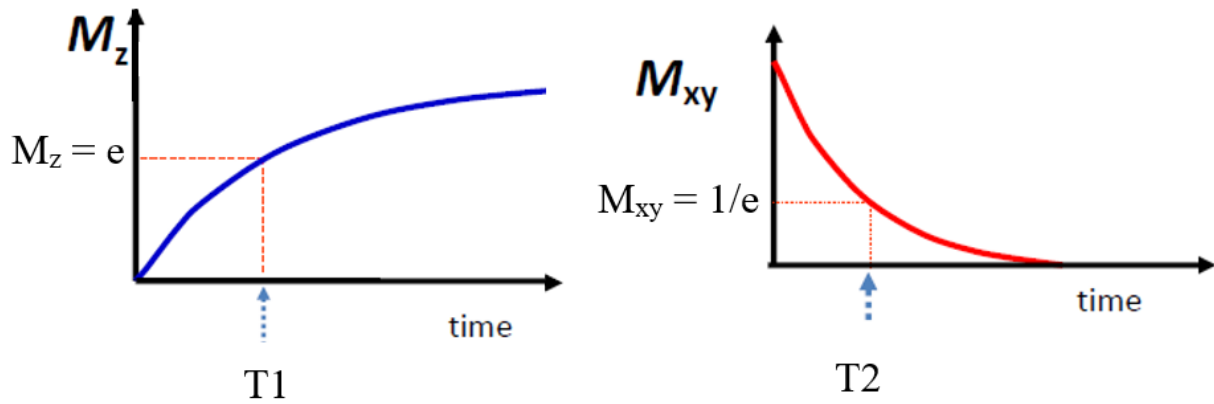


**Figure 1. Effect of MRI on magnetization.** Protons within a sample each have their own magnetic moment with no net magnetization vector. In the presence of the main magnetic field ( $B_0$ ) from an MRI most protons align parallel or antiparallel to the magnetic field, leading to a net magnetization vector in the direction of  $B_0$ . An RF pulse ( $B_1$ ) is applied perpendicular to  $B_0$  to tip the net magnetization vector into the XY plane and R1 and R2 decays are obtained as the magnetization in the Z-plane regrows ( $M_z$ ) and the XY component ( $M_{xy}$ ) decreases respectively.

## 1.3.1 Sequences

### Spin-echo sequence

Spin echo (SE) sequences use a  $90^\circ$  RF pulse to tip the net magnetization from its alignment along the Z axis (parallel to the main magnetic field,  $B_0$ ) into the XY plane. Next, a  $180^\circ$  pulse is applied at a time  $TE/2$  after the  $90^\circ$  RF pulse, where TE is the echo time. This  $180^\circ$  RF pulse rephases the spins that were aligned in different directions in the XY plane, due to magnetic field inhomogeneities. The signal acquisition occurs at a time  $TE/2$  after the  $180^\circ$  RF pulse, i.e., at a time TE after the  $90^\circ$  RF pulse. As TE increases the signal intensity decreases due to T2 relaxation, i.e., this is the irreversible decay. The pairs of  $90^\circ$  and  $180^\circ$  RF pulses are repeated while varying magnetic field gradients in a prescribed method to acquire a full image. The repetition time (TR) is the time between these  $90^\circ$  excitation RF pulses. As signal intensity is measured at varying TE, all signal intensities decrease as TE increases, but the rate of this signal decay varies, measured as R2. In SE images, the signal intensity is low in tissues with a short T2 and is comparably higher in tissues with a long T2. Fluids, which have long T2 (i.e., low R2), appear bright, whereas tissues, which are packed with cells, have high R2 and appear gray.

### Gradient echo sequence

Gradient echo (GRE) sequences use a single  $90^\circ$  excitation RF pulse in combination with magnetic field gradients to produce an echo. No refocusing pulses (i.e., no  $180^\circ$  pulse) are utilized. For the gradient echo, TE is the time from the RF pulse to the centre of the gradient echo. As with SE imaging, signal intensity decreases with longer TE, but the rate of signal decay varies. Signal decay as a function of TE is due to  $R2^*$  relaxation which includes both R2 relaxation and static dephasing associated with magnetic field inhomogeneities. Unlike R2,  $R2^*$  is not an intrinsic property of the tissue since any imperfections in the tissue composition, including the presence of nearby air spaces and metal ions can alter the rate of signal dephasing due to the generation of localized magnetic field gradients.

### Inversion-recovery sequence

Inversion recovery (IR) sequences can be used to obtain longitudinal relaxation rate measurements through the acquisition of T1-weighted images. In this sequence, a  $180^\circ$  RF pulse,

or an inversion pulse, inverts the longitudinal magnetization before applying the 90° excitation pulse. The inversion time (TI) refers to the time between these two pulses. The sequence is repeated with varying TI; there is little time for T1 signal recovery during short TI so the signal acquired is negative, whereas longer TI allow for T1 recovery and positive signal acquisition. These positive and negative echoes are plotted as IR curves to obtain R1 measurements. The proton density (or water content) of an imaged tissue impacts R1.

### **1.3.2 Effect of metals and contrast enhancement on MRI**

Magnetic metals, including ferro-, para- and diamagnetic ions cause local field inhomogeneities and enhance transverse relaxivity within a sample. Though many metals impact MRI, the effects of paramagnetic particles like manganese on MRI are orders of magnitude weaker than those of ferromagnetic (iron) particles<sup>47</sup>.

Magnetic resonance signals can be manipulated by using contrast agents, both exogenous or endogenous, to improve target specificity<sup>46</sup>. Exogenous contrast agents, such as superparamagnetic oxide nanoparticles (SPIO), are injected into the patient and shorten the rate of transverse relaxation. Endogenous agents are produced and expressed by the patient's cells and act similarly to exogenous agents, however, there are a few key advantages of endogenous contrast agents. Exogenous contrast agents dilute with cell division, are injected once and then degrade and dissipate from the target site. This causes decreased MR signal over time<sup>48</sup> and requires injections each time patients are scanned. Endogenous agents are replicated in each cell, passing the contrasting material onto daughter cells during mitosis. therefore the signal remains longitudinally<sup>46</sup> for long-term cell labelling. It is also possible to explore cellular activities when using endogenous agents since the cell must be alive to produce the contrast<sup>49</sup>. In addition, there is the potential for reporter-gene based expression, where contrast is measured when a specific cell signalling pathway becomes activated or when specific ligands are present. Overall, development of endogenous contrast agents is necessary for earlier detection and intervention in disease, especially in patients requiring repeat MRI sessions.

Iron-related contrast agents are popular for MRI as they affect transverse relaxation rates, including R2, R2\*, and R2' <sup>50</sup>. These MR measurements are impacted by magnetic field

inhomogeneities from iron<sup>44</sup>. Zhou *et al.* (2017) found that clustering of magnetic nanoparticles causes a decrease in T2 relaxation<sup>45</sup>. Since T2 is inversely proportional to R2, we see an increase in R2 measurements. These magnetic nanoparticles lead to generation of a local magnetic field which causes the surrounding protons to dephase<sup>45</sup>. These key measurements are affected by iron labelling, can be exploited for imaging bacteria *in vivo*, and are used in our study to quantitatively measure the effect of iron in bacteria.

Endogenous, gene-based agents for long-term contrast and the monitoring of cellular activities<sup>49</sup> has been previously demonstrated in mammalian cells by expressing single genes<sup>50</sup>, and in non-magnetic bacteria with full operons from magnetotactic bacteria (MTB)<sup>51</sup> to improve iron uptake and retention, thereby imparting MR contrast enhancement.

### **1.3.3 Magnetosomes, MagA and their applications in molecular imaging**

Magnetotactic bacteria are gram negative anaerobes that produce iron biomineral compartments, or magnetosomes, to impart magnetic properties and align along magnetic fields. These magnetosomes are produced in a protein-mediated stepwise manner starting with membrane invagination to form intracellular vesicles<sup>51</sup>. These magnetosome vesicles take up iron and biomineralize complex iron particles that vary based on the species of MTB. For example, *Magnetospirillum magneticum* sp. AMB-1 produce magnetite which is stored in magnetosome vesicles that assemble into chains along the cytoskeleton<sup>51</sup>. The proteins that permit this process to take place are well conserved between MTB species, and many are encoded on a distinct region of the genome termed the magnetosome genomic island (MAI). To determine which genes may be essential for magnetosome production, Kolinko *et al.* (2014) cloned full operons of the genes in non-magnetic bacteria. They speculated that only a subset of the MAI genes are required for magnetosome formation and that systematic analysis of each gene will help to uncover those that are necessary<sup>51</sup>. One of these potentially important magnetosome genes, *mamK*, has been cloned into *E. coli* and shown to play a role in positioning the magnetosomes along the cytoskeleton<sup>52</sup>. The idea of magnetosome gene regulation by induction may be useful in future studies to restrict any toxic effects that accompany iron retention. For example, Pradel *et al.* (2006) regulated *mamK*

gene expression using arabinose-mediated induction. A similar study cloning *mamK* into *E. coli* used isopropyl- $\beta$ -D-thiogalactopyranoside (IPTG) to induce the gene expression<sup>53</sup>.

A gene from AMB-1, *magA*, was previously characterized to encode a non-selective iron uptake protein<sup>54</sup>. This characterization involved cloning a strain of *E. coli* to express the gene in a bacterial expression plasmid. They found that MagA shared homology with KefC, a K<sup>+</sup> efflux pump in *E. coli*, however this homology did not reflect function. Instead, they found that MagA functioned as a membrane-bound ATP-dependent iron transporter. They further suggested that *magA* expression is regulated similarly to the Fur system in *E. coli*<sup>54</sup> since the sequence of Fur within *Magnetospirillum* MTB is well conserved and these sequences are quite similar in *M. magneticum* and *M. magnetotacticum*<sup>12</sup>. At the very least, Fur seems to be involved in iron homeostasis and the regulation of MTB biomineralization<sup>12</sup>. Another study found that *magA* expression was increased in iron deficient conditions but partially repressed in iron replete conditions<sup>55</sup>, suggesting the possibility for Fur-mediated regulation. These researchers also found through electron microscopy that MagA may interact with the magnetosome membrane<sup>55</sup>. A more recent study of *magA* found that the gene was not conserved in all MTB and was not located on the MAI<sup>56</sup>. These findings suggest that *magA* may not be important for magnetotaxis since *magA* deletion mutants showed no phenotypic effects and still produced magnetosomes, indicating that MagA is either not essential or not involved in magnetosome formation<sup>56</sup>.

Using magnetosomes for MR contrast enhancement may be advantageous over SPIO since they share similarities, including size, composition, and response to magnetic fields<sup>49</sup>. Biological magnetosomes tend to have more uniform crystal size as well as more even dispersion than their synthetic counterparts<sup>57</sup>. These differences may be attributed to the natural lipid bilayer that surrounds the magnetosomes. That lipid bilayer allows for a larger crystal to form, which seemingly provides better magnetic properties. To explore this further Hu *et al.* (2010) compared synthetic nanoparticles and biological magnetosomes in varying concentrations by proton NMR and analyzed the T1 and T2 effects. They saw increasing signal attenuation in both T1 and T2 weighted images with increasing magnetosome concentration, as expected. The signal decayed faster in samples of bacterial magnetosomes, which was attributed to increased inhomogeneities within the magnetic field<sup>57</sup> due to the presence of concentrated magnetite iron particles. The main shortcoming in this study was the lack of phantom for air exclusion to minimize artifacts. Also,

the FLAIR and fast SE sequences they used to acquire their MR data are very different from our own. That combined with the minimal quantitative data (mostly displayed as T1/T2 ratios) provide a barrier for direct comparison MR relaxivity of purified magnetosomes to that of the wildtype bacteria within our study. Other groups have found that increasing concentrations of magnetosomes lead to lower T2 *in vivo*, enabling labelling for up to 28 days<sup>46</sup>. This longitudinal labelling may aid in early diagnosis of disease as well as monitoring, or even theranostics<sup>46</sup>.

Single MTB genes like *magA*<sup>49, 58</sup> or *mms6*<sup>59</sup> have been employed to improve iron uptake/retention and impart magnetic properties and improve MR contrast. Full operons of MTB magnetosome genes have been cloned into a non-magnetic bacterium, *Rhodospirillum rubrum*, to elucidate their functions<sup>51</sup>. MagA expression in mammalian cells increases cellular iron and transverse (R2, R2\*) relaxivity<sup>48, 49</sup>. Though iron loading can be detrimental to cells, and toxicity has been noted following high levels of MagA induction in some mammalian cells<sup>48</sup> but not others<sup>49, 50</sup>, MagA-mediated toxicity in bacterial cells has yet to be reported and previous *E. coli* studies found no toxic effects<sup>54</sup>. A recent study used a lentivirus to provide inducible MR contrast by MagA for monitoring stem cell grafts longitudinally<sup>48</sup>. They observed cytotoxicity and reduced proliferation rates upon induction of MagA expression. Nonetheless, increases in cellular iron were measured following MagA expression which correlated to increased R2 *in vivo*<sup>48</sup>. The technique to induce MagA expression used by Cho *et al.* (2014) may be beneficial in pursuing MagA as an MRI reporter gene to minimize detrimental iron accumulation and control cytotoxicity, although this toxicity was not seen in other mammalian cell lines such as N2A<sup>49</sup>, or MDA-MB-435<sup>50</sup>. A study where adult stem cells were labelled with MagA found MagA-associated cytotoxicity in both mouse kidney stem/progenitor cells and mouse mesenchymal/stromal cells<sup>60</sup>. However, they did find that human embryonic kidney cells transduced with *magA* were viable, and as previously reported, showed MR relaxation rates correlated with iron content. They suggest that MagA as a reporter gene system may not be feasible for all cell types. Pereira *et al.* (2016) also proposed that magnetosome-like particles previously observed may simply be ferritin clusters which also have applications in MR contrast enhancement<sup>50</sup>. At 11 T, Goldhawk *et al.* (2009) saw increased R2 relaxation rates and cellular iron uptake following MagA expression, though they noted that varying levels of MagA expression may lead to inhomogeneities in the MR signal. They also found signal void and blooming effect using MR to image the gut of mice fed an iron supplement<sup>49</sup>. We suggest that these hypointensities may be due to iron uptake by enterocytes as well as countless

gut microbes. Transgenic MagA-expressing mice have also been produced, with MagA expression verified in various tissues along with the presence of intracellular magnetosome-like particles<sup>61</sup>. Their findings supported the previous studies with increased R2 measurements in the MagA-expressing transgenic mice<sup>61</sup>. Zurkiya *et al.* (2008) also found differences in 3-4 fold increases in MR transverse relaxation rates in MagA-expressing 293FT cells following iron supplementation<sup>58</sup>. If similar MR measurements were to be obtained in the context of our study, this would provide a great tool for imaging bacteria *in vivo*.

## **1.4 Rationale**

Bacteria-human interactions tend to have a negative connotation, however many of these relationships are symbiotic. The benefits of microbiome interactions are complex and difficult to replicate outside of the host<sup>1</sup>. In the gut, this dependency of bacteria on their host varies depending on diet and micro-environment, which in turn influences gene expression<sup>2</sup>, metabolism and signaling pathways, providing an explanation for how the microbiome plays a role in disease<sup>2</sup>. It would therefore be beneficial to have a system for observing these interactions *in situ*. Establishing fast and safe protocols for visualizing the healthy gut microbiome *in vivo* will help clarify which factors play a role in disease manifestation and progression and enable better tools for early detection and treatment of dysbiosis.

The current gold standard for gut microbiome investigation involves *ex vivo* analysis of microbial samples removed from the intestinal mucosa and attempts to propagate these *in vitro* for high-throughput analyses, such as 16S rRNA to identify microbes and their relative abundance. Nevertheless, *ex vivo* samples are prone to contamination or changes in bacterial growth that may misrepresent the original sample. In addition, many microbes depend on bacterial-host interactions to survive, requiring specific nutrients or atmospheric conditions. Although there are model systems, including the chemostat fermenter<sup>1</sup>, it is impossible to recreate the complexity of the microbiome *in vitro*, therefore; these models should be used as a tool to validate *in vivo* techniques.

We propose a complementary approach to *ex vivo* analyses, using *in vivo* imaging to observe bacterial growth, dispersion, and behaviour. Imaging also affords the potential for labeling bacteria

to improve sensitivity of detection. The research reported here provides a foundation for using MRI to image bacteria *in vivo*. Through this, we aim to foster a greater understanding of microbial behaviour, the microbiome, infection, and the personalized medicine required for early diagnosis and treatment of bacterial disease.

## **1.5 Hypotheses**

Firstly, we hypothesized that MR relaxation rates vary among bacterial strains and species.

Secondly, we hypothesized that MagA expression in *Escherichia coli* would increase cellular iron content and impart magnetic properties for cellular detection by MRI.

## **1.6 Objectives**

To explore differences in MR measures between bacterial strains, we examined the MR relaxation rates of nine *Escherichia coli* strains along with their iron and manganese contents using inductively-coupled plasma mass spectrometry (ICP-MS). We then evaluated the relationships between these parameters as well as trends between MR measures, metal content and strain classification.

To evaluate the effect of MagA expression on bacterial MR measures, we cloned epitope-tagged *magA* into an *E. coli* expression vector and transformed this MagA construct into *E. coli* BL21(DE3). MagA-expressing bacteria were assessed by immunoblotting to verify protein expression, by MRI to measure relaxation rates, and by ICP-MS to quantify total cellular iron and manganese content in the presence or absence of extracellular iron supplementation.

To assess interspecies variability in MR measures and metal content, we obtained MR measurements for various bacterial species found in the urogenital tract and gut microbiome, relating these to iron and manganese content. We then explored the effect of iron acquisition



mutants on MRI and bacterial metal content. We also assessed the feasibility of distinguishing MR signatures in mixed samples of human bladder cells and *Lactobacillus crispatus*.

## **1.7 References**

- [1] McDonald J. A. K., Schroete K., Fuentes S., Heikamp-deJong I., Khursigara C. M., de Vos W. M., and Allen-Vercoe E. (2013) Evaluation of microbial community reproducibility, stability and composition in a human distal gut chemostat model, *J Microbiol Methods* 95, 167–174.
- [2] Gao Y.-D., Zhao Y., and Huang J. (2014) Metabolic modeling of common *Escherichia coli* strains in human gut microbiome, *BioMed Res Int* v.2014, Article ID 694967.
- [3] Bao Y., Al K. F., Chanyi R. M., Whiteside S., Dewar M., Razvi H., Reid G., and Burton J. P. (2016) Questions and challenges associated with studying the microbiome of the urinary tract, *Annals of Translational Medicine* 5(2): 33.
- [4] Hadjifrangiskou M., Gu A. P., Pinkner J. S., Kostakioti M., Zhang E. W., Greene S. E., and Hultgren S. J. (2012) Transposon mutagenesis identifies uropathogenic *Escherichia coli* biofilm factors, *J Bacteriol* 194, 6195–6205.
- [5] Ferrières L., Hancock V., and Klemm P. (2007) Specific selection for virulent urinary tract infectious *Escherichia coli* strains during catheter-associated biofilm formation, *FEMS Immunol Med Microbiol* 51, 212-219.
- [6] Koseoglu H., Aslan G., Esen N., Sen B. H., and Coban H. (2006) Ultrastructural stages of biofilm development of *Escherichia coli* on urethral catheters and effects of antibiotics on biofilm formation, *Urology* 68, 942-946.
- [7] Floyd K. A., Moore J. L., Eberly A. R., Good J. A. D., Shaffer C. L., Zaver H., Almqvist F., Skaar E. P., Caprioli R. M., and Hadjifrangiskou M. (2015) Adhesive fiber stratification in uropathogenic *Escherichia coli* biofilms unveils oxygen-mediated control of type I pili, *PLoS Pathog* 11(3): e1004697.

- [8] Manz B., Volke F., Goll D., and Horn H. (2003) Measuring local flow velocities and biofilm structure in biofilm systems with magnetic resonance imaging (MRI), *Biotechnology and Bioengineering* 84, 424-432.
- [9] Majors P. D., McLean J. S., Pinchuk G. E., Fredrickson J. K., Gorby Y. A., Minard K. R., and Wind R. A. (2005) NMR methods for *in situ* biofilm metabolism studies, *J Microbiol Methods* 62, 337-344.
- [10] Andrews S. C., Robinson A. K., and Rodriguez-Quinones F. (2003) Bacterial iron homeostasis, *FEMS Microbiology Reviews* 27, 215-237.
- [11] Abdul-Tehrani H., Hudson A. J., Chang Y.-S., Timms A. R., Hawkins C., Williams J. M., Harrison P. M., Guest J. R., and Andrews S. C. (1999) Ferritin mutants of *Escherichia coli* are iron deficient and growth impaired, and fur mutants are iron deficient, *J Bacteriol* 181, 1415-1428.
- [12] Uebe R., Voigt B., Schweder T., Albrecht D., Katzmann E., Lang C., Bottger L., Matzanke B., and Schuler D. (2010) Deletion of a fur-Like gene affects iron homeostasis and magnetosome formation in *Magnetospirillum gryphiswaldense*, *J Bacteriol* 192, 4192–4204.
- [13] Bauminger E. R., Cohen S. G., Dickson D. P. E., Levy A., Ofer S. and Yariv J. (1980) Mossbauer spectroscopy of *Escherichia coli* and its iron-storage protein, *Biochim Biophys Acta* 623, 237-242.
- [14] El-Hajj Z. W., and Newman E. B. (2015) How much territory can a single *E. coli* cell control?, *Front Microbiol* 6 article 309.
- [15] Furchtgott L., Wingreen N. S., and Huang K. C. (2011) Mechanisms for maintaining cell shape in rod-shaped Gram negative bacteria, *Mol Microbiol* 81(2):340-353.
- [16] Gao Q., Wang X., Xu H., Xu Y., Ling J., Zhang D., Gao S. and Liu X. (2012) Roles of iron acquisition systems in virulence of extraintestinal pathogenic *Escherichia coli*: salmochelin and aerobactin contribute more to virulence than heme in a chicken infection model, *BMC microbiol* 12, 143-154.

- [17] Köster W. (2001) ABC transporter-mediated uptake of iron, siderophores, heme and vitamin B12, *Research in microbiology* 152, 291-301.
- [18] Subashchandrabose S., and Mobley H. L. T. (2015) Virulence and fitness determinants of uropathogenic *Escherichia coli*, *Microbiol Spectr* 3(4).
- [19] Ikeda J. S., Janakiraman A., Kehres D. G., Maguire M. E., and Slauch J. M. (2005) Transcriptional regulation of sitABCD of *Salmonella enterica* serovar *Typhimurium* by MntR and Fur, *J Bacteriol* 187, 912-922.
- [20] Martin J. E., Waters L. S., Storz G., and Imlay J. A. (2015) The *Escherichia coli* small protein MntS and exporter MntP optimize the intracellular concentration of manganese, *PLoS Genet* 11, e1004977.
- [21] Archibald F. (1983) *Lactobacillus plantarum*, an organism not requiring iron *FEMS Microbiol Lett* 19, 29-32.
- [22] Archibald F. (1986) Manganese: Its acquisition by and function in the lactic acid bacteria, *CRC Crit Rev Microbiol* 13, 63-109.
- [23] Welch J. L. M., Hasegawa Y., McNulty N. P., Gordon J. I., and Borisy G. G. (2017) Spatial organization of a model 15-member human gut microbiota established in gnotobiotic mice, *PNAS*, E9105–E9114.
- [24] Earle K. A., Billings G., Sigal M., Lichtman J. S., Hansson G. C., Elias J. E., Amieva M. R., Huang K. C., and Sonnenburg J. L. (2015) Quantitative imaging of gut microbiota spatial organization, *Cell Host Microbe* 18, 478-488.
- [25] Dinjaski N., Suri S., Valle J., Lehman S. M., Lasa I., Prieto M. A., and Garcia A. J. (2014) Near-infrared fluorescence imaging as an alternative to bioluminescent bacteria to monitor biomaterial-associated infections, *Acta biomaterialia* 10, 2935-2944.
- [26] Garrido V., Collantes M., Barberan M., Penuelas I., Arbizu J., Amorena B., and Grillo M. J. (2014) In vivo monitoring of *Staphylococcus aureus* biofilm infections and antimicrobial

- therapy by [<sup>18</sup>F]fluoro-deoxyglucose-MicroPET in a mouse model, *Antimicrobial agents and chemotherapy* 58, 6660-6667.
- [27] Rodea G. E., Montiel-Infante F. X., Cruz-Cordova A., Saldana-Ahuactzi Z., Ochoa S. A., Espinosa-Mazariego K., Hernandez-Castro R., and Xicohtencatl-Cortes J. (2017) Tracking bioluminescent ETEC during *in vivo* BALB/c mouse colonization, *Front cell infect microbiol* 7, article 187.
- [28] Merritt J., Senpuku H., and Kreth J. (2016) Let there be bioluminescence: development of a biophotonic imaging platform for in situ analyses of oral biofilms in animal models, *Environ microbiol* 18, 174-190.
- [29] Shapiro M. G., Goodwill P. W., Neogy A., Yin M., Foster F. S., Schaffer D. V., and Conolly S. M. (2014) Biogenic gas nanostructures as ultrasonic molecular reporters, *Nat nanotechnol* 9, 311-316.
- [30] Bourdeau R. W., Lee-Gosselin A., Lakshmanan A., Farhadi A., Kumar S.R., Nety S. P. and Shapiro M. G. (2018) Acoustic reporter genes for noninvasive imaging of microorganisms in mammalian hosts, *Nat Lett* 553, 86-92.
- [31] Anastasiadis P., Mojica K. D., Allen J. S., and Matter M. L. (2014) Detection and quantification of bacterial biofilms combining high-frequency acoustic microscopy and targeted lipid microparticles, *J nanobiotechnol* 12, 24; doi:10.1186/1477-3155-12-24.
- [32] Heuker M., Sijbesma J. W. A., Suarez R. A., de Jong J. R., Boersma H. H., Luurtsema G., Elsinga P. H., Glaudemans A., van Dam G. M., van Dijk J. M., Slart R., and van Oosten M. (2017) *In vitro* imaging of bacteria using (<sup>18</sup>F)-fluorodeoxyglucose micro positron emission tomography, *Sci Rep* 7, 4973; doi:10.1038/s41598-017-05403-z.
- [33] Mills B., Awais R. O., Luckett J., Turton D., Williams P., Perkins A. C., and Hill P. J. (2015) [<sup>18</sup>F]FDG-6-P as a novel *in vivo* tool for imaging staphylococcal infections, *EJNMMI research* 5, 13; doi:10.1186/s13550-015-0095-1.
- [34] Fischman A. J., Pike M. C., Kroon D., Fucello A. J., Rexinger D., tenKate C., Wilkinson R., Rubin R. H., and Strauss H. W. (1991) Imaging focal sites of bacterial infection in rats with indium-111-labeled chemotactic peptide analogs, *J nuc med* 32, 483-491.

- [35] Bettgowda C., Foss C. A., Cheong I., Wang Y., Diaz L., Agrawal N., Fox J., Dick J., Dang L. H., Zhou S., Kinzler K. W., Vogelstein B., and Pomper M. G. (2005) Imaging bacterial infections with radiolabeled 1-(2'-deoxy-2'-fluoro-beta-D-arabinofuranosyl)-5-iodouracil, *PNAS* 102, 1145-1150.
- [36] Brader P., Stritzker J., Riedl C. C., Zanzonico P., Cai S., Burnazi E. M., Ghani E. R., Hricak H., Szalay A. A., Fong Y., and Blasberg R. (2008) *Escherichia coli* Nissle 1917 facilitates tumor detection by positron emission tomography and optical imaging, *Clin Cancer Res* 14, 2295-2302.
- [37] Pullambhatla M., Tessier J., Beck G., Jedynek B., Wurthner J. U., and Pomper M. G. (2012) [<sup>125</sup>I]FIAU imaging in a preclinical model of lung infection: quantification of bacterial load, *Am J Nucl Med Mol Imag* 2, 260-270.
- [38] Ning X., Seo W., Lee S., Takemiya K., Rafi M., Feng X., Weiss D., Wang X., Williams L., Camp V. M., Eugene M., Taylor W. R., Goodman M., and Murthy N. (2014) PET imaging of bacterial infections with fluorine-18-labeled maltohexaose, *Angewandte Chemie (International ed. in English)* 53, 14096-14101.
- [39] Gowrishankar G., Namavari M., Jouannot E. B., Hoehne A., Reeves R., Hardy J., and Gambhir S. S. (2014) Investigation of 6-[(<sup>18</sup>F)]-fluoromaltose as a novel PET tracer for imaging bacterial infection, *PLoS One* 9, e107951.
- [40] Neumann K. D., Villanueva-Meyer J. E., Mutch C. A., Flavell R. R., Blecha J. E., Kwak T., Sriram R., VanBrocklin H. F., Rosenberg O. S., Ohliger M. A., and Wilson D. M. (2017) Imaging active infection *in vivo* using D-amino acid derived PET radiotracers, *Sci Rep* 7, 7903; doi:10.1038/s41598-017-08415-x.
- [41] Hill P. J., Stritzker J., Scadeng M., Geissinger U., Haddad D., Basse-Lusebrink T. C., Gbureck U., Jakob P., and Szalay A. A. (2011) Magnetic resonance imaging of tumors colonized with bacterial ferritin-expressing *Escherichia coli*, *PLoS ONE* 6(10): e25409.
- [42] Hoerr V., Tuchscher L., Huve J., Nippe N., Loser K., Glyvuk N., Tsytsyura Y., Holtkamp M., Sunderkotter C., Karst U., Klingauf J., Peters G., Loffler B., and Faber C. (2013) Bacteria tracking by *in vivo* magnetic resonance imaging, *BMC biology* 11, 63; doi:10.1186/1741-7007-11-63.

- [43] McRobbie D. W., Moore E. A., Graves M. J., and Prince M. R. (2006) *MRI from proton to picture*, 2nd ed., Cambridge University Press.
- [44] Lee C., Thompson R., Prato F., Goldhawk D., and Gelman N. (2015) Investigating the relationship between transverse relaxation rate (R2) and interecho time in MagA-expressing iron-labeled cells, *Mol Imag* 14, 551-560.
- [45] Zhou Z., Tian R., Wang Z., Yang Z., Liu Y., Liu G., Wang R., Gao J., Song J., Nie L., and Chen X. (2017) Artificial local magnetic field inhomogeneity enhances T2 relaxivity, *Nat Comm* 8, 15468; doi: 10.1038/ncomms15468.
- [46] Boucher M., Geffroy F., Preveral S., Bellanger L., Selingue E., Adryanczyk-Perrier G., Pean M., Lefevre C. T., Pignol D., Ginet N., and Meriaux S. (2017) Genetically tailored magnetosomes used as MRI probe for molecular imaging of brain tumor, *Biomaterials* 121, 167-178.
- [47] Ibrahim M. A., Gupta N., and Dublin A. B. (2020) Magnetic resonance imaging (MRI) gadolinium, in *StatPearls*; StatPearls Publishing, Treasure Island, FL, USA.
- [48] Cho I. K., Moran S. P., Paudyal R., Piotrowska-Nitsche K., Cheng P-H., Zhang X., Mao H., and Chan A. W. S. (2014) Longitudinal monitoring of stem cell grafts in vivo using magnetic resonance imaging with inducible MagA as a genetic reporter, *Theranostics* 4, 972-989.
- [49] Goldhawk D., Lemaire C., McCreary C., McGirr R., Dhanvantari S., Thompson R., Figueredo R., Koropatnick J. Foster P., and Prato F. (2009) Magnetic resonance imaging of cells overexpressing MagA, an endogenous contrast agent for live cell imaging, *Mol Imaging* 8, 129-139.
- [50] Sengupta A., Quiaoit K., Thompson R., Prato F., Gelman N., and Goldhawk D. (2014) Biophysical features of MagA expression in mammalian cells: implications for MRI contrast, *Front Microbiol* 5 article 29.
- [51] Kolinko I., Lohße A., Borg S., Raschdorf O., Jogler C., Tu Q., Posfai M., Tompa E., Plitzko J. M., Brachmann A., Wanner G., Muller R., Zhang Y., and Schuler D. (2014) Biosynthesis of magnetic nanostructures in a foreign organism by transfer of bacterial magnetosome gene clusters, *Nat Nanotechnol* 9, 193-197.

- [52] Pradel N., Santini C.-L., Bernadac A., Fukumori Y, and Wu L.-F. (2006) Biogenesis of actin-like bacterial cytoskeletal filaments destined for positioning prokaryotic magnetic organelles, *PNAS* *103*, 17485-17489.
- [53] Taoka A., Asada R., Wu L.-F., and Fukumori Y. (2007) Polymerization of the actin-like protein MamK, which is associated with magnetosomes, *J Bacteriol* *189*, 8737–8740.
- [54] Nakamura C., Burgess J. G., Sode K., and Matsunaga T. (1995) An iron-regulated gene, *magA*, encoding an iron transport protein of *Magnetospirillum* sp. strain AMB-1, *J Biol Chem* *270*, 28392–28396.
- [55] Nakamura C., Kikuchi T., Burgess J. G., and Matsunaga T. (1995) Iron-regulated expression and membrane localization of the MagA protein in *Magnetospirillum* sp. strain AMB-1, *J Biochem* *118*, 23-27.
- [56] Uebe R., Henn S., and Schuler D. (2012) The MagA protein of *Magnetospirilla* is not involved in bacterial magnetite biomineralization, *J Bacteriol* *194*, 1018-1023.
- [57] Hu L. L., Zhang F., Wang Z., You X. F., Nie L., Wang H. X., Song T., and Yang W. H. (2010) Comparison of the <sup>1</sup>H NMR relaxation enhancement produced by bacterial magnetosomes and synthetic iron oxide nanoparticles for potential use as MR molecular probes, *IEEE Transactions on Applied Superconductivity* *20*, 822-825.
- [58] Zurkiya O., Chan A. W., and Hu X. (2008) MagA is sufficient for producing magnetic nanoparticles in mammalian cells, making it an MRI reporter, *Magn Reson Med* *59*, 1225–1231.
- [59] Zhang X.-Y., Robledo B. N., Harris S. S., and Hu X. P. (2014) A bacterial gene, *mms6*, as a new reporter gene for magnetic resonance imaging of mammalian cells, *Mol Imaging* *13*, 1-12.
- [60] Pereira S. M., Williams S. R., Murray P., and Taylor A. (2016) MS-1 *magA*: Revisiting Its efficacy as a reporter gene for MRI, *Mol Imaging* *15*, 1-9.
- [61] Guan X., Jiang X., Yang C, Tian X., and Li L. (2015) The MRI marker gene *MagA* attenuates the oxidative damage induced by iron overload in transgenic mice, *Nanotoxicology* *10*, 531-541.

## **Chapter 2: Characterizing the magnetic resonance signal in different *Escherichia coli* strains with and without MagA expression**

### **2.1 Introduction**

*Escherichia coli* are gram negative, rod-shaped bacteria that commonly make up a relatively small percentage (approximately 0.1%) of the human gut microbiota<sup>1</sup>. Although *E. coli* only constitute a small portion of the microbial colonization, Gao *et al.* found that at least one or more strains of *E. coli* were present in each of the 148 human gut samples examined<sup>1</sup>, suggesting that *E. coli* are an integral component of the gut microbiome in most, if not all humans. *Escherichia coli* strains are not only important commensals in the human gut, but some are also pathogenic, causing major diarrheal, renal and other illnesses from intestinal invasion. In addition, *E. coli* is responsible for more than 80% of all urinary tract infections (UTIs), which are the most frequent infection in humans<sup>2</sup>. UTI recurrence can lead to chronic infection as well since *E. coli* can form and establish within biofilms, allowing the bacteria to become increasingly resistant to antibiotics, host defenses and shearing forces, thus promoting pathogen survival and colonization of the urinary tract<sup>3</sup>. Differential gene expression during biofilm formation may promote adherence to biological and abiotic surfaces<sup>4</sup>; however, some virulence factors that improve bacterial pathogenesis like type I pili and flagella are not crucial for biofilm formation<sup>4, 5</sup>.

The ability of *E. coli* to acquire certain metal cofactors, such as iron, can also be considered a form of bacterial pathogenesis<sup>6</sup>. Iron uptake and storage is tightly regulated in *E. coli* and these regulatory mechanisms may be impacted by biofilm formation, bacteria-bacteria interactions or bacteria-host interactions. Low molecular weight, high-affinity iron chelators known as siderophores are commonly encoded on pathogenicity islands, genomic islands containing genes that contribute to bacterial virulence<sup>6</sup>. Ferritin and bacterioferritin store intracellular iron in *E. coli* in a readily available form for metabolic processes while preventing the iron from interacting with reactive oxygen species and causing cell damage and toxicity<sup>7</sup>. Intracellular iron in *E. coli* is stored in ferritin aggregates and soluble iron accounts for less than 1% of the total



cellular iron<sup>8</sup>. In iron-rich environments, the ferric uptake regulator (Fur) binds free iron, leading to transcriptional repression of iron uptake genes<sup>7, 9</sup>. Methods of iron uptake and storage in these bacteria are important as we consider using magnetic resonance imaging (MRI) for bacterial imaging, with the possibility of iron labelling for improved MR detection of bacteria.

MRI is a non-invasive imaging modality with high spatial resolution and unrestricted depth of penetration for *in vivo* imaging. MRI is one of the most frequently employed clinical imaging modalities since it does not require the use of radioisotopes<sup>10</sup>, making it a safer alternative particularly for the young or pregnant population. Certain MR measurements are sensitive to magnetic field inhomogeneities caused by magnetic elements like iron<sup>11</sup>. These sensitivities can be exploited with contrast enhancement to improve target specificity<sup>10</sup>. Endogenous, gene-based agents provide long-term contrast and enable the monitoring of cellular activities<sup>12</sup>. Gene-based contrast has been previously demonstrated in mammalian cells by expressing single genes, such as *magA*<sup>12</sup> or *mms6*<sup>13</sup>. This has also been attempted in non-magnetic bacteria expressing full operons of magnetosome genes<sup>14</sup> from environmental magnetotactic bacteria (MTB) to improve iron uptake and/or retention and impart magnetic properties. Here we focus on *magA*, which encodes a putative iron uptake protein that has previously been successfully expressed in *E. coli*<sup>15</sup>. This previous study found that MagA functioned as an ATP-dependent iron transporter on the inner membrane of *E. coli* and may be regulated by the Fur system<sup>15, 9</sup> due to its innate repression in iron-rich conditions<sup>16</sup>. Many groups are trying to recreate the magnetosome by expressing magnetosome-associated genes in non-magnetic bacteria; however, *magA* is not conserved across all MTB. *magA* is not located on the genomic magnetosome island and is not essential for magnetosome formation<sup>17</sup>. Nevertheless, MagA expression in mammalian cells has been shown to increase cellular iron and transverse (R2, R2\*) relaxivity<sup>12, 18</sup>. Though iron loading can be detrimental to cells and toxicity has been noted following high levels of MagA induction in some mammalian cells<sup>18</sup>, but not others<sup>12, 19</sup>, MagA-mediated toxicity in bacterial cells has yet to be reported and previous *E. coli* studies did not report toxic effects<sup>15</sup>.

Here we sought to assess the MR relaxation rates of *E. coli* and examine the effect of MagA expression on MR measures. Due to high genetic intraspecies variability in *E. coli*<sup>20</sup>, we hypothesized that MR relaxation rates vary among *E. coli* strains and that expression of MagA in these bacteria would increase cellular iron content and impart magnetic properties for cellular

detection by MRI at clinical field strength. To explore differences in MR measures between bacterial strains, we examined the MR relaxation rates of various lab, commensal and uropathogenic *E. coli* along with their cellular iron and manganese contents. We evaluated the relationships between MR measures, elemental content and strain classification. We also evaluated the effect of MagA expression on bacterial MR measures by preparing a *magA* expression plasmid and transforming this construct in *E. coli* BL21(DE3). MagA expression was then assessed and related to MR relaxation rates and the cellular iron and manganese contents of cells cultured in the presence or absence of extracellular iron supplementation.

## **2.2 Materials and Methods**

### **2.2.1 Reagents**

All reagents were from Thermo Fisher Scientific, Mississauga, Canada and Sigma-Aldrich, Oakville, Canada unless otherwise noted.

### **2.2.2 Bacterial strains and culture conditions**

*E. coli* BL21(DE3) were grown in lysogeny broth (LB) for 20 h at 37°C with shaking. When transformed with pcDNA3.1MycHisA<sup>+</sup>/HA-*magA*, cells were grown in the presence of ampicillin (200 µg/mL). When transformed with a pET28a<sup>+</sup> plasmid or a pET28a<sup>+</sup>/HA-*magA-myc* construct, cells were grown in the presence of kanamycin (30 µg/mL). Iron supplementation was achieved through addition of 40 µM FeCl<sub>3</sub> to LB. To induce the expression of epitope-tagged HA-MagA-Myc, 0.4 mM isopropyl β-D-1-thiogalactopyranoside (IPTG) was added to cultures with an optical density at 600 nm (OD<sub>600</sub>) of approximately 0.6. Induced cultures were then incubated at 30°C with shaking until harvest. All other *E. coli* strains (Table 2) were grown in LB for 16 h at 37°C with shaking.

**Table 2. *E. coli* strains assessed in this study using MRI**

<b>Strain<sup>a</sup></b>	<b>Classification</b>	<b>Plasmids</b>
MG1655	Commensal	
25922	Commensal	
Nissle	Probiotic	
67	UPEC <sup>b</sup>	
AD110	UPEC	
GR-12	UPEC	
536	UPEC	
J96	UPEC	
BL21(DE3)	Lab	
BL21(DE3)	Lab	pET28a <sup>+</sup>
BL21(DE3)	Lab	pET28a <sup>+</sup> / <i>HA-magA-myc</i>

<sup>a</sup> All strains are untransformed unless otherwise indicated

<sup>b</sup> UPEC, uropathogenic

### 2.2.3 Cloning

#### PCR amplification of *HA-magA-myc*

Following overnight growth of *E. coli* BL21(DE3) / pcDNA3.1*MycHisA*<sup>+</sup>/*HA-magA*<sup>21</sup> (Figure 2) in liquid culture, plasmid DNA was isolated and quantified by measuring  $A_{260}/A_{280}$  using the DeNovix DS-11 Spectrophotometer (DeNovix, Wilmington, USA). The *HA-magA-myc* region of the plasmid was amplified by polymerase chain reaction (PCR) using custom primers (Table 3). Amplification upon adding 1 ng/ $\mu$ L or 10 ng/ $\mu$ L of pcDNA3.1*MycHisA*<sup>+</sup>/*HA-magA* was compared to a no template control. PCR reactions were completed using Phusion polymerase and a thermal cycler programmed with the following protocol: 1) 98°C 3 min, 2) 98°C 40 s, 3) 56°C 35 s, 4) 72°C 90 s, repeating steps 2 – 4 for 33 cycles and ending with 72°C for 5 min. Amplified *HA-magA-myc* was purified using ENZA DNA purification columns, digested with *NheI* and *XhoI* restriction enzymes and column purified again. This insert was subsequently introduced into pET28a as described in the following section.

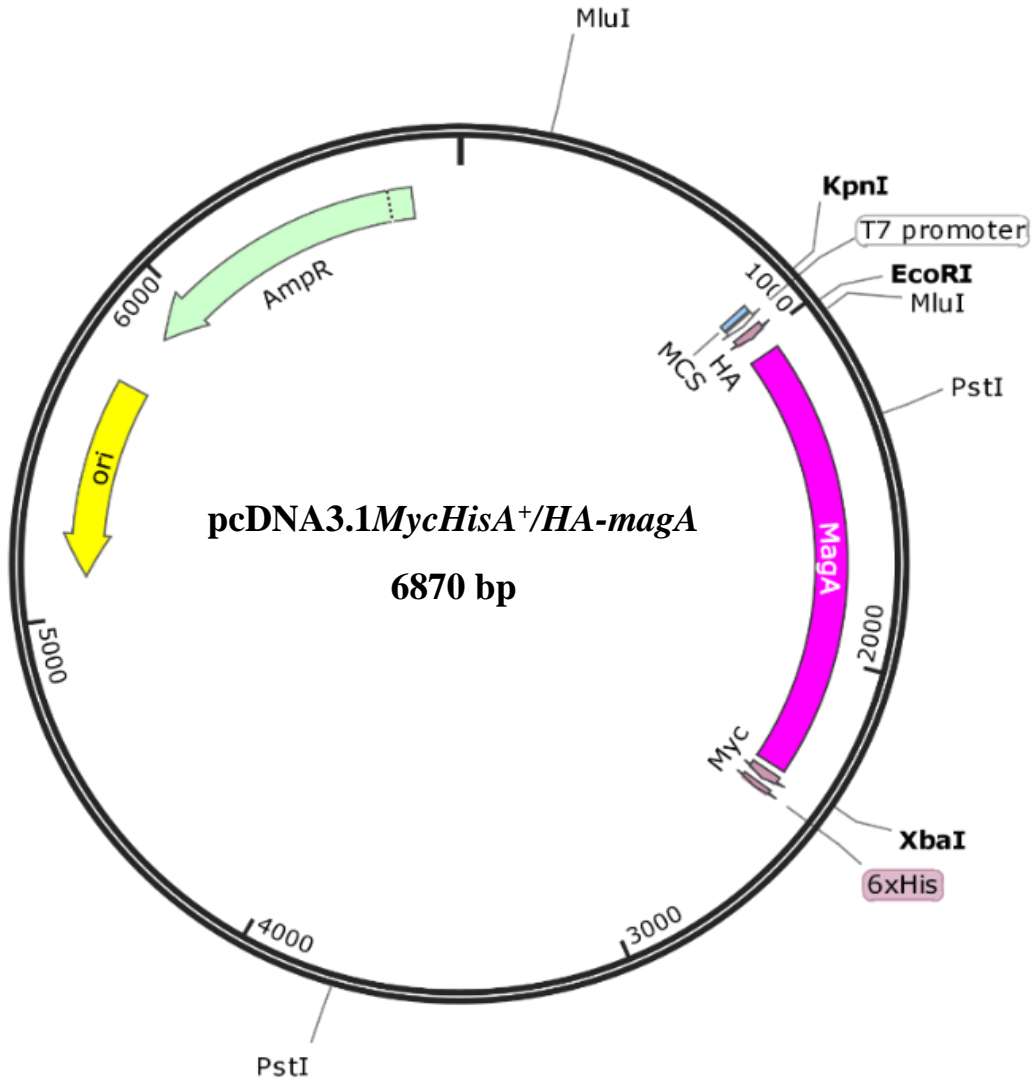


**Figure 2. Vector map of pcDNA3.1MycHisA<sup>+</sup>/HA-magA.** HA-magA was previously subcloned from pEGFP-C2 using *Bgl*III and *Bam*HI and introduced into the *Bam*HI site within the pcDNA3.1MycHisA<sup>+</sup> vector. Adapted from Quiaoit (2015)<sup>21</sup> using SnapGene 4.0

**Table 3. pET28a<sup>+</sup>/HA-magA-myc cloning primers**

<b>Primer</b>	<b>Sequence (5'-3')<sup>a</sup></b>
Forward	ATATAT <b>GCTAGCT</b> <u>TACCCATACGACGTACC</u>
Reverse	ATAATGCT <b>CGAGTCA</b> <u>TAGGTCCTCTTCTGAG</u>

<sup>a</sup> Bolded text refers to *Nhe*I (forward) and *Xho*I (reverse) restriction sites; red text in the reverse primer designates a stop codon; underlined text refers to *HA* (forward) or *myc* (reverse).

## Generation of pET28a<sup>+</sup>/HA-magA-myc

Cloning was achieved using a two-step process: first, in *E. coli* DH5 $\alpha$ , we prepared and identified the HA-magA-myc insert from the pcDNA3.1MycHisA<sup>+</sup> vector and subcloned it into our destination vector pET28a<sup>+</sup> to form our MagA expression construct. We then shuttled our final MagA expression construct into BL21(DE3), an *E. coli* strain commonly used for expression experiments.

pET28a<sup>+</sup> was propagated in *E. coli* DH5 $\alpha$ ; plasmid DNA was isolated and digested with *Nhe*I and *Xho*I. Digested pET28a<sup>+</sup> was then purified using an ENZA column. Alkaline phosphatase treatment was omitted as the digested ends were not compatible.

*Nhe*I / *Xho*I digested HA-magA-myc and pET28a<sup>+</sup> were ligated using an ~10:1 ratio of insert to vector. Ligation was performed at 16°C overnight using T4 DNA ligase. The pET28a<sup>+</sup>/HA-magA-myc ligation product was added to chemically competent *E. coli* DH5 $\alpha$  and transformed using the heat shock method<sup>22</sup>. Transformation reactions were plated on LB agar + kanamycin and grown overnight at 37°C.

Transformants were picked and screened for the presence of HA-magA-myc by PCR, using the cloning primers described in Table 2 and Taq polymerase under the following conditions: 1) 98°C 3 min, 2) 98°C 40 s, 3) 56°C 35 s, 4) 72°C 90 s, repeating steps 2 – 4 for 33 cycles and ending at 72°C for 5 min. In successfully transformed clones, the primers amplified HA-magA-myc present in pET28a<sup>+</sup> plasmid; PCR products were assessed by agarose gel electrophoresis. Positive colonies (containing the ~1.5 kb band) were grown in liquid culture and assessed by plasmid DNA isolation and restriction digestion with *Nhe*I and *Xho*I. The clone with the highest copy number displaying 5.3 kb and 1.5 kb bands by 1% agarose gel electrophoresis was chosen. pET28a<sup>+</sup>/HA-magA-myc from this clone was isolated and transformed into *E. coli* BL21(DE3), as was the empty vector, pET28a<sup>+</sup>. Several transformants were picked; plasmid DNA was isolated and digested with *Nhe*I / *Xho*I, *Nhe*I, *Sma*I, *Mlu*I, or *Mlu*I / *Xho*I to confirm successful transformation prior to sequencing. Clones with the highest copy number were pursued further.

## Sequencing

Clones of *E. coli* BL21(DE3) transformed with pET28a<sup>+</sup> and pET28a<sup>+</sup>/*HA-magA-myc* (Figure 3) were sent for Sanger sequencing (Robarts Sequencing Facilities). The empty vector was assessed using the T7 forward primer, whereas pET28a<sup>+</sup>/*HA-magA-myc* was examined using custom primers (Table 4) to sequence over the full insert and part of the surrounding vector (Appendix 3).



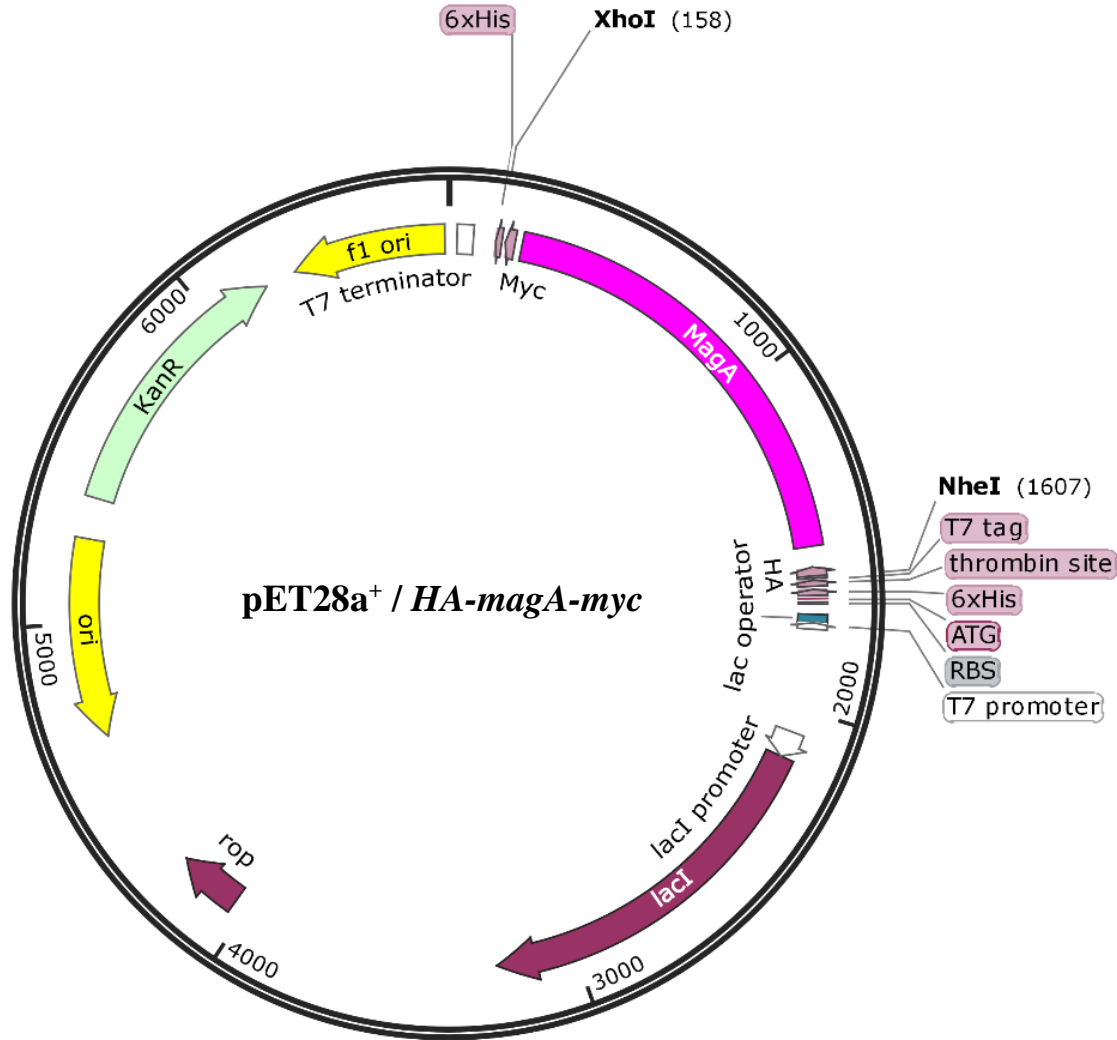


**Figure 3. pET28a<sup>+</sup>/HA-magA-myc vector map.** *HA-magA-myc* was cloned into pET28a<sup>+</sup> at *NheI* and *XhoI* restriction sites. Plasmid maps were generated using SnapGene 4.0. IPTG induction leads to dissociation of the lac repressor, allowing T7 polymerase to initiate transcription 3' to the T7 promoter. A species-specific ribosome binding site (RBS) is required to recruit the ribosome and allow for translation. The start codon (ATG) is 5' to tagged *magA*. *His*, *T7 tag* and *HA* epitope tags are found in frame 5' to *magA*, and a *myc* tag is encoded in frame 3' to *magA*. An in frame stop codon is encoded 3' to tagged *magA*, meaning that upon IPTG induction His-T7tag-HA-MagA-Myc is expressed, allowing for detection of protein expression with commercial antibodies (see section 2.2.7). The kanamycin resistance gene (KanR) enables antibiotic selection for growth of transformed bacteria.

**Table 4. pET28a<sup>+</sup>/HA-*magA*-*myc* sequencing primers**

<b>Primer</b>	<b>Sequence (5'-3')</b>
MagA 2012 <sup>a</sup>	GCGCTAAGACTGGAACGGTGGG
MagA 5' internal <sup>b</sup>	AAGAGCTTCACACCTTCTGC
MagA 3' internal rev <sup>c</sup>	GATTCCAGCACCAGCATCAT

<sup>a</sup> Anneals at position 636 bp – 658 bp from the 5' end of *magA*, providing sequence of the 3' region, including *magA*, *myc*, *His* and the stop codon

<sup>b</sup> Anneals at position 241 bp – 261 bp from the 5' end of *magA* for sequencing the middle of *magA*

<sup>c</sup> Anneals at position 509 bp – 489 bp from the 5' end of *magA* on the antisense strand to sequence the 5' end of *magA*, *HA*, the start codon and ribosome binding site

## 2.2.4 Magnetic resonance imaging

### Sample preparation

*Escherichia coli* were grown overnight as described in section 2.2.2. From these, 200  $\mu\text{L}$  of each culture were placed in the wells of a 96-well plate to measure  $\text{OD}_{600}$  in the Eon Biotek plate reader (Biotek, Winooski, USA) equipped with Gen5 2.01 software. To obtain colony-forming unit (CFU) counts, the 200  $\mu\text{L}$  cultures were serially diluted 1/10 down to  $10^{-7}$  and 10  $\mu\text{L}$  from each dilution was plated in triplicate on plates containing LB agar or LB agar + kanamycin. Plates were incubated aerobically at  $37^{\circ}\text{C}$  for 12 h before counting the number of CFUs. Equation 1 was used to calculate the total number of CFUs within the full culture based on the total culture volume and volume plated.

#### Equation 1.

$$\text{Total CFUs} = \left[ \frac{\text{Average CFUs}}{\text{Volume plated} * \text{Dilution factor}} \right] * \text{Total culture volume}$$

The remaining culture was routinely pelleted at  $4500 \times g$  for 10 min; washed once with 35 mL phosphate-buffered saline (PBS, 154 mM NaCl / 2.7 mM KCl / 10 mM  $\text{HPO}_4$  pH 7.4) then twice with 10 mL PBS. Finally, cell pellets were resuspended in PBS to prepare a ~75% cell slurry for loading into Ultem wells (inner diameter: 4 mm, inner height: 9 mm, Lawson Imaging Prototype Lab) by centrifugation at  $4500 \times g$  for 10 min. Once full, total number of CFUs within the wells was estimated using Equation 2. Number of CFUs within the MR slice (see Figure 5) constitutes  $\frac{1}{3}$  of the total CFUs loaded since slice thickness was 3 mm, the total inner height of the Ultem well was 9 mm and the wells were completely filled with bacteria.

#### Equation 2.

$$\text{CFUs in well} = \left[ \frac{\text{Total CFUs}}{\text{Total volume of cell pellet}} \right] * \text{Volume loaded in well}$$

## **Phantom preparation**

Cells were loaded into Ultem wells as described above prior to mounting in a 9 cm spherical MR phantom made of ~600 mL of 4% gelatin (porcine type A) / PBS (Figures 4 and 5)<sup>19</sup>. MR phantoms were scanned at 3 Tesla (3T) on a Biograph mMR (Siemens AG, Erlangen, Germany) adapting previously developed sequences to acquire longitudinal and transverse relaxation rates<sup>19</sup> as described below.

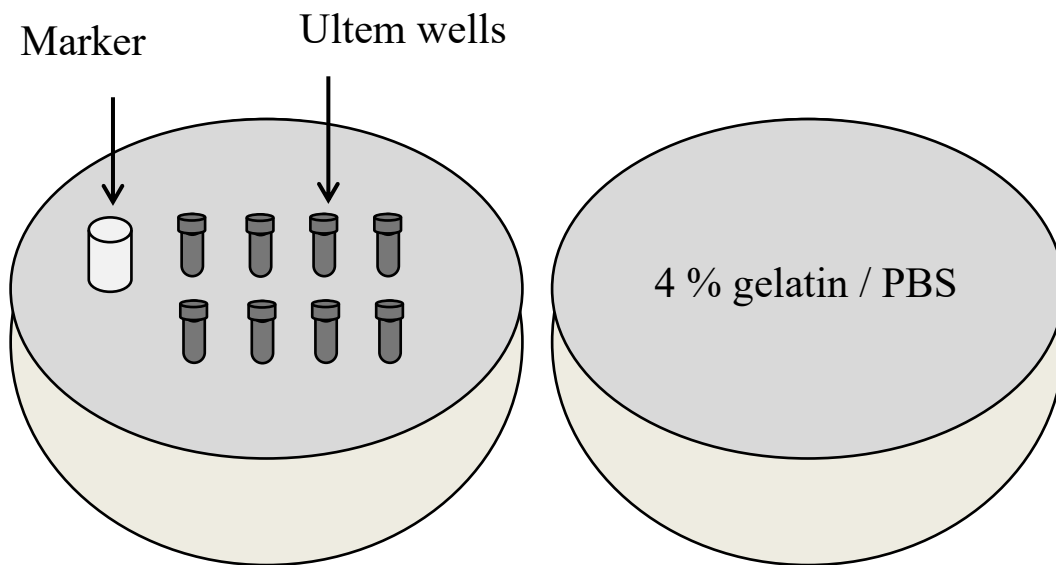


**Figure 4. MRI cell phantom.** Cells were loaded into Ultem wells by centrifugation at 4500 x g and then mounted in a spherical gelatin phantom (9 cm diameter).

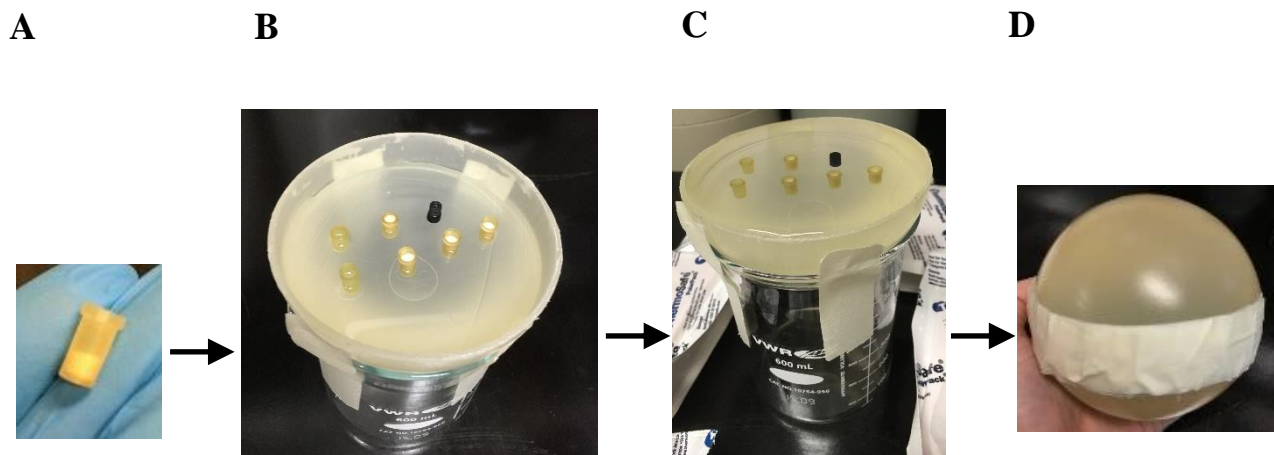


**Figure 5. Workflow for MR phantom preparation.** Within 24 h of the scan, cells were loaded into Ultem wells (A) using centrifugation to create a compact pellet. Filled wells were then mounted on a solidified layer of 4 % gelatin / PBS (B) that partially filled one hemisphere of the spherical phantom. Once positioned, the wells were completely overlaid with gelatin / PBS (C) and allowed to set for 6 h at room temperature before transferring to 4°C overnight. To assemble the spherical phantom (D), one hemisphere containing only gelatin / PBS was taped to the sample-filled hemisphere, separated by a double layer of parafilm to exclude air pockets. MR data was collected on a 3 T mMR Biograph.

## MRI Sequences

A slice thickness of 3 mm (Figure 6A) and field of view (FOV) of 120 x 120 mm<sup>2</sup> was used for all image acquisitions.

For R1 longitudinal relaxation rate acquisition, an inversion recovery (IR) spin echo sequence was used<sup>19</sup>. The matrix resolution was 128 × 128 mm<sup>2</sup> and voxel size was 1.5 × 0.9 × 0.9 mm<sup>3</sup>. Repetition time (TR) was 4000 ms, flip angle was 90°, and inversion times (TI) were 22, 200, 500, 1000, 2000 and 3900 ms. IR scanning time was approximately 39 min.

For R2 transverse relaxation rate measurements, a single-echo spin echo (SE) sequence was used. For R2\* measurements, a multi-echo gradient echo sequence (GRE) sequence was employed<sup>19</sup> (Figure 6B). The matrix resolution for both was 192 × 192 mm<sup>2</sup> and voxel size was 1.5 × 0.6 × 0.6 mm<sup>3</sup>. For the SE sequence, echo times (TE) were 13, 20, 25, 30, 40, 60, 80, 100, 150 and 200 ms; TR was 2010 ms; and flip angle was 90°. SE scanning time was approximately 61 minutes. For the GRE sequence, TE were 6.12, 14.64, 23.16, 31.68, 40.2, 50, 60, 70 and 79.9 ms; TR was 200 ms; and flip angle was 60°. GRE scanning time was approximately 25 minutes.

Compared to a previous study by Sengupta et al. (2014), a larger slice thickness was used (3 mm vs 1.5 mm). In addition, echo times for SE sequences were shorter than those used for mammalian cells<sup>19</sup> to accommodate the high transverse relaxivity of bacteria.

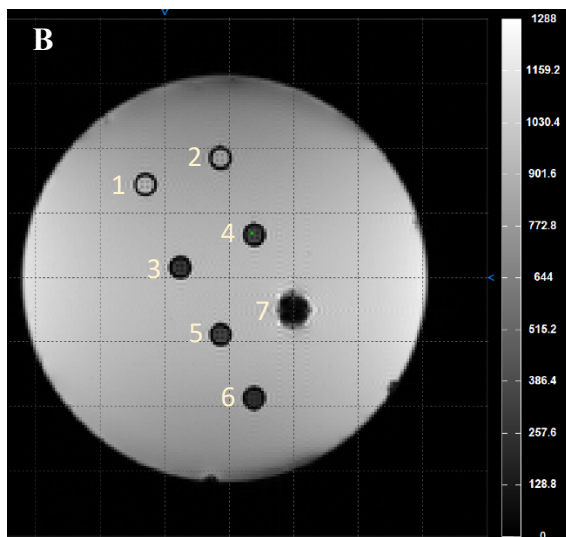
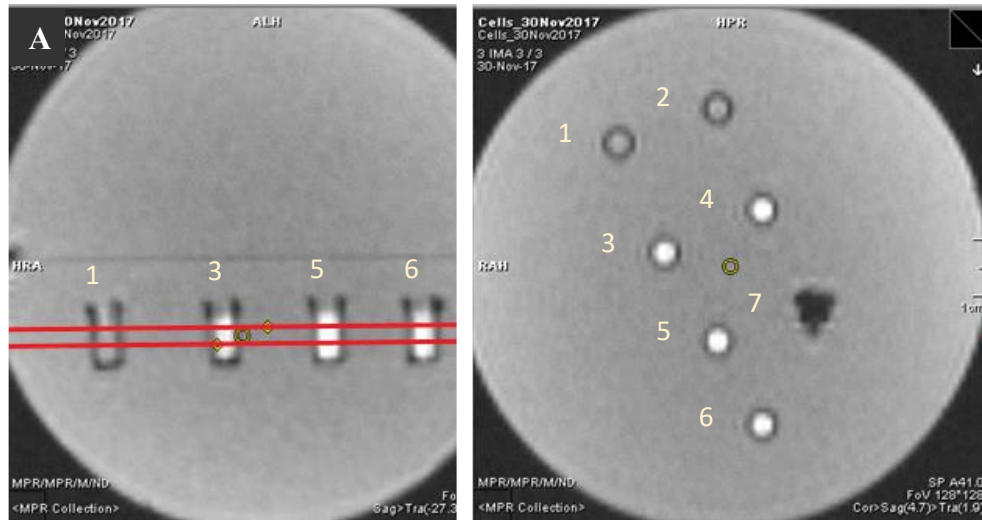


**Figure 6. Representative slice and MR image.** The MR signal was acquired from a 3 mm slice positioned perpendicular to each of the Ultem wells within a gelatin phantom, providing a cross section through the filled wells shown in two planes (A). Representative T2\*-weighted multi-echo gradient echo imaging displays *E. coli* BL21(DE3) and LB/gelatin samples where the scale bar indicates signal intensity in arbitrary units. Shown here is the signal intensity at an echo time of 31.86 ms (B). Data collected at multiple echo times are used to plot the change in signal intensity in a region of interest as a function of echo time. This provides the decay curve needed to calculate R2\* ( $s^{-1}$ ). Numbers to the left of each well designate sample identity: 1 and 2 are LB / gelatin, 3 – 6 are BL21(DE3) either washed with PBS (3 and 4) or pelleted straight from LB (5 and 6), and 7 is the marker for orientation.



## MR data analysis

Longitudinal and transverse relaxation rates of samples were determined using custom software developed in Matlab 7.9.0 (R2010b). This software was used to select a 21-voxel region of interest (ROI) within the sample, avoiding the wall of the Ultem well. The average signal intensity within the ROI was determined at each TE or TI and decay curves were plotted using GraphPad Prism software, version 8.0.0, using a single exponential line of best fit (Appendix 6).  $R2'$  was calculated by subtraction ( $R2^* - R2 = R2'$ )<sup>11</sup>. Relaxation rates of replicate samples were reported as the mean +/- standard error of the mean (SEM) using GraphPad Prism software.

A motion artifact appeared in approximately half of all images from GRE sequences. This motion always appears in the vertical/y-plane and was not caused by the physical movement of the gelatin phantom or any samples within. This apparent motion is likely attributed to MRI component malfunction requiring repair. To account for the vertical shift between TE's, the position of ROI's within each well was assessed at each TE and moved as necessary to ensure only sample would be contained within the ROI and not the edges of the Ultem well.

### 2.2.5 Protein preparation and quantification

For elemental iron quantification and western blot analysis, bacteria were cultured as above and pelleted at  $4500 \times g$  for 10 min at 20°C, washing three times with at least 10 mL PBS. Cell pellets were collected in radioimmunoprecipitation buffer (RIPA; 10 mM Tris-HCl pH 7.5/140 mM NaCl/1% NP-40/1% sodium deoxycholate/0.1% sodium dodecyl sulfate) with Complete Mini protease inhibitor cocktail (Roche Diagnostic Systems, Laval, Canada). Cells were lysed through five cycles of freeze-thaw, then pelleted at  $10,000 \times g$  for 10 min to remove debris. Protein concentrations were calculated using the bicinchoninic acid (BCA) assay and bovine serum albumin (BSA) as the standard<sup>23</sup>. Absorbance at 562 nm was determined using the Eon Biotek plate reader and Gen5 2.01 software.

### 2.2.6 Inductively-coupled plasma mass spectrometry

For elemental iron and manganese analysis, samples containing 1 – 3 mg/ml of protein were prepared as indicated in section 2.2.5. Quantification of each element was performed using

inductively-coupled plasma mass spectrometry (ICP-MS, Biotron Analytical Services, Western University). Briefly, samples were digested using nitric acid and heat, then filtered prior to mass spectrometry. The data reported in this thesis reflect total cellular iron or manganese content normalized to total amount of protein.

## **2.2.7 Examining MagA expression**

### **Protein separation**

Samples of total cellular protein described in section 2.2.5, were separated by sodium dodecyl sulfate-polyacrylamide gel electrophoresis (SDS PAGE). Samples were assessed under reducing conditions using 0.71 M  $\beta$ -mercaptoethanol. Thirty micrograms of protein from each sample was separated based on protein size using a 5% stacking gel and 10% running gel. Molecular weight (M.W.) standards were used for size comparison.

### **Western blot**

Protein separated by SDS PAGE was transferred to a nitrocellulose blot (iBlot Gel Transfer Stacks; BioRad, Hercules, USA) following the manufacturer's protocol using the iBlot Gel Transfer Device and a 7 min transfer (BioRad). To block nonspecific binding, the blot was incubated in 10% Blotto/PBS for 3 – 5 h on a rocker at room temperature. To check for expression of the epitope-tagged MagA protein, the blot was incubated overnight at room temperature in 1:1000 rabbit anti-c-Myc / 2 % Blotto/PBS. Following the primary antibody incubation, blots were washed for 30 minutes with 3 changes of PBS / 0.05% Tween 20 (PBST), then incubated for 2 hours at room temperature with 1:20,000 horseradish peroxidase (HRP)-conjugated goat anti-rabbit immunoglobulin/PBST. After the secondary antibody incubation, blots were washed for 30 minutes with three changes of PBST. Protein bands were developed using a Clarity Max<sup>TM</sup> Western ECL Substrate (BioRad) and signal was detected under the ultraviolet transilluminator using the ChemiDoc® Imaging System (Syngene, Fredrick, USA). The estimated M.W. of His-T7-HA-MagA-Myc is 54 kDa.

Level of MagA protein was compared to glyceraldehyde-3-phosphate dehydrogenase (GAPDH). Blots were stripped in 245 mM  $\beta$ -mercaptoethanol / 2 % SDS / 62.5 mM tris-hydrochloric acid

(pH 6.8), washed in PBST, and re-probed as above, using 1:2000 rabbit anti-GAPDH as the primary antibody and 1:20,000 HRP-conjugated goat anti-rabbit immunoglobulin secondary antibody. GAPDH is approximately 37 kDa.

MagA expression was also assessed using 1:2000 mouse anti-HA primary antibody paired with 1:2000 HRP-conjugated goat anti-mouse immunoglobulin secondary antibody<sup>24</sup>.

## **Coomassie Blue**

Following transfer of protein to nitrocellulose, protein remaining in the gel was stained using Coomassie blue. The gel was stained in 0.303 mM Coomassie blue / 10 % acetic acid / 25 % isopropanol for 1 h with rocking, then destained in 30.3  $\mu$ M Coomassie / 10 % acetic acid / 10 % isopropanol for 1 h, then fixed in 10 % acetic acid for 72 h, changing the acetic acid until no more stain appeared in the fixative. The stained gel was washed with distilled water and then imaged under white light using the ChemiDoc® Imaging System (Syngene).

### **2.2.8 Statistical analyses**

Statistical analyses were performed using GraphPad Prism version 8.0.0 and SPSS version 25. MR relaxation rates of bacteria were analyzed using one-way analysis of variance (ANOVA) where significance was defined at  $\alpha = 0.05$ . Pearson's correlations were assessed to determine the relationship between cellular iron content, manganese content, and MR relaxation rate. Multiple linear regression models were applied to examine correlations between measurements and trends in these measurements between *E. coli* strains. In these analyses, MR relaxation rate was the independent variable and iron and manganese content, strain designation and classification (lab, commensal or UPEC) were the dependent variables.

## **2.3 Results**

### **2.3.1 MR relaxation rates of *E. coli* BL21(DE3)**

*Escherichia coli* BL21(DE3) were cultured overnight in LB and either washed with PBS (BL21(DE3) / PBS) or left in LB (unwashed; BL21(DE3) / LB) prior to mounting in a cell phantom for MRI. Both longitudinal (R1) and transverse (R2\*, R2) relaxation rates were examined and compared to the background signals from 4% gelatin / PBS (MR phantom background) and 4% gelatin / LB (bacterial culture background). As shown in Figure 7, MR relaxation rates did not vary between washed and unwashed *E. coli*, indicating minimal contribution to MR relaxivity from either PBS or LB. R1, R2 and R2\* of BL21(DE3) were significantly higher than the gelatin or LB background (Figure 7;  $p < 0.001$ ), with transverse relaxation rates of *E. coli* over 10 to 20-times higher than background. R1 of bacteria was increased approximately 4-fold over background (Appendix 1;  $p < 0.001$ ).

The irreversible (R2) component fully explained the total (R2\*) transverse relaxation rate, with little to no contribution from the reversible (R2') component ( $R2' \sim 0$ ; Figure 7). Raw MR data are available in Appendix 7.

When BL21(DE3) cells were pelleted in Ultem wells at varying forces of gravity, there was little or no change in transverse relaxation rates (Figure 8A;  $n = 2 - 5$ ). When normalized to CFUs, relaxation rates were similar between samples (approximately  $4s^{-1}/10^9$  CFUs; Figure 7B), suggesting that the MR relaxation rates do not depend on these centrifugal speeds. We therefore assume that approximately the same number of cells were present in the imaged slice of each sample.

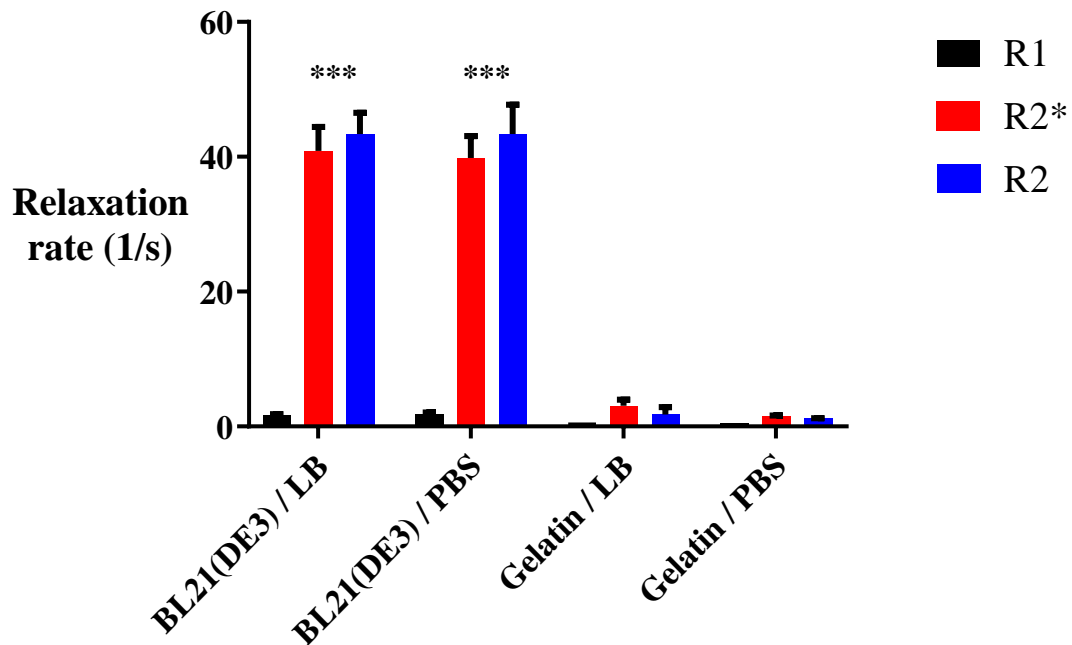


**Figure 7. *E. coli* BL21(DE3) display high transverse relaxivity.** The bar graph shows mean longitudinal and transverse relaxation rates for bacteria and/or the culture medium (n = 4 – 5). Cells were either pelleted from LB or after washing with PBS; then mounted in a cell phantom; and scanned at 3T. Data are the mean +/- SEM and were analyzed by one-way ANOVA and Tukey’s test. BL21(DE3) display significantly higher relaxation rates than gelatin/LB or the gelatin/PBS background (p < 0.001).

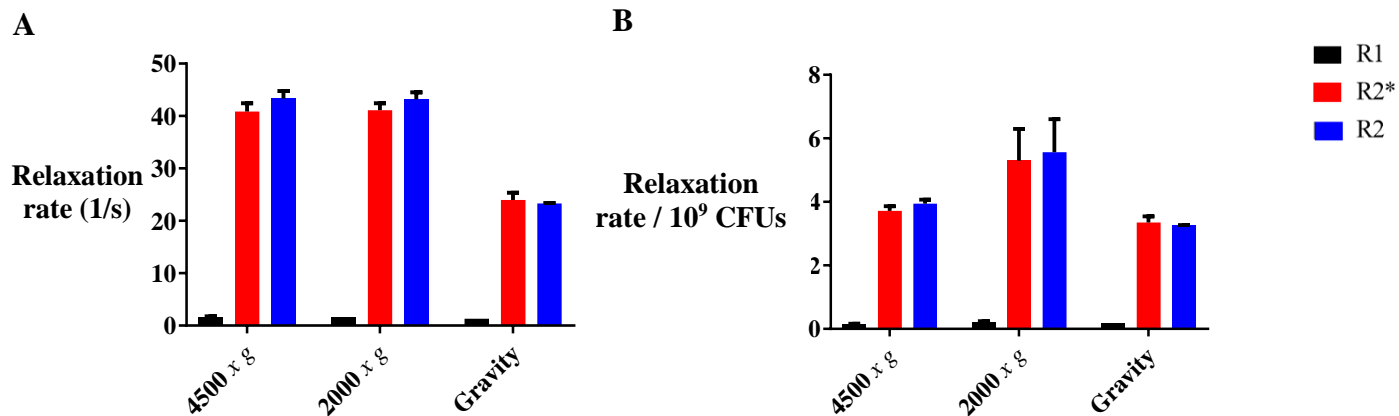


**Figure 8. Relaxation rates of BL21(DE3) packed into wells at different relative centrifugal forces.** Bar graphs show A) mean longitudinal and transverse relaxation rates, and B) mean relaxation rates per  $10^9$  colony-forming units  $\pm$  SEM for *E. coli* pelleted at various forces of gravity (n = 3 – 5, except n = 2 for gravity pelleted samples).

### 2.3.2 MR relaxation rates of various *E. coli* strains

Various lab, probiotic, commensal and uropathogenic *E. coli* strains were cultured and mounted in a gelatin cell phantom for MRI. Transverse relaxation rates for *E. coli* Nissle, 25922 and AD110 were significantly lower than those of BL21(DE3), MG1655 and J96 (Figure 9;  $p < 0.05$ ). However, there was no overall trend within the classifications of strain type. There are strains on the higher and lower ends of the range (approximately  $20 - 40 \text{ s}^{-1}$ ) within each of the lab/probiotic/commensal/UPEC groupings. As noted for BL21(DE3), transverse relaxivity in these *E. coli* strains is dominated by the R2 component with little or no R2' contribution.

These data show that transverse relaxation rates can vary widely between different strains of *E. coli*, irrespective of strain characteristics and origin (Figure 9; Table 2). The lower transverse relaxation rates of *E. coli* strains Nissle, 25922 and 67 indicate that these may be harder to detect than the other strains using SE and GRE sequences for MRI.

Although longitudinal relaxation rates of *E. coli* strains 25922, AD110 and Nissle were significantly lower than some other strains (Table 5,  $p < 0.05$ ), these MR measures showed little variation ( $1.22 - 1.88 \text{ s}^{-1}$ , Table 5). These data suggest that R1 measurements may not be a useful parameter for differentiating between *E. coli* strains in comparison to transverse relaxivity measurements. All raw MR data for *E. coli* strains are found in Appendix 8.

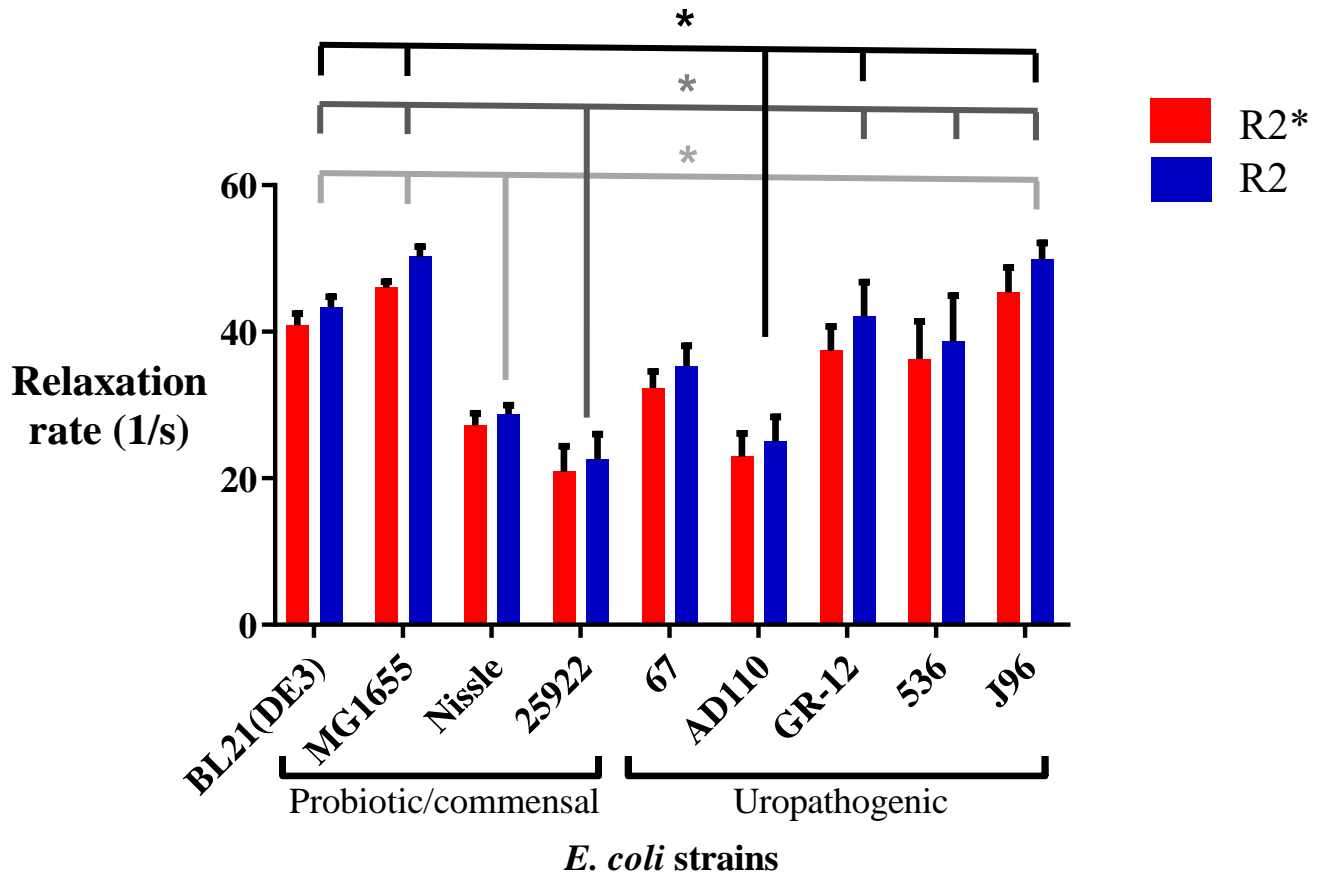


**Figure 9. *Escherichia coli* are detectable by MRI.** Bar graphs compare MR signals from the BL21(DE3) laboratory strain of *E. coli* with select probiotic (Nissle), commensal (MG1655, 25922) and uropathogenic strains (67, AD110, GR-12, 536, J96). All *E. coli* exhibit relatively high transverse relaxation rates, with R2\* consisting virtually entirely of an R2 component and little or no R2' contribution. One-way ANOVA indicates that R2/R2\* of Nissle (light gray lines), 25922 (dark gray lines) and AD110 (black lines) are significantly lower than various other tested strains (\*  $p < 0.05$ ). Data are the mean  $\pm$  SEM ( $n = 3 - 5$ ).



**Table 5. Longitudinal relaxation rates of *E. coli* strains**

<i>E. coli</i> strain	R1 (s <sup>-1</sup> ) #	SEM (s <sup>-1</sup> )	n
<b>BL21(DE3)</b> <sup>a</sup>	1.70 d	0.06	5
<b>MG1655</b> <sup>b</sup>	1.66 bcd	0.07	3
<b>Nissle</b> <sup>b</sup>	1.42 abc	0.07	3
<b>25922</b> <sup>b</sup>	1.22 a	0.08	3
<b>67</b> <sup>c</sup>	1.63 abcd	0.09	3
<b>AD110</b> <sup>c</sup>	1.31 ab	0.05	3
<b>GR-12</b> <sup>c</sup>	1.68 bcd	0.15	3
<b>536</b> <sup>c</sup>	1.64 abcd	0.09	3
<b>J96</b> <sup>c</sup>	1.88 d	0.09	3

<sup>a</sup> Lab strain

<sup>b</sup> Commensal or probiotic strain

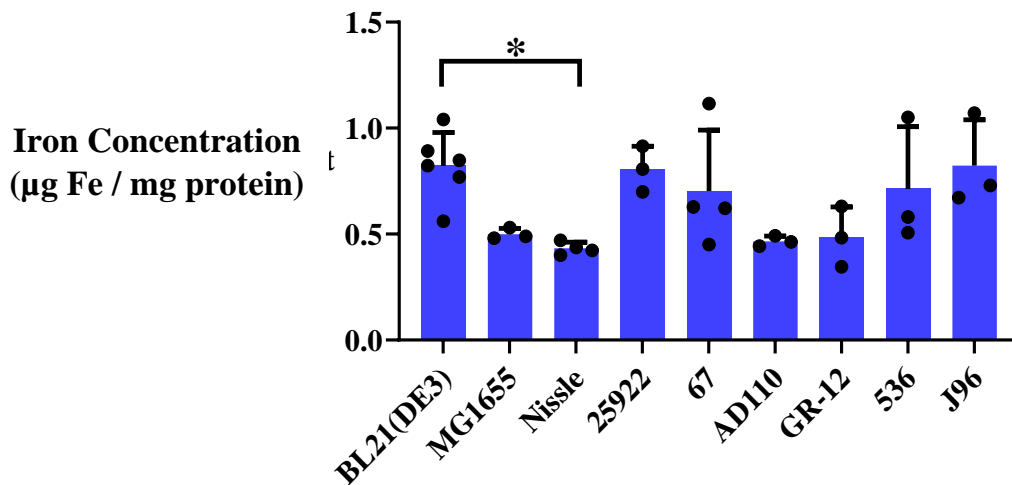
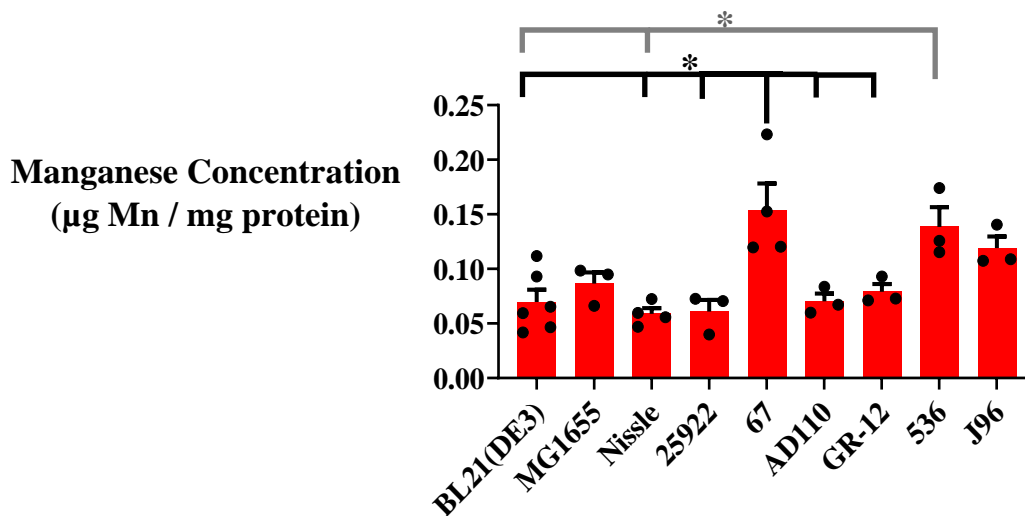
<sup>c</sup> Uropathogenic strain

# Letters designate statistically significant differences in R1 values between *E. coli* strains where values followed by the same letter are not significantly different based on a one-way ANOVA and Tukey's test ( $p < 0.05$ ).

### 2.3.3 Fe and Mn quantification in *E. coli* strains

Lysed samples from all *E. coli* strains imaged by MRI were examined by ICP-MS for quantification of ferromagnetic and paramagnetic metals like iron and manganese, respectively. When normalized to total cellular protein, total elemental iron content ranged between 0.34 to 1.2  $\mu\text{g Fe} / \text{mg protein}$  (Figure 10A). Only *E. coli* Nissle displayed significantly lower iron content than BL21(DE3) (Figure 10A;  $p < 0.05$ ) and this difference in iron content was reflected in transverse relaxation rates (R2 of Nissle,  $28.75 \text{ s}^{-1}$  vs R2 of BL21(DE3),  $43.36 \text{ s}^{-1}$ ; Figure 9). Overall however, there was little or no correlation between total cellular iron content and R2 or R2\* in these bacterial strains (Appendix 2), unlike mammalian cells<sup>19, 25</sup>.

The manganese content of these same *E. coli* strains was approximately ten-fold lower than iron, ranging between 0.04 to 0.22  $\mu\text{g Mn} / \text{mg protein}$  (Figure 10B). *E. coli* 536 sequestered more manganese than either BL21(DE3) or Nissle ( $p < 0.05$ ), and *E. coli* 67 samples contained more Mn than over half of the other strains (Figure 10B;  $p < 0.05$ ). Interestingly, UPEC strains tend to have higher manganese content than commensal or probiotic strains — UPEC have an average Mn content of 0.11  $\mu\text{g Mn} / \text{mg protein}$  compared to 0.063  $\mu\text{g Mn} / \text{mg protein}$  for the tested commensal or probiotic strains. This trend can be visualized by the grouping of UPEC manganese contents in comparison to non-UPEC strains, though sample sizes were not large enough to see any significant correlations (Appendix 2). Differences in iron and/or manganese content do not correlate with changes in MR relaxation rates, suggesting that other factors may be influencing MR measurements. All raw ICP-MS data for *E. coli* strains are found in Appendix 9.

**A****B**

**Figure 10. Content of iron and manganese varies between *E. coli* strains.** Bar graphs display the variability in total cellular content of iron (A, blue) and manganese (B, red), with approximately 10-fold higher elemental iron than manganese in all strains. Despite variability in cellular iron content, Nissle displayed lower iron levels than BL21(DE3) (A). Manganese content is significantly higher in *E. coli* 536 (gray lines) than two other strains (536 vs. BL21(DE3), 536 vs. Nissle). Likewise, manganese content is significantly higher in *E. coli* 67 (black lines) than several other strains (67 vs. BL21(DE3), 67 vs. Nissle, 67 vs. 25922, 67 vs. AD110, and 67 vs. GR-12). Data are the mean +/- SEM with points indicating individual samples (n = 3 – 6, \* p < 0.05).

### **2.3.4 Correlation between metal content and MR measures in *E. coli* strains**

Samples in which cells were analyzed both by MRI and ICP-MS provided paired Fe and Mn values for individual MR measurements. No correlation was found between iron content and R2 (Appendix 2 A), though a weak correlation appeared between Fe and R2\* (Appendix 2 C;  $p < 0.05$ ). Similarly, no correlation was evident between Mn and either R2 or R2\* (Appendix 2 B and D). When separated into strain classification (lab, commensal/probiotic or UPEC), no correlations existed (Appendix 2).

To further explore relationships between our measured parameters, we used a multiple linear regression model. Correlations between each parameter were assessed based on the Pearson correlation for comparisons between R2 or R2\* and iron content, manganese content, as well as strain designation and classification (lab, commensal/probiotic or UPEC origin). There was a moderate positive correlation between R2 and iron or manganese content ( $r = 0.380$  and  $0.395$  respectively; Table 6,  $p < 0.05$ ). Total cellular iron and manganese content were also moderately positively correlated ( $r = 0.522$ ), indicating that *E. coli* samples with higher iron also contained higher manganese levels. R2 was moderately correlated to strain, demonstrating that there is a possibility of differentiating the identity of *E. coli* strains based on R2 measurements by MRI. As expected, strain identity and classification were moderately correlated ( $r = 0.465$ ) (Table 6). R2\* was also moderately positively correlated to manganese content ( $r = 0.375$ ), but not iron content, and as in the R2 analysis, iron and manganese were moderately positively correlated, and strain identity and classification were moderately correlated. Interestingly, R2\* had a stronger correlation to both strain identity and classification than R2 ( $r = 0.519$  and  $0.449$  vs.  $r = 0.475$  and  $0.360$ ) meaning this MR measure may be slightly more sensitive to the distinction between commensal and pathogenic *E. coli* strains (Tables 6 and 7). These data provide support for the notion of using MRI measurements as a method to differentiate *E. coli* strains (Table 7,  $p < 0.001$ ).

Overall, the relationships between transverse relaxation rates and iron or manganese content indicate that there are more factors impacting transverse relaxivity besides these two metals, possibly including other paramagnetic elements and even the size and shape of bacterial cells.

**Table 6. Pearson correlation<sup>a</sup> of *E. coli* R2 measurements with iron, manganese, strain and classification.**

	R2	Fe	Mn	Strain <sup>b</sup>	Classification <sup>c</sup>
R2	1.000	0.380 *	0.395 *	0.475 **	0.360 *
Fe	0.380 *	1.000	0.522 **	0.312	0.277
Mn	0.395 *	0.522 **	1.000	0.128	0.333
Strain	0.475 **	0.312	0.128	1.000	0.465 *
Classification	0.360 *	0.277	0.333	0.465 *	1.000

<sup>a</sup> Values for the Pearson correlation coefficient, *r*, range between weak ( $\leq 0.299$ ) and moderate (0.300 - 0.699).

<sup>b</sup> Separate *E. coli* strains were arbitrarily designated by a unique numerical value.

<sup>c</sup> Classification was arbitrarily designated by a numerical value and refers to the category of bacterial strain: laboratory (designated 1), commensal/probiotic (2) or uropathogenic (3). Classifications of strains match up with axes on Figure 9 where BL21(DE3) is the lab strain.

\*  $p < 0.05$ , \*\*  $p < 0.01$

**Table 7. Pearson correlation<sup>a</sup> of *E. coli* R2\* measurements with iron, manganese, strain and classification.**

	R2*	Fe	Mn	Strain <sup>b</sup>	Classification <sup>c</sup>
R2*	1.000	0.320	0.375 *	0.519 **	0.449 *
Fe	0.320	1.000	0.522 **	0.312	0.277
Mn	0.375 *	0.522 **	1.000	0.128	0.333
Strain	0.519 **	0.312	0.128	1.000	0.465 *
Classification	0.449 *	0.277	0.333	0.465 *	1.000

<sup>a</sup> Values for the Pearson correlation coefficient, r, range between weak ( $\leq 0.299$ ) and moderate (0.300 - 0.699).

<sup>b</sup> Separate *E. coli* strains were arbitrarily designated by a unique numerical value.

<sup>c</sup> Classification was arbitrarily designated by a numerical value and refers to the category of bacterial strain: laboratory (designated 1), commensal/probiotic (2) or uropathogenic (3). Classifications of strains match up with axes on Figure 9 where BL21(DE3) is the lab strain.

\*  $p < 0.05$ , \*\*  $p < 0.01$

### 2.3.5 MagA expression in *E. coli* BL21(DE3)

Despite the relatively high transverse relaxivity of *E. coli*, we examined whether or not expression of a bacterial iron import protein would further increase the MR signal. To assess the impact of MagA expression on MR relaxation rates and iron content in *E. coli*, we transformed the BL21(DE3) laboratory strain with pET28a<sup>+</sup>/*HA-magA-myc*. Plasmid DNA was assessed by restriction digestion (Figure 11). Bacteria transformed with the empty vector served as a control for MagA expression. In addition to diagnostic digests, the successful preparation of pET28a<sup>+</sup>/*HA-magA-myc* and transformation into BL21(DE3) was confirmed by DNA sequencing.

Expression of MagA in *E. coli* BL21(DE3) was assessed in the presence or absence of IPTG-mediated protein induction. Coomassie Blue staining detected protein remaining in the gel after blotting and demonstrated that protein expression in BL21(DE3) was altered by the induction of MagA with IPTG (Appendix 4). Western blot analysis also shows altered protein expression in induced MagA-expressing cells compared to uninduced empty vector-containing cells, with an extra protein band at ~50kDa appearing in MagA-expressing *E. coli* (Figure 12).

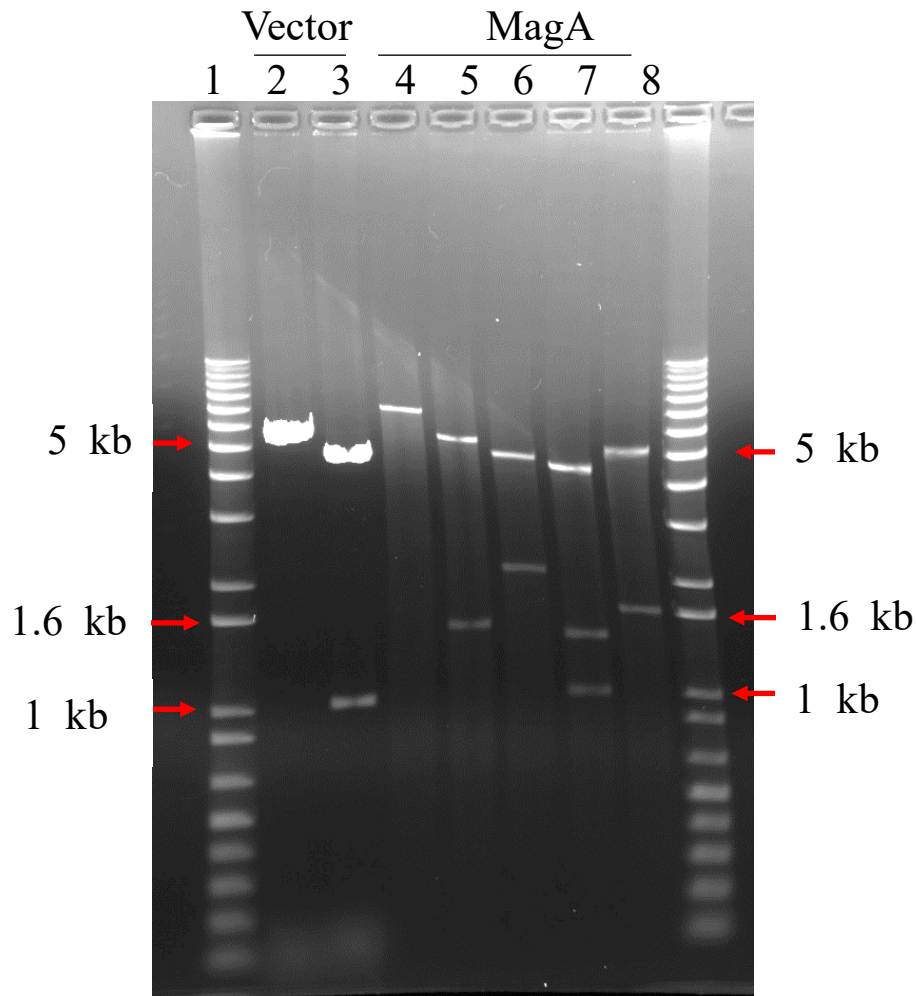


**Figure 11. Diagnostic digests of pET28a<sup>+</sup>/HA-magA-myc compared to empty vector.**

Diagnostic restriction digestion of pET28a<sup>+</sup> with and without insert DNA confirms successful insertion of *HA-magA-myc* in the *E. coli* expression vector at *NheI* and *XhoI* restriction sites.

Lanes 1 and 9 show the DNA ladder. Lanes 2 and 3 show empty vector either linearized with *NheI* (5369 bp) or doubly digested with *MluI/XhoI* (4404 bp, 965 bp), respectively. Lanes 4-8

assess pET28a<sup>+</sup>/HA-magA-myc. The full-length construct in lane 4 was linearized with *NheI*

(6745 bp). In lane 5, a double digest with *NheI/XhoI* retrieved the insert (1449 bp). Lane 6

confirms that *SmaI* cuts internally to *magA* as well as within the vector (5676 bp, 972 bp). In lane

7, *MluI* cut in the linker sequence between *magA* and *myc*, creating in an additional fragment in

the *MluI/XhoI* digested hybrid construct (977 bp, 1364 bp, 4404 bp) compared to vector alone

(lane 3). Lastly, in lane 8, *BglIII/XhoI* appropriately cleaved pET28a<sup>+</sup>/HA-magA-myc (1619 bp, 5126 bp) at sites surrounding the insert.



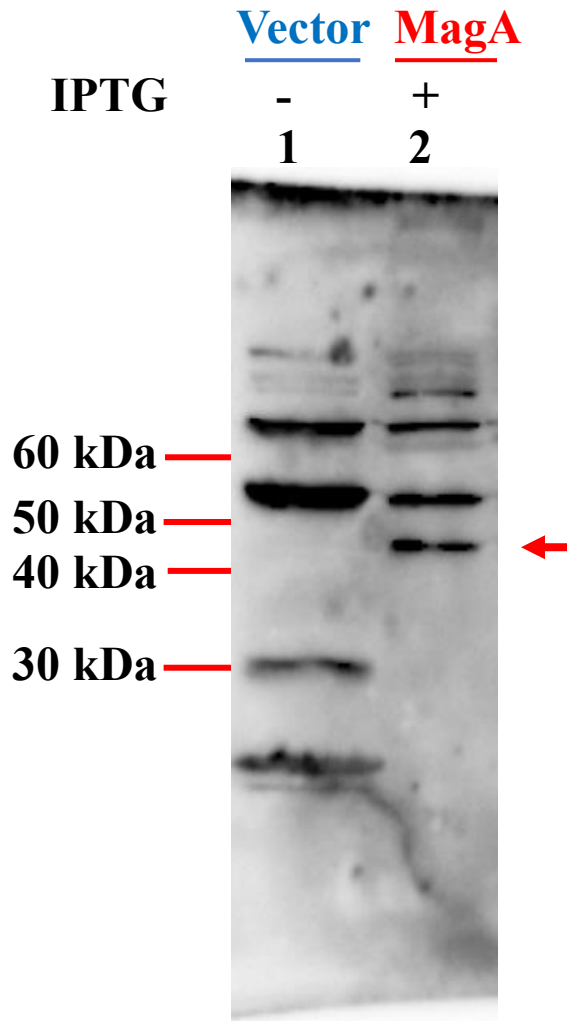


**Figure 12. Western blot of MagA expression in *E. coli* BL21(DE3).** Total protein from cells transformed with either empty vector or HA-MagA-Myc was separated by SDS-PAGE; transferred to a nitrocellulose blot; and probed with primary rabbit  $\alpha$ -cMyc to detect Ha-MagA-Myc protein levels. Molecular standards are shown on the left. Lane 1 contains uninduced cells harbouring the empty vector. Lane 2 contains induced cells harbouring the hybrid vector-MagA insert. Though there is non-specific binding in both lanes, we have provisionally identified a band in MagA-transformed *E. coli* between 40 – 50 kDa (red arrow), slightly below its estimated size of ~54 kDa.

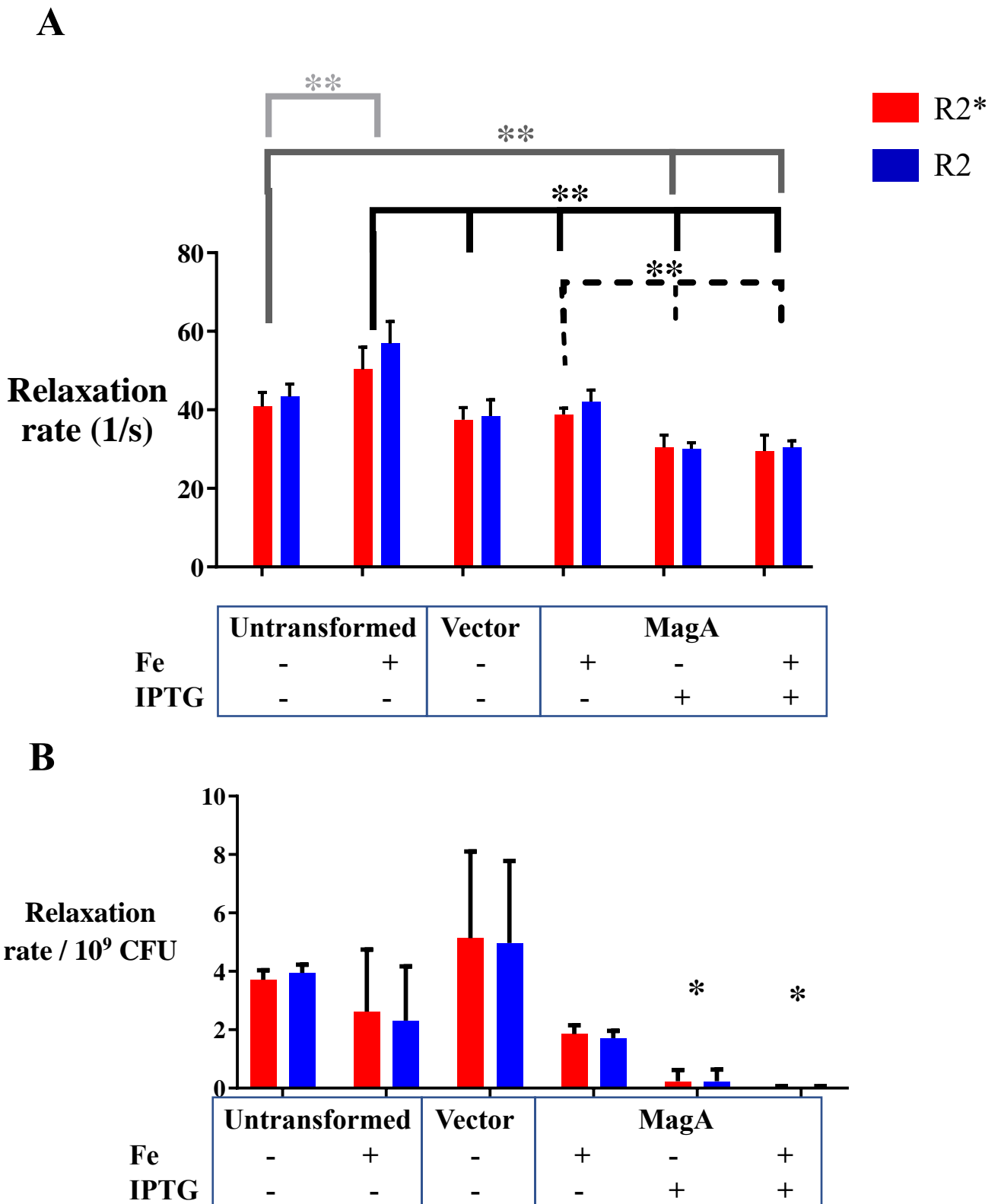
### **2.3.6 Effect of MagA expression in *E. coli* BL21(DE3) on MR measures and content of metal ions**

We sought to elucidate the impact of MagA expression on *E. coli* MR relaxation rates and cellular iron content in the presence and absence of extracellular iron supplementation. In untransformed BL21(DE3), iron supplementation alone led to a small increase in transverse relaxivity (Figure 13A); however, this was not reflected in  $R2/R2^*$  per billion CFUs (Figure 13B), suggesting little or no influence of iron supplement on transverse relaxivity. Interestingly, MagA-transformed cells displayed lower transverse and longitudinal MR measures than untransformed cells +/- Fe, particularly upon induction of MagA expression (Figure 13A, Appendix 5). This drop in relaxivity may be due to lower viability of MagA-expressing cells (Figure 13B), indicating potential toxicity in these bacteria. Viability was assessed in terms of live CFUs loaded within the MR slice since CFU counts varied even as  $OD_{600}$  remained relatively constant since MagA expression increased cell turnover rather than slowing cell growth.

Regardless of MagA expression or extracellular iron supplementation, there were no differences in total cellular iron content in *E. coli* BL21(DE3) (Figure 14A). However, manganese content decreased in MagA-expressing cells relative to controls (Figure 14B). These data show that manganese levels and  $R2/R2^*$  fluctuate in a similar manner and may be proportional to bacterial viability. We suggest that the MagA-expressing cells import more iron per live cell than controls, leading to toxicity and cell death, while manganese content is not altered by MagA expression itself, but is decreased in MagA-expressing cells due to bacterial death. Dead but unlysed cells may be contributing to the MR signal in these MagA-expressing cells, leading to the lower, but still substantial MR signal (Figure 13A). Raw MR and ICP-MS data are displayed in Appendices 10 and 11 respectively.

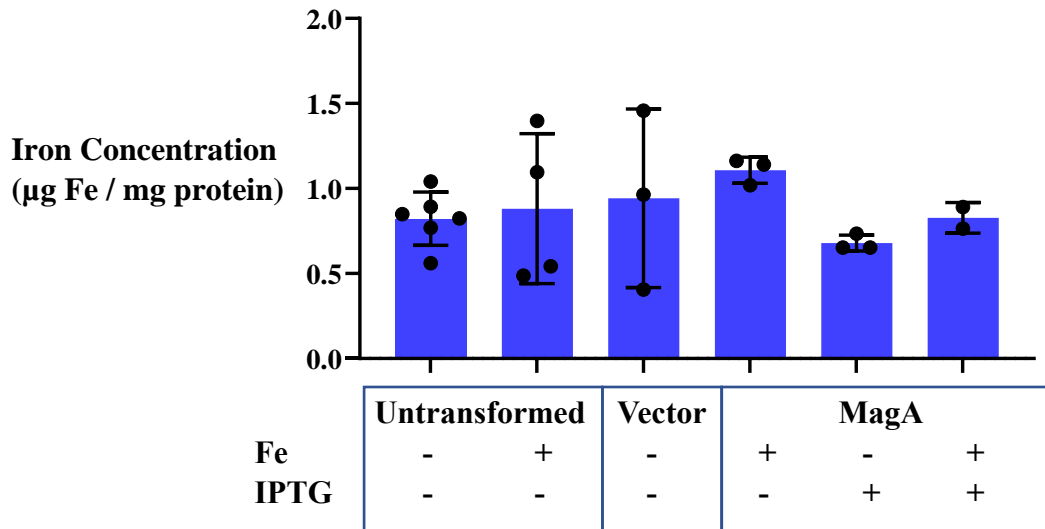
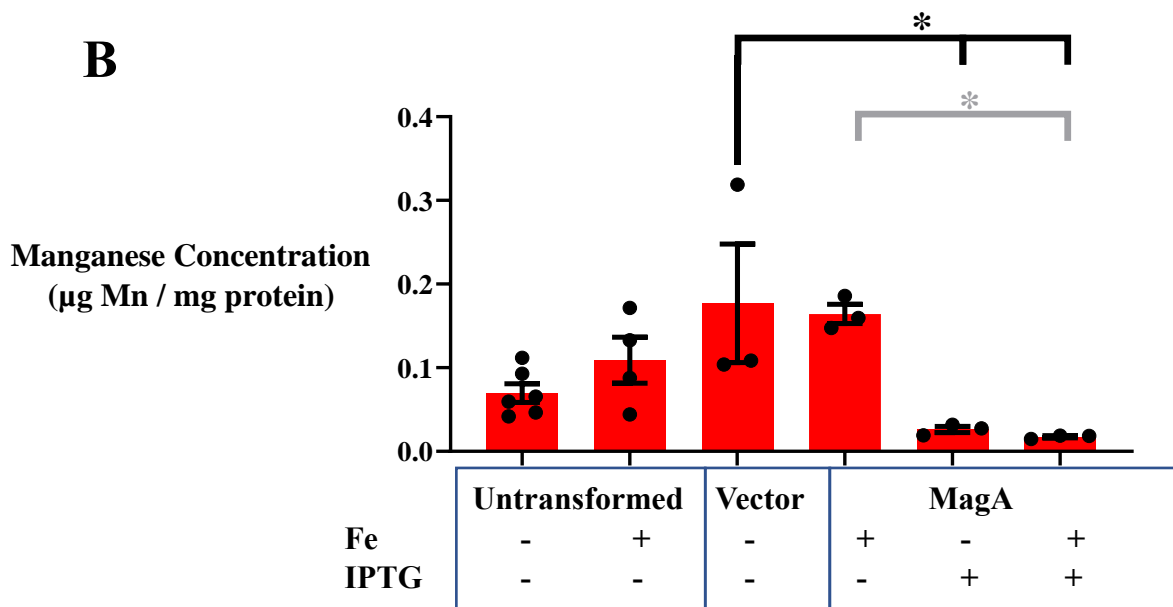
Though Fe content appears to be constant and Mn decreases in MagA-expressing *E. coli* compared to controls, there are large differences in range of iron content vs. manganese content. We see a tighter range of data distribution and lower levels of manganese overall in comparison to iron, so although significant, the differences seen may not be biologically relevant. Though

many metal ion cofactors are present in small amounts, the effects of paramagnetic particles on MRI are orders of magnitude weaker than those by ferromagnetic particles<sup>26</sup>.



**Figure 13. MagA expression does not improve MR detection of *E. coli* BL21(DE3) and diminishes cell viability.** Bar graphs compare MR signals (A) or MR signal per billion live cells

(B) for BL21(DE3) before and after transformation with vector +/- MagA insert. Transverse relaxation rates were examined in the presence and absence of iron supplementation (+/- Fe) and MagA induction (+/- IPTG). One-way ANOVA indicates that untransformed, iron-supplemented cells exhibit higher transverse relaxation rates than their unsupplemented counterparts (light gray lines, \*\*  $p < 0.01$ ). While the latter display higher  $R2/R2^*$  than induced MagA-expressing cells (dark gray lines), in the presence of iron-supplementation, untransformed BL21(DE3) exhibit higher transverse relaxivity than all forms of MagA-transformed cells, regardless of protein induction or iron supplement (black lines) indicating that MRI of *E. coli* BL21(DE3) is not improved by MagA expression. MagA induction lowers  $R2/R2^*$  in iron supplemented bacteria (dashed lines). After normalizing MR data to  $10^9$  CFUs (B), the signal from MagA-expressing cells decreases significantly as cell viability drops compared to untransformed and vector-transformed controls (\*  $p < 0.05$ ). Data are the mean +/- SEM ( $n = 3 - 5$ ).

**A****B**

**Figure 14. Manganese, but not iron content varies in MagA-expressing *E. coli* BL21(DE3).** Elemental iron content (A, blue bars) is unchanged by iron supplementation, transformation with a MagA construct, or induction of MagA expression; whereas, elemental manganese content (B, red bars) varies significantly. Total cellular manganese content is higher in the vector control than in MagA-expressing bacteria, regardless of iron supplementation (black lines, \*  $p < 0.05$ ). In iron-supplemented MagA-transformed cells, manganese levels drop following induction of MagA (gray lines). Data are the mean  $\pm$  SEM ( $n = 3 - 6$ , except  $n = 2$  for iron content of MagA + Fe + IPTG).

## **2.4 Discussion**

In summary, we examined the MR relaxation rates of *E. coli* strains that may be encountered in the laboratory, the urinary tract or the gut and have different genomic compositions and outputs relating to survival in their particular niches. In the laboratory model, BL21(DE3) displayed high transverse relaxivity, much higher than that previously described in mammalian cell lines using the same MR sequences<sup>19, 21, 24</sup>. In addition, bacterial transverse relaxivity was predominantly an R2 signal, with little to no R2' contribution. As expected, the density at which bacterial cells were packed by centrifugation into phantom wells (at relatively low speeds < 4,500  $\times$  g) did not affect the MR measures normalized to CFUs. This is consistent with MR measures being proportional to the number of live cells within the imaged sample. Between *E. coli* strains, transverse relaxation rates varied, in part due to differences in iron and manganese content. However, there was little variation in longitudinal relaxivity between these bacterial strains. Though the MR measures did not distinguish between commensal or pathogenic groups, each strain exhibited a distinct MR signature. Finally, MagA expression in *E. coli* BL21(DE3) did not enhance MR measures or increase cellular iron content when cells were cultured in the presence of extracellular iron supplementation. The data are consistent with MagA-associated cytotoxicity.

Interestingly, the baseline MR signature of *E. coli* BL21(DE3) exceeded that of mammalian cells, including those displaying contrast enhancement through MagA expression and extracellular iron supplementation<sup>19, 21, 24</sup>. The high bacterial transverse relaxivity may be useful in differentiating the MR signal of bacteria from human tissue and provides a potentially important foundation for future studies using *in vivo* MRI to observe bacterial-host interactions.

The lack of R2' component for transverse relaxivity (*i.e.* R2 ~ R2\*) in all *E. coli* strains is also interesting. Previous literature reporting that 99% of all intracellular iron in *E. coli* is stored in protein aggregates to prevent interactions with reactive oxygen species that may damage the cell<sup>7, 8</sup>. Perhaps the different components of transverse relaxivity are impacted differentially by the form of iron within the cell. In our samples R2 appears to be greater than R2\*, however this is inconsistent with the definition of R2\*. This discrepancy may have arisen because different pulse sequences were used to make independent R2 and R2\* measurements, each potentially

propagating some systematic errors. For example, flip angles errors in the SE sequence may have led to some loss of signal in the transverse plane, consequently decreasing T2 and increasing R2 measurements. Additionally, the echo-spacing in the multi-echo GRE sequence used in this study could have influenced the T2\* measurement leading to a higher T2\* time constant, and consequently a lower R2\* value. Further refinement of our MR sequence parameters for bacterial detection are warranted. Although these systematic errors are worth noting, they do not impact on the main findings of this study as we focus on the comparison of transverse relaxivity measurements between bacteria and not their absolute relaxivity values.

Our data normalizing bacterial MR measures to CFUs raise the possibility that intrastain variation in MR relaxivity may be influenced by bacterial viability, but future experiments would require a range of bacterial dilutions to accurately explore this relationship. It may also be beneficial to saturate the bacteria in an MR sensitive metal like iron or manganese to assess whether increased metal loading can improve bacterial detection when administered at sublethal levels. In addition, it would be interesting to assess MR measures in serially diluted bacterial samples to further explore the correlation between R2/R2\* and number of CFUs, and better understand the threshold for bacterial detection. For example, the PET probe 6-[<sup>18</sup>F]-fluoromaltose has a sensitivity down to 10<sup>6</sup> CFUs *in vivo*<sup>27</sup>, suggesting it may detect bacteria at the clinical threshold for most infections. In this study, Gowrishankar *et al.* (2014) administered radioactive probe to detect bacteria *in vitro* in mammalian cells as well as *in vivo* in a murine myositis model using both PET and bioluminescence imaging<sup>27</sup>. For our study, we imaged bacteria alone, assessing baseline MR signals as well as an endogenous gene-based probe (MagA) to improve imaging sensitivity. While MagA expression offered no advantage in a laboratory model, most *E. coli* strains examined had inherently high R2.

Multiple linear regression analyses showed that variations in transverse MR measures between strains of *E. coli* are partially due to total cellular iron and manganese content. In addition to the influence of these elements on the proton signal, other factors may affect MR measures. Though all *E. coli* are rod shaped, there is some strain to strain size variation<sup>28</sup> and even intrastain size variation<sup>29</sup>. Differences in iron acquisition genes and metabolic needs of strains may explain variability in cellular iron content since, as discussed in section 2.1, iron acquisition genes are virulence factors contributing to bacterial pathogenesis. For example, certain UPEC encode



siderophores such as salmochelin and aerobactin on their pathogenicity islands to improve survival in low iron environments<sup>6</sup>. Iron and manganese uptake are linked in UPEC expressing the *sitABCD* operon within their pathogenicity island(s)<sup>30</sup>. The genes in this operon include those encoding iron and manganese uptake proteins that are regulated by transcription factors involved in the Fur system as well as the MntR manganese regulator<sup>31</sup>. The combined regulation of iron and manganese uptake and enormous genetic intrastrain variability supports the similarity in trends between iron and manganese content in UPEC strains, but not necessarily the lab or commensal *E. coli* strains. Interstrain variation in MR measures may also be impacted by other magnetic or paramagnetic atoms that were not examined in this study. Not all atoms create identical local magnetic fields, meaning some compounds will have a greater impact on MRI than others<sup>26</sup>.

Total cellular iron content is positively correlated to transverse relaxation rates in iron-supplemented MagA-expressing mammalian cells<sup>19, 24, 25</sup>; therefore, we examined whether expression of the MTB putative iron transporter, MagA, in non-magnetic bacteria might further improve MR relaxivity. In our BL21(DE3) expression system this was not the case. Upon IPTG-induction, MagA-expressing cells displayed decreased viability, especially upon iron supplementation. Iron is tightly regulated in *E. coli* to prevent toxicity<sup>7</sup> so our data suggest that the reduced viability observed following MagA expression may be due to MagA-related iron toxicity. Unlike MTB which contain intracellular vesicles (magnetosomes) for dedicated iron storage, *E. coli* are innately non-magnetic. The possibility of imparting magnetic properties to non-magnetic bacteria was previously demonstrated in *Rhodospirillum rubrum*, by incorporating several operons containing approximately 30 magnetosome genes to produce relatively functional magnetosome-like iron biominerals<sup>14</sup>. The notion of creating magnetosome-like nanoparticles in mammalian cells using single gene expression systems has been partially successful, perhaps because iron may be sequestered within intracellular vesicles in eukaryotes. Nevertheless, MagA expression has given variable results in different mammalian cell types, suggesting that single MTB gene expression systems fall short of creating the optimal magnetosome-like compartment and may increase the risk of cytotoxicity<sup>18, 32</sup>. A previous study expressing MagA in *E. coli* DH5 $\alpha$  did not report toxic effects<sup>15</sup>; these cells were grown in unsupplemented LB before isolating magnetosome-like particles and subjecting these “vesicles” to 330  $\mu$ M ferrous ammonium sulfate for iron loading. We recorded cytotoxicity in MagA-

expressing BL21(DE3) cultures growing in either LB alone or LB supplemented with 40  $\mu$ M ferric chloride. While variable tolerance for MagA activity among different *E. coli* strains is a possibility, Nakamura *et al.* (1995) did not report cell growth characteristics in the presence and absence of MagA expression. Their use of the *trc* promoter suggests that there would be high basal transcription by the leaky promoter, though the T7 promoter we used has been shown to cause higher protein expression than the *trc* system<sup>33</sup>. Our MagA construct enabled us to induce protein expression, but we were unable to repress expression for more stringent regulation. Tighter regulation of MagA expression may allow us to repress MagA transcription during initial growth phases, then induce expression and cause iron loading as the culture reaches the plateau phase, enabling bacterial proliferation and iron loading through MagA expression.

## **2.5 Conclusions**

In this study, we assessed the MR relaxation rates of various *E. coli* strains and examined the effect of MagA expression on MR measures in a model laboratory bacterium. We found that each *E. coli* strain had its own MR signature; however, MRI alone was not enough to distinguish between lab, commensal or uropathogenic groups. Potentially, MR signal(s) in combination with the analysis of cellular iron and/or manganese content could be used to identify these groups of bacteria. We created a MagA-expressing *E. coli* strain and found that, regardless of iron supplementation, MagA expression reduced cell viability, thereby reducing MR relaxation rates, cellular manganese content and bacterial detection by MRI. Overall, our findings suggest that tracking bacteria using MRI is feasible and that future applications or improvements in MR detection may not require any form of contrast enhancement for *in vivo* bacterial detection within the human host.

## **2.6 References**

- [1] Gao Y.-D., Zhao Y., and Huang J. (2014) Metabolic modeling of common *Escherichia coli* strains in human gut microbiome, *BioMed Res Int* v.2014, Article ID 694967.
- [2] Geerlings S. E. (2016) Clinical presentations and epidemiology of urinary tract infections, *Microbiol Spectr* 4(5).
- [3] Ferrières L., Hancock V., and Klemm P. (2007) Specific selection for virulent urinary tract infectious *Escherichia coli* strains during catheter-associated biofilm formation, *FEMS Immunol Med Microbiol* 51, 212-219.
- [4] Floyd K. A., Moore J. L., Eberly A. R., Good J. A. D., Shaffer C. L., Zaver H., Almqvist F., Skaar E. P., Caprioli R. M., and Hadjifrangiskou M. (2015) Adhesive fiber stratification in uropathogenic *Escherichia coli* biofilms unveils oxygen-mediated control of type I pili, *PLoS Pathog* 11(3): e1004697.
- [5] Hadjifrangiskou M., Gu A. P., Pinkner J. S., Kostakioti M., Zhang E. W., Greene S. E., and Hultgren S. J. (2012) Transposon mutagenesis identifies uropathogenic *Escherichia coli* biofilm factors, *J Bacteriol* 194, 6195–6205.
- [6] Gao Q., Wang X., Xu H., Xu Y., Ling J., Zhang D., Gao S. and Liu X. (2012) Roles of iron acquisition systems in virulence of extraintestinal pathogenic *Escherichia coli*: salmochelin and aerobactin contribute more to virulence than heme in a chicken infection model, *BMC microbiol* 12, 143-154.
- [7] Abdul-Tehrani H., Hudson A. J., Chang Y.-S., Timms A. R., Hawkins C., Williams J. M., Harrison P. M., Guest J. R., Andrews S. C. (1999) Ferritin mutants of *Escherichia coli* are iron deficient and growth impaired, and fur mutants are iron deficient, *J Bacteriol* 181, 1415-1428.
- [8] Bauminger E.R., Cohen S.G., Dickson D.P.E., Levy A., Ofer S. and Yariv J. (1980) Mossbauer spectroscopy of *Escherichia coli* and its iron-storage protein, *Biochim Biophys Acta* 623, 237-242.

- [9] Uebe R., Voigt B., Schweder T., Albrecht D., Katzmann E., Lang C., Bottger L., Matzanke B., and Schuler D. (2010) Deletion of a fur-Like gene affects iron homeostasis and magnetosome formation in *Magnetospirillum gryphiswaldense*, *J Bacteriol* 192, 4192–4204.
- [10] Boucher M., Geffroy F., Preveral S., Bellanger L., Selingue E., Adryanczyk-Perrier G., Pean M., Lefevre C. T., Pignol D., Ginet N., and Meriaux S. (2017) Genetically tailored magnetosomes used as MRI probe for molecular imaging of brain tumor, *Biomaterials* 121, 167-178.
- [11] Lee C., Thompson R., Prato F., Goldhawk D., and Gelman N. (2015) Investigating the relationship between transverse relaxation rate (R2) and interecho time in MagA-expressing iron-labeled cells, *Mol Imaging* 14, 551-560.
- [12] Goldhawk D., Lemaire C., McCreary C., McGirr R., Dhanvantari S., Thompson R., Figueredo R., Koropatnick J. Foster P., and Prato F. (2009) Magnetic resonance imaging of cells overexpressing MagA, an endogenous contrast agent for live cell imaging, *Mol Imaging* 8, 129-139.
- [13] Zhang X.-Y., Robledo B. N., Harris S. S., and Hu X. P. (2014) A bacterial gene, *mms6*, as a new reporter gene for magnetic resonance imaging of mammalian cells, *Mol Imaging* 13, 1-12.
- [14] Kolinko I., Lohße A., Borg S., Raschdorf O., Jogler C., Tu Q., Posfai M., Tompa E., Plitzko J. M., Brachmann A., Wanner G., Muller R., Zhang Y., and Schuler D. (2014) Biosynthesis of magnetic nanostructures in a foreign organism by transfer of bacterial magnetosome gene clusters, *Nat Nanotechnol* 9, 193-197.
- [15] Nakamura C., Burgess J. G., Sode K., and Matsunaga T. (1995) An iron-regulated gene, *magA*, encoding an iron transport protein of *Magnetospirillum* sp. strain AMB-1, *J Biol Chem* 270, 28392–28396.

- [16] Nakamura C., Kikuchi T., Burgess J. G., and Matsunaga T. (1995) Iron-regulated expression and membrane localization of the MagA protein in *Magnetospirillum* sp. strain AMB-1, *J Biochem* 118, 23-27.
- [17] Uebe R., Henn S., and Schuler D. (2012) The MagA protein of *Magnetospirilla* is not involved in bacterial magnetite biomineralization, *J Bacteriol* 194, 1018-1023.
- [18] Cho I. K., Moran S. P., Paudyal R., Piotrowska-Nitsche K., Cheng P-H., Zhang X., Mao H., and Chan A. W. S. (2014) Longitudinal monitoring of stem cell grafts in vivo using magnetic resonance imaging with inducible Maga as a genetic reporter, *Theranostics* 4, 972-989.
- [19] Sengupta A., Quiaoit K., Thompson R., Prato F., Gelman N., and Goldhawk D. (2014) Biophysical features of MagA expression in mammalian cells: implications for MRI contrast, *Front Microbiol* 5 article 29.
- [20] Lukjancenko O., Wassenaar T. M., and Ussery D. W. (2010) Comparison of 61 sequenced *Escherichia coli* genomes, *Microb Ecol* 60, 708-720.
- [21] Quiaoit K. (2015) Towards the development of a MagA reporter gene expression construct for magnetic resonance imaging, *Western University, London, Canada, Scholarship@Western Electronic Thesis and Dissertation Repository*.
- [22] Froger A., and Hall J. E. (2007) Transformation of plasmid DNA into *E. coli* using the heat shock method, *J Vis Exp* 6, 253.
- [23] Smith P. K., Krohn R., Hermanson G. T., Mallia A. K., Gartner F. H., Provenzano M. D., Fujimoto E. K., Goetze N. M., Olson B. J., and Klenk D. C. (1985) Measurement of protein using bicinchoninic acid, *Anal Biochem* 150, 76-85.
- [24] Liu L, Alizadeh K., Donnelly S. C., Dassanayake P., Hou T. T., McGirr R., Thompson R. T., Prato F. S., Gelman N., Hoffman L., and Goldhawk D. E. (2019) MagA expression attenuates iron export activity in undifferentiated multipotent P19 cells, *PLoS ONE* 14.

- [25] Goldhawk D., Gelman N., Sengupta A., and Prato F. (2015) The interface between iron metabolism and gene-based iron contrast for MRI, *Magnetic Resonance Insights* 8, 9-14.
- [26] Ibrahim M. A., Gupta N., and Dublin A. B. (2020) Magnetic resonance imaging (MRI) gadolinium, in *StatPearls*; StatPearls Publishing, Treasure Island, FL, USA.
- [27] Gowrishankar G., Namavari M., Jouannot E. B., Hoehne A., Reeves R., Hardy J., and Gambhir S. S. (2014) Investigation of 6-<sup>[18F]</sup>-fluoromaltose as a novel PET tracer for imaging bacterial infection, *PLoS One* 9, e107951.
- [28] El-Hajj Z. W., and Newman E. B. (2015) How much territory can a single *E. coli* cell control?, *Front Microbiol* 6 article 309.
- [29] Furchtgott L., Wingreen N. S., and Huang K. C. (2011) Mechanisms for maintaining cell shape in rod-shaped Gram negative bacteria, *Mol Microbiol* 81(2):340-353.
- [30] Subashchandrabose S., and Mobley H. L. T. (2015) Virulence and fitness determinants of uropathogenic *Escherichia coli*, *Microbiol Spectr* 3(4).
- [31] Ikeda J. S., Janakiraman A., Kehres D. G., Maguire M. E., and Slauch J. M. (2005) Transcriptional regulation of sitABCD of *Salmonella enterica* serovar *Typhimurium* by MntR and Fur, *J Bacteriol* 187, 912-922.
- [32] Pereira S. M., Williams S. R., Murray P., and Taylor A. (2016) MS-1 magA: Revisiting its efficacy as a reporter gene for MRI, *Mol Imaging* 15, 1-9.
- [33] Tegel H., Ottosson J., and Hober S. (2011) Enhancing the protein production levels in *Escherichia coli* with a strong promoter, *FEBS J* 278, 729–739.

## **Chapter 3: *In vitro* characterisation of the magnetic resonance signal of *Lactobacillus crispatus* and other urinary bacterial isolates**

### **3.1 Introduction**

Bacterial-host interactions are widespread and many of these are complex symbiotic relationships as in the human microbiota at different sites in the human body. A microbiota is a community of microorganisms that interact with each other and their host to thrive. The interactions between microbes and their host cause changes in metabolism and signaling pathways, providing an explanation for how the microbiota plays a role in disease<sup>1</sup>. Having a “healthy” microbiota has been shown to protect us from pathogens, produce metabolites for energy and play a major part in homeostasis, amongst other functions<sup>2</sup>. Unfortunately, microbiome interactions are complex and difficult to replicate outside of the host<sup>2</sup>.

The current gold standard for microbiota analyses involves *ex vivo* analysis, by removing microbial samples from the mucosa and attempting to propagate these *in vitro* for high-throughput analyses, such as 16S rRNA analysis, shotgun metagenomics or metabolomics to identify the microbes, their properties and functions. However, these samples may become degraded, contaminated, or undergo changes in bacterial growth that render them unrepresentative of the original sample. For example, the microbiota within feces versus the intestinal mucosa or other sites along the gastrointestinal tract can differ in both bacterial diversity and abundance<sup>3, 4</sup>. Many microbes depend on bacterial-host interactions, specific nutrient requirements and atmospheric conditions to survive, making them difficult to culture *ex vivo*. Although there are model systems for complex cultures, including the artificial human gut/chemostat fermenters<sup>2</sup>, it is impossible to fully recreate the complexity of the microbiome *in vitro*, therefore, these methods should be used as tools to validate *in vivo* techniques. Chemostat systems are reproducible and cost-effective alternatives to *in vivo* studies, but reports have found variation in same-donor between-run repeatability as well as discrepancies in the composition of fecal inocula compared to chemostat culture. Additionally,

over 30 days may be required to achieve a stable community<sup>2</sup>, in which time *in vivo* techniques could have already been performed and treatment initiated.

Given the importance of the microbiota on human health, it is critical to establish ways to visualize the microbiota in healthy and disease states *in vivo*, to complement the current *ex vivo* analyses and to elucidate the factors involved in disease manifestation and progression in real time. In the future, this may be achieved with imaging tools such as magnetic resonance imaging (MRI) to detect and identify microbes. The utility of advanced imaging techniques for microbiome research is exemplified by a recent microscopy study using fluorescence in situ hybridization (FISH)<sup>5</sup>. Prior to this study, it was believed that gut bacteria were dispersed in microcolonies but, through imaging gnotobiotic mice with FISH, it was observed that the gut microbiota is very dynamic, with rapid turnover and cellular shedding preventing aggregations and leading to more homogeneous bacterial dispersion<sup>5</sup>. There are also many groups exploring the potential applications of positron emission tomography (PET)<sup>6</sup> and ultrasound<sup>7</sup> to visualize the presence and dispersion of specific bacteria within the microbiota. There is still much to learn in microbiome research and complementing *ex vivo* analyses with *in vivo* imaging may be beneficial for observing bacterial growth, dispersion and behaviour in their preferred niche, as these properties are not well-studied in either health or disease.

While modalities like MRI are widely applied clinically, currently very little research has employed this technology to specifically detect bacteria<sup>8,9</sup>. There are a multitude of MRI studies imaging bacterial infection indirectly by focusing on inflammation<sup>10,11</sup>. Assuming bacteria can be detected at clinically relevant levels using MRI, the question remains whether the bacterial magnetic resonance (MR) signal can be resolved from that of surrounding mammalian tissues based on distinct differences in cellular relaxation rates, individual cell characteristics and diffusion. Does *et al* (2002) used 4.7 Tesla MRI to resolve three distinct microenvironments within the rat trigeminal nerve *in vivo* based on a combination of T1 and T2<sup>12</sup>. Using these data and theoretical physics, others suggest that if the difference in MR relaxivity between two components is great enough, separation of the MR signatures may be possible<sup>13-15</sup>. We hypothesize that differences in MR signatures of different cell types may be partially due to differences in intracellular MR-sensitive metal concentrations such as iron and manganese.



Ferromagnetic and paramagnetic metals like iron, manganese, nickel, cobalt, gadolinium, and dysprosium influence MRI. The association of various bacterial types with metals in the environment and in medicine has long been investigated<sup>16-18</sup>. Bacterial acquisition of metal cofactors, like iron and manganese is widely considered a form of bacterial pathogenesis with many siderophores encoded on pathogenicity islands to improve survival in low iron environments<sup>19, 20</sup>. Ferritin and bacterioferritin store intracellular iron for use in metabolic processes in bacteria while preventing the iron from interacting with reactive oxygen species and causing cell damage and toxicity<sup>21</sup>. In iron-rich environments, the ferric uptake regulator (Fur) binds free iron, leading to transcriptional repression of iron uptake genes<sup>21, 22</sup>. Iron and manganese uptake are linked in gram-negative uropathogenic *Escherichia coli* (UPEC) expressing the *sitABCD* operon within their pathogenicity island(s)<sup>23</sup>. The genes in this operon include those encoding iron and manganese uptake proteins that are regulated by transcription factors involved in the Fur system, as well as the MntR manganese regulator<sup>24</sup>. In *Staphylococcus aureus*, iron acquisition is facilitated mainly through the *isd* genes to obtain iron in the form of heme, as well as the Fe<sup>3+</sup> siderophore system. Staphyloferrin A (*sfa*) is one of the siderophores produced by *Staphylococcus* spp. that is regulated by Fur<sup>25</sup>. This siderophore is encoded by the *sfaABC* operon and *sfaD*, and though mutation of this locus prevents staphyloferrin A production, bacterial growth is unaltered due to redundancy in iron acquisition<sup>26</sup>. Staphyloferrin B is encoded by the siderophore biosynthesis (*sbm*) operon, and unlike *sfa*, mutations in *sbm* lead to impaired bacterial iron acquisition and growth<sup>26</sup>. Deletion of both *sfa* and *sbm* leads to severely impaired growth in iron deplete conditions where active iron uptake by siderophores is crucial, but in iron replete conditions, growth of siderophore mutants is recovered<sup>26</sup>. Unlike many other bacteria, lactobacilli do not use iron as a cofactor; instead they rely on manganese<sup>27, 28</sup>. In general, lactobacilli actively import manganese using the MntA manganese/cadmium transporter<sup>29, 30</sup> for downstream uses in activating enzymes like lactate dehydrogenase and RNA polymerase<sup>31</sup>. Both bacterial acquisition and storage of paramagnetic metals like iron and manganese are important factors to consider when using MRI for bacterial imaging.

Our research group is mostly interested in the urological system. The most frequent infection of humans is urinary tract infections, where the main aetiological agent responsible is *E. coli*. However, in healthy individuals, the lower urinary system is dominated by species of lactobacilli and most frequently, members of the *Lactobacillus crispatus* species. While the microbiota of the

urinary system is slightly more complex than the absence or presence of these commensal bacteria in health or disease, it represents a much simpler microbiota than that of other sites in the body, with lower microbial diversity and reasonable densities, enabling more rapid human studies in this area. Here, we sought to assess the MR relaxation rates of various pathogenic and commensal urinary isolates and to explore the bacterial detection limit using MR measures. In addition, we examined how mixed bacterial/mammalian cell samples may impact MR measures and potentially alter individual bacterial MR signatures. Due to large genetic variability and differences in iron and manganese handling<sup>31</sup>, we hypothesized that MR relaxation rates vary drastically between bacterial species. We also suggested that bacteria with higher cellular iron or manganese content would have higher MR relaxation rates and therefore be easier to detect by MRI at clinical field strength. To explore differences in MR measures between urinary bacterial isolates, we examined the MR relaxation rates of various probiotic, commensal and uropathogenic bacteria along with their iron and manganese content. In addition, we related bacterial counts to MR measures and assessed the feasibility of distinguishing MR signatures in mixed samples of human bladder cells and *L. crispatus*. Finally, we explored the effect of iron acquisition mutants on cellular MRI and metal content.

## **3.2 Materials and Methods**

### **3.2.1 Reagents**

All reagents were from Thermo Fisher Scientific, Mississauga, Canada and Sigma-Aldrich, Oakville, Canada unless otherwise noted.

### **3.2.2 Bacterial strains and culture conditions**

*Escherichia coli* BL21(DE3) was grown in LB for 20 h at 37°C with shaking. Staphylococci were grown in Brain-Heart Infusion (BHI) broth for 16 h at 37°C with shaking, or, when noted, in iron deplete RPMI-1640 medium for 24 h at 37°C with shaking. *Pseudomonas aeruginosa* PA01 was grown in LB for 16 h at 37°C with shaking. All lactobacilli were grown in deMan,

Rogosa and Sharpe (MRS) broth anaerobically for 24 h at 37°C. *Proteus mirabilis* 296 and *Klebsiella pneumoniae* 280 were grown in LB, while *Enterococcus faecalis* ATCC33186 was grown in BHI, all anaerobically for 24 h at 37°C.

### **3.2.3 Tissue culture conditions**

Human bladder epithelial cells (ATCC 5637) were cultured in RPMI-1640 containing 10% FBS and 4 U/mL penicillin/4 µg/mL streptomycin at 37°C in 5% CO<sub>2</sub>. For passaging or amplification, plates were washed twice with PBS then cells were agitated in 0.05% trypsin / ethylenediaminetetraacetic acid and incubated at 37°C for 10 min before removing cells. Cells were pelleted at 550 x g for 10 min at 10°C then washed with PBS and resuspended in fresh media for plating.

### **3.2.4 Magnetic resonance imaging**

#### **Bacterial sample preparation**

After bacteria were grown overnight as described in section 3.2.2, 200 µL of each culture was placed in a 96-well plate and measured in an Eon BioTek plate reader (Biotek, Winooski, USA) with Gen5 2.01 software to obtain OD<sub>600</sub> measurements. This aliquot of each culture was then serially diluted 1/10 down to 10<sup>-7</sup> and 10 µL volumes were plated in triplicate on LB/agar or BHI/agar. *Proteus mirabilis* samples were always plated on 6% non-swarming LB/agar. For lactobacilli, 5 µL of each dilution was plated in triplicate on pre-warmed MRS/agar plates. After drying, plates were inverted and incubated either aerobically or anaerobically (depending on the bacterium) at 37°C for 12–24 h before counting the number of CFUs. Equation 1 (Chapter 2) was used to calculate the total number of CFUs within the full culture based on the total culture volume and volume plated.

The remaining culture was routinely pelleted at 4500 x g for 10 min, washed once with 35 mL PBS then twice with 10 mL PBS. Finally, cell pellets were resuspended in PBS to prepare a ~75% cell slurry and loaded into Ultem wells by centrifugation at 4500 x g for 10 min. Supernatant was removed and more cells were added and centrifuged until the Ultem well was full. Total number of CFUs within the wells were estimated using Equation 2 (Chapter 2) based

on CFU counts. The number of CFUs within the MR slice (see Figure 15) constitute  $\frac{1}{3}$  of the total CFUs loaded within the well, since slice thickness was 3 mm and the total inner height of the Ultem well was 9 mm.

For *L. crispatus* dilutions, cells were cultured and quantified as described above but final cell pellets were diluted 1/2 in 4 % gelatin / PBS before serially diluting 1/2 down to a final dilution of 1/32. Diluted cells were mixed gently; loaded into Ultem wells; and immediately placed at 4°C to solidify before mounting in the gelatin phantom.

### **Sample preparation of bladder cells mixed with *L. crispatus***

Human ATCC 5637 bladder cells were cultured as per section 3.2.3 in 12 x 150 mm plates; harvested; and combined into one sample for the serial dilutions described below. For harvesting, plates were washed twice with PBS, incubated with 0.05% trypsin/ethylenediaminetetracetic acid for 10 min, then cells were collected in a 50 mL conical tube. Cells were pelleted at 550 x g at 10°C for 10 min then washed three times with PBS before obtaining cell counts using hemacytometry. *Lactobacillus crispatus* ATCC33820 were collected as described above (subsection on bacterial sample preparation, section 3.2.4) including plating for cell counts. A suspension of *L. crispatus* was serially diluted  $\frac{1}{2}$  with a suspension of bladder cells using the following ratios of mammalian:bacterial cells (v/v): 15:1 (93.75%/6.25%), 7:1 (87.5%/12.5%), 3:1(75%/25%) and 1:1 (50%/50%). Samples of bladder cells alone were also prepared for MR analysis. Two biological replicates at each ratio were loaded into Ultem wells by centrifugation at 550 x g; removing supernatant and loading more sample until wells were full of the cellular mixture. Total number of bladder cells as well as bacterial cells were calculated as per Equation 2 (Chapter 2), factoring in the ratio of each cell type.

### **Phantom preparation**

Cells were loaded into Ultem wells prior to mounting in a 9 cm spherical MR phantom made of 4% gelatin (porcine type A)/PBS (Figures 4 and 5 in Chapter 2). MR phantoms were scanned at 3T on a Biograph mMR (Siemens AG, Erlangen, Germany), adapting previously developed sequences<sup>32</sup> to acquire longitudinal and transverse relaxation rates, as described below.

## MRI Sequences

A slice thickness of 3 mm (Figure 15A) and field of view (FOV) of 120 x 120 mm was used for all image acquisitions.

An inversion recovery (IR) spin echo sequence was used to acquire R1 measurements. Matrix resolution was  $128 \times 128 \text{ mm}^2$  and voxel size was  $1.5 \times 0.9 \times 0.9 \text{ mm}^3$ . Repetition time (TR) was 4000 ms, flip angle was  $90^\circ$ , and inversion times (TI) were 22, 200, 500, 1000, 2000 and 3900 ms.

For R2 transverse relaxation rate measurements, a single echo spin echo (SE) sequence was used (Figure 15B) and a multi-echo gradient echo (GRE) sequence for R2\* measurements. The matrix resolution for both sequences was  $192 \times 192 \text{ mm}^2$  and voxel size was  $1.5 \times 0.6 \times 0.6 \text{ mm}^3$ . For SE spin echo, measurements were obtained at echo times (TE) 13, 20, 25, 30, 40, 60, 80, 100, 150 and 200 ms; TR was 2010 ms; and flip angle was  $90^\circ$ . Scanning time took approximately 61 minutes. For the GRE sequence, measurements were obtained at TE 6.12, 14.64, 23.16, 31.68, 40.2, 50, 60, 70 and 79.9 ms; TR was 200 ms; and flip angle was  $60^\circ$ .

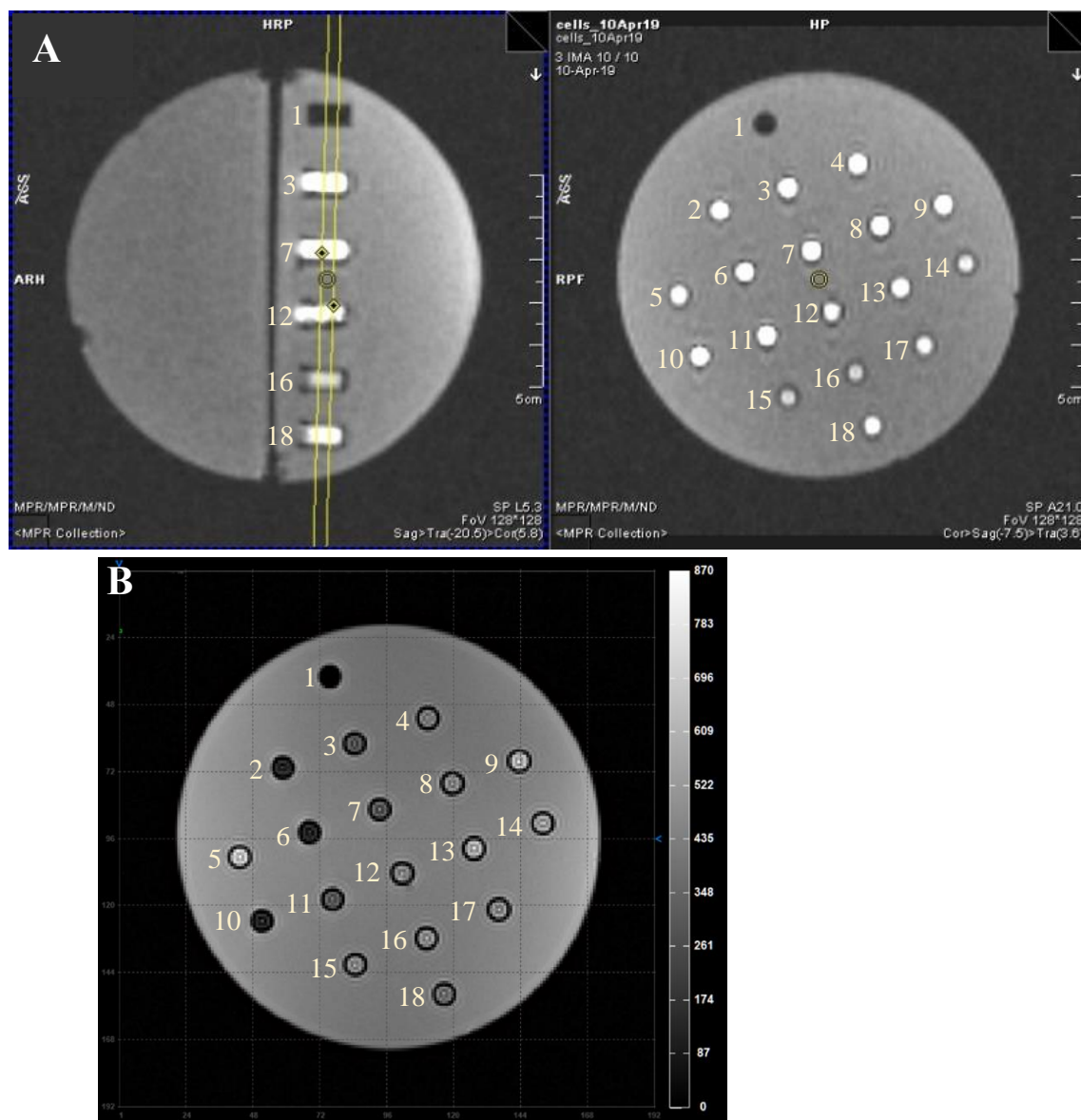


**Figure 15. Representative slice and MR image.** The MR signal was acquired from a 3 mm slice through the wells of a gelatin phantom where the cross-section through the samples is shown in two planes (A). Representative T2-weighted spin echo imaging displays an array of serially diluted *L. crispatus* ATCC33820 samples where the scale bar indicates signal intensity at the specified echo time (B). Changes in signal intensity over echo time are plotted to obtain R2 values. Numbers to the left of each well designate sample identity: 1 is the marker for orientation; 2, 6 and 10 are 1/2 dilutions of *L. crispatus* in gelatin; 3, 7 and 11 are 1/4 dilutions of *L. crispatus* in gelatin; 4, 8 and 12 are 1/8 dilutions of *L. crispatus* in gelatin; 5, 9 and 13 are 1/16 dilutions of *L. crispatus* in gelatin; 14 contains *Staphylococcus aureus* USA300; 15 contains the double deletion mutant of *S. aureus* USA300  $\Delta$ sfA/ $\Delta$ sbn; 16 is the triple deletion mutant of *S. aureus* USA300  $\Delta$ sfA/ $\Delta$ sbn/ $\Delta$ ftnA; 17 contains transformed *E. coli* BL21(DE3)/pET28a<sup>+</sup>; 18 contains iron-supplemented *E. coli* BL21(DE3)/pET28a<sup>+</sup>.

## **MR data analysis**

Longitudinal and transverse relaxation rates were determined using custom software developed in Matlab 7.9.0 (R2010b). This software was used to select a 21-voxel ROI within the sample, avoiding the wall of the Ultem well. Signal intensity within the ROI was determined at each TE or TI and decay curves were plotted using Prism software (GraphPad; San Diego, CA) version 8.0.0, and a single exponential line of best fit (Appendix 6).  $R2'$  was calculated by subtraction ( $R2^* - R2 = R2'$ ). Relaxation rates were reported as the mean  $\pm$  SEM using Prism software.

A motion artifact appeared in approximately half of all images from GRE sequences. This motion always appears in the vertical/y-plane and was not caused by the physical movement of the gelatin phantom or any samples within. This apparent motion is likely attributed to MRI component malfunction requiring repair. To account for the vertical shift between TE's, the position of ROI's within each well was assessed at each TE and moved as necessary to ensure only sample would be contained within the ROI and not the edges of the Ultem well.

## **Post-scanning viability assessment**

To qualitatively assess the viability of bacterial pellets following MRI, we used the LIVE/DEAD™ BacLight™ Bacterial Viability Kit and fluorescence microscopy. Approximately half of the cell pellet within the Ultem well was resuspended in 5 mL of PBS. In a separate tube, 1.5  $\mu$ L reagent A (SYTO 9) and 1.5  $\mu$ L reagent B (propidium iodide) were diluted in 1 mL sterile distilled water. Then, 500  $\mu$ L of each resuspended sample was mixed with 100  $\mu$ L of diluted reagents A + B and incubated at room temperature for 15 min in the dark. Cells were centrifuged at 12,000  $\times$  g for 5 min to remove the supernatant and cell pellets were washed with PBS to remove unbound dye. Stained samples were diluted in PBS as necessary and 5  $\mu$ L was loaded onto slides with mounting oil and coverslips. Slides were examined by fluorescence microscopy on a Zeiss Axioskop (Carl Zeiss AG, Oberkochen, Germany) with a FluoArc HBO 100 (Carl Zeiss AG) fluorescence illumination system, using the Texas red filter (excitation 596 nm / emission 615 nm) to visualize dead cells (stained with propidium iodide) and the FITC filter (excitation 495 nm / emission 519 nm) for SYTO 9 labelling of live cells. To obtain semi-quantitative data, relative proportions of live to dead cells were estimated by manually counting

the number of dead cells over at least three separate fields of view containing ~100 - 500 cells per FOV.

### **3.2.5 Protein preparation and quantification**

For elemental iron quantification, bacteria were cultured as above and centrifuged at 4500  $\times$  g for 10 min at 20°C, washing three times with at least 10 mL PBS. Cell pellets were collected in RIPA buffer with Complete Mini protease inhibitor cocktail (Roche Diagnostic Systems, Laval, Canada) and lysed through five cycles of freeze-thaw. Protein concentrations were calculated using the BCA assay and BSA as the standard<sup>33</sup>. Absorbance at 562 nm was determined using the Eon plate reader.

### **3.2.6 Inductively-coupled plasma mass spectrometry**

For elemental iron and manganese analysis, samples containing 1–3 mg/mL of protein were prepared as indicated in section 3.2.5. Quantitation was performed using ICP-MS (Biotron Analytical Services, Western University). Briefly, samples were digested using nitric acid and heat, then filtered prior to mass spectrometry. The data reported here reflect total cellular iron or manganese content normalized to total amount of protein.

### **3.2.7 Statistical analyses**

Statistical analyses were performed using Prism software and SPSS version 25. MR relaxation rates and metal contents of bacteria were analyzed using one-way ANOVA, where significance was defined at  $\alpha = 0.05$ , and followed by Tukey's test. Kruskal-Wallis multiple comparisons test was performed on ICP-MS data of bacterial species since these data were non-parametric. R2/R2\* ratio comparisons were achieved using the unpaired Mann-Whitney test to compensate for large differences in sample size between groups.



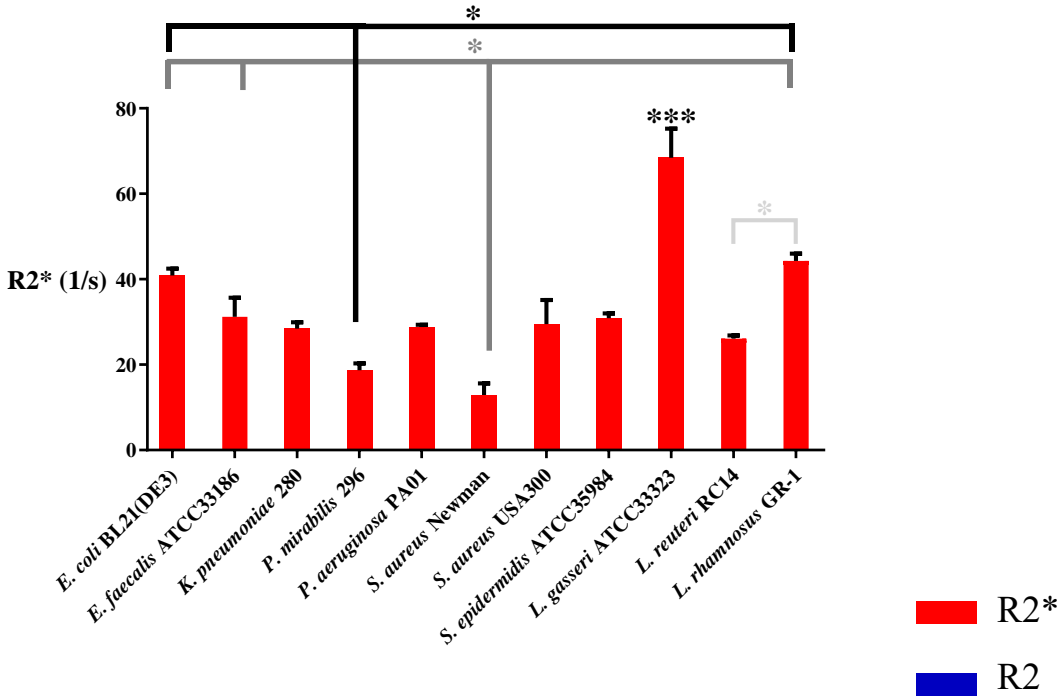
## **3.3 Results**

### **3.3.1 MR relaxation rates of examined bacteria**

Various commensal, probiotic and pathogenic bacteria were cultured and subjected to MRI. Transverse relaxation rates of *L. gasseri* ATCC33323 were significantly higher than all other species examined (Figure 16A and B;  $p < 0.001$ ). *Lactobacillus rhamnosus* GR-1 displayed higher transverse relaxivity than *L. reuteri* RC14, with higher R2 than *P. mirabilis* 296 and *S. aureus* Newman as well (Figure 16 A and B;  $p < 0.05$ ). *Proteus mirabilis* 296 and *S. aureus* Newman displayed low transverse relaxivity (Figure 16 A and B). Multiple *Lactobacillus* spp. demonstrated high transverse relaxation rates, with the signal intensity of *L. crispatus* ATCC33820 decaying before the first TE (13 ms), meaning the signal from these wells was much lower than other samples at TE = 13 ms and did not decrease further at higher TE, and thus preventing an accurate measurement (data not shown).

Longitudinal relaxation rates of *L. rhamnosus* GR-1 were significantly higher than all other non-lactobacilli examined (Table 8,  $p < 0.01$ ). *Lactobacillus gasseri* ATCC33323 displayed higher R1 than all non-lactobacilli except for *E. faecalis* 33186, while *L. reuteri* RC-14 displayed higher longitudinal relaxivity than *S. aureus* Newman, *P. mirabilis* 296 and *P. aeruginosa* PA01 (Table 8,  $p < 0.05$ ). These data suggest that R1 measurements may be useful for differentiating some lactobacilli from other bacterial species (Table 8). Raw MR data for all bacterial species examined are found in Appendix 12.

**A**



**B**

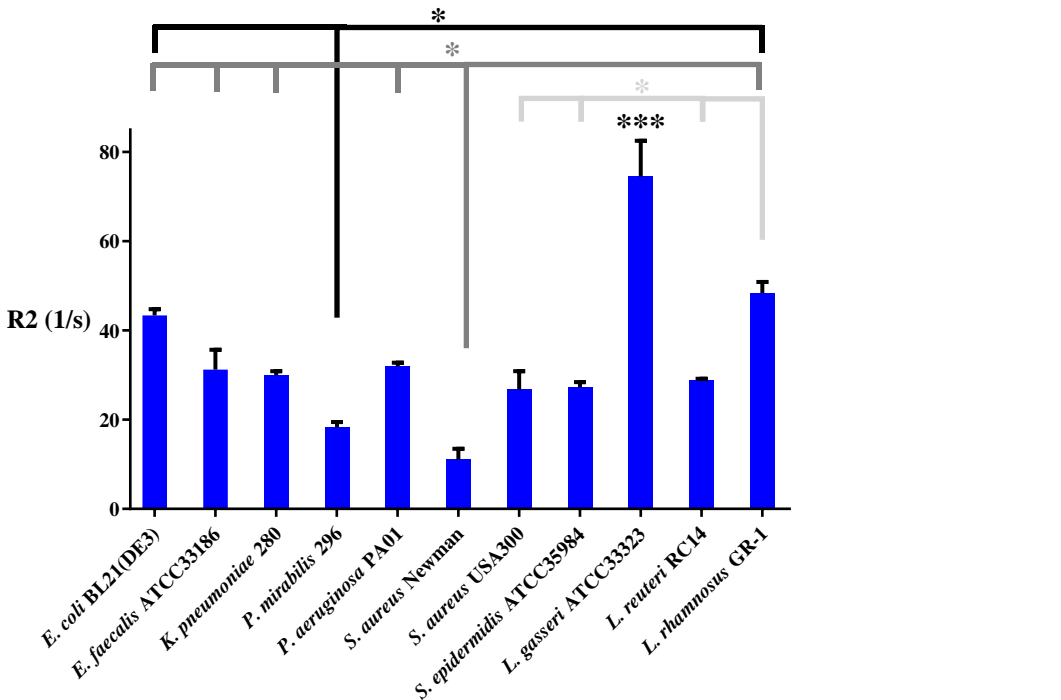


**Figure 16. MR measurements of different bacterial species vary widely.** Cultures from different bacterial species were mounted in a gelatin cell phantom for MRI at 3T. In all cases, the

R2 component of transverse relaxivity (blue bars, B) dominates the total R2\* signal (red bars, A). *Lactobacillus gasseri* ATCC33323 displayed significantly higher R2 and R2\* than any other species tested (A and B; \*\*\*  $p < 0.001$ ). *Lactobacillus rhamnosus* GR-1 displayed higher relaxivity than *L. reuteri* RC14, as well as higher R2 than *S. aureus* USA300 and *S. epidermidis* ATCC35984 (A and B; light gray lines;  $p < 0.05$ ). *P. mirabilis* 296 and *S. aureus* Newman displayed lower transverse relaxivity than several other species imaged (A and B; black and gray lines respectively). Bar graphs show mean  $\pm$  SEM ( $n = 3 - 5$ ).

**Table 8. Longitudinal relaxation rates for various bacterial species**

<b>Sample</b>	<b><sup>^</sup> R1 (s<sup>-1</sup>)</b>	<b>SEM (s<sup>-1</sup>)</b>	<b>n-value</b>
<i>P. aeruginosa</i> PA01	1.04 d	0.14	4
<i>S. epidermidis</i> ATCC35984	1.49 cd	0.07	4
<i>K. pneumoniae</i> 280	1.25 cd	0.01	3
<i>E. faecalis</i> ATCC33186	2.04 bcd	0.10	3
<i>P. mirabilis</i> 296	0.92 d	0.05	3
<i>S. aureus</i> USA300	1.37 cd	0.10	3
<i>S. aureus</i> Newman	1.17 d	0.15	4
<i>L. gasseri</i> ATCC33323	3.34 ab	0.32	5
<i>L. rhamnosus</i> GR-1	3.77 a	0.66	4
<i>L. reuteri</i> RC-14	2.60 abc	0.05	3

<sup>^</sup> Mean R1 values followed by the same letter are not significantly different ( $\alpha = 0.05$ ) based on Tukey's test.

### 3.3.2 Fe and Mn quantification in various bacterial species

Cell lysates of bacterial strains were examined using ICP-MS to quantify total cellular iron and manganese content and correlate these measures to MR relaxivity. Iron was below detectable levels in all samples of *Lactobacillus* spp. examined (Figure 17A). Both *S. aureus* Newman and *K. pneumoniae* 280 samples contained significantly more iron than lactobacilli (Figure 17A;  $p < 0.001$  and  $p < 0.05$  respectively). Manganese levels varied widely between bacteria, ranging from 0.014 – 111.9  $\mu\text{g Mn} / \text{mg protein}$  (Figure 17B). *Staphylococcus aureus* Newman contained more Mn than *P. mirabilis* 296, while all other significant differences were due to the high Mn of lactobacilli. *Lactobacillus rhamnosus* GR-1 and *L. crispatus* ATCC33820 had higher manganese than all non-*Lactobacillus* species except *S. epidermidis*. *Lactobacillus reuteri* RC-14 had significantly more Mn than *P. aeruginosa*, *K. pneumoniae* or *P. mirabilis*, while *L. gasseri* ATCC33323 only had significantly more Mn than *P. mirabilis* 296 (Figure 17B;  $p < 0.05$ ). Raw ICP-MS data are available in Appendix 13.

These data show that both Fe and Mn levels vary widely between different bacterial species, and Mn especially may contribute extensively to the high MR relaxation rates of *Lactobacillus* spp. However, the high R2 and R2\* of *L. gasseri* ATCC33323 cannot be fully attributed to Mn levels, which are relatively low for this strain.

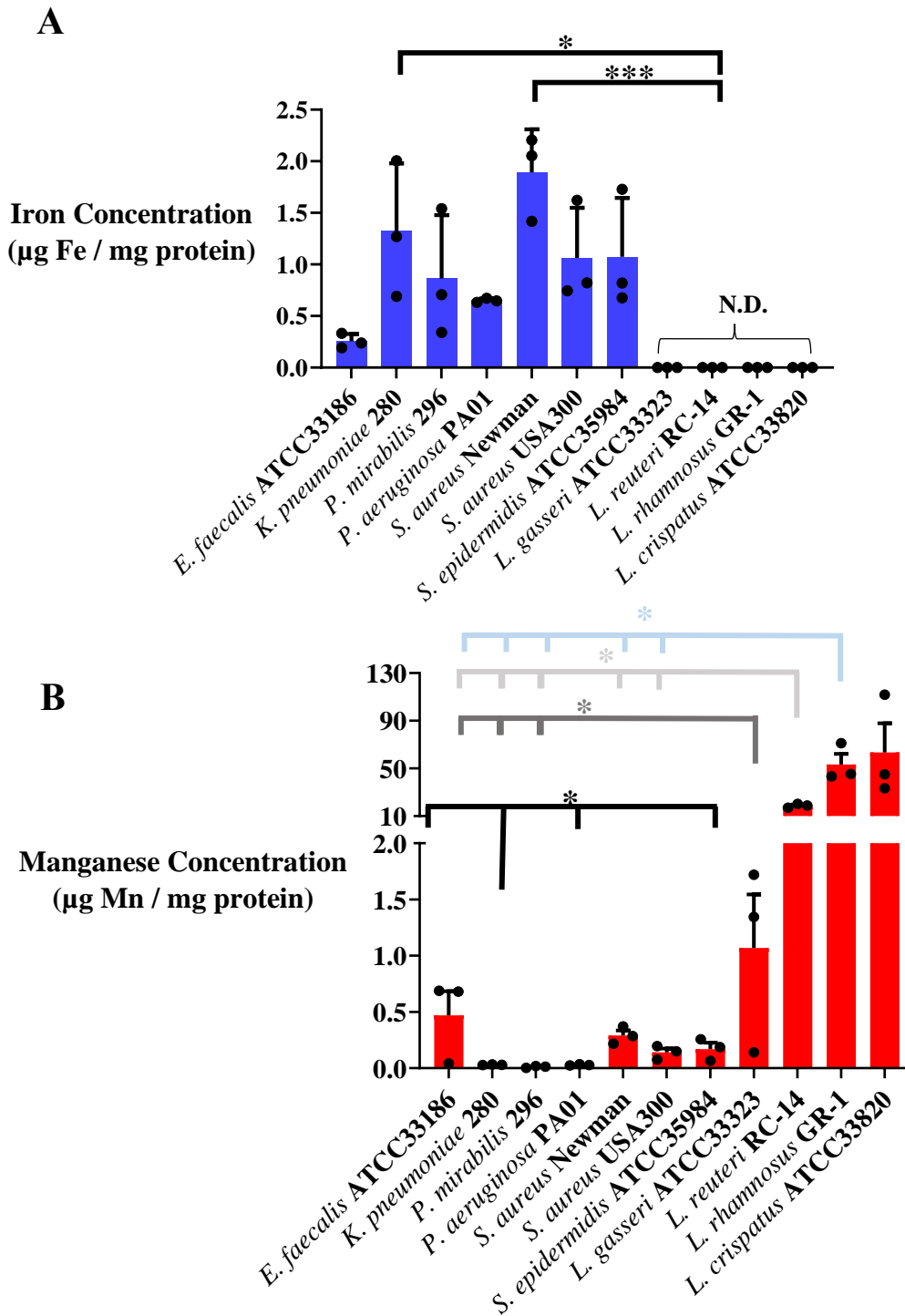


**Figure 17. Elemental iron and manganese content vary widely between bacterial species.** Iron and manganese were quantified by ICP-MS and normalized to total protein. Both iron (A, blue) and manganese (B, red) content varied between bacterial species. All lactobacilli examined contain extremely high levels of Mn, but undetectable Fe (N.D., not detectable). Data are

displayed as individual values with mean  $\pm$  SEM ( $n = 3$ ). In panel A, iron content of *S. aureus* Newman and *K. pneumoniae* were significantly higher than that of all lactobacilli examined (black lines, \*  $p < 0.05$ , \*\*\*  $p < 0.001$ ). In panel B, the Kruskal-Wallis test with Dunn's multiple comparisons showed that *P. mirabilis* contained less Mn than *E. faecalis*, *S. aureus* Newman, and *L. gasseri* (black lines) and *L. reuteri*, *L. rhamnosus* and *L. crispatus* samples each contained more manganese than most other bacterial species examined (dark gray, light gray and light blue lines respectively).

### 3.3.3 Measuring MR relaxivity of *L. crispatus* ATCC33820

As mentioned in section 3.3.1, the signal intensity of *L. crispatus* ATCC33820 decayed to baseline before the first TE, preventing the measurement of MR relaxation rates in a compact pellet. To overcome the rapid signal decay, *L. crispatus* was serially diluted in 4 % gelatin / PBS so that signal intensity could be measured before it decayed completely. Following a ½ dilution, signal intensity still decayed to background levels by the third TE (25 ms) but R2 and R2\* were nevertheless measurable. Indeed, since transverse relaxation rates were more reliable as the dilution factor increased, this suggests that *L. crispatus* may be detected by MRI even when relatively few cells are present (Figures 18 and 19).

Longitudinal relaxivity does not vary significantly in samples containing 25-50% *L. crispatus* ATCC33820, however R1 in samples diluted 1/8 was significantly lower than those diluted 1/4 (Table 9,  $p < 0.01$ ). When *L. crispatus* represented less than 10% of the total sample (1/16 dilution), R1 was significantly lower than all other dilutions examined (Table 9,  $p < 0.001$ ). Individual transverse and longitudinal relaxation rate measurements are found in Appendix 14.

Since the number of CFUs within the MR slice varies with each replicate, we explored the correlation between number of CFUs in the MR slice (where the signal is acquired) and its relaxation rate. Both R2 and R2\* show moderate positive linear correlations to the number of live cells (Figure 19A and B;  $p < 0.001$ ). Thus, as the number of live cells in the ROI increases, so do the MR measurements.

On the other hand, R2 and R2\* of *L. crispatus* ATCC33820 were strongly correlated to the percentage of cells in the sample (Figure 20). Based on these strong positive correlations and using the linear regression equations, we estimate that R2 for undiluted *L. crispatus* (where  $f = 100\%$ ) is  $\sim 308\text{ s}^{-1}$  and R2\* is  $\sim 339\text{ s}^{-1}$ . These estimated values are at least 3 -fold higher than any other species examined, explaining the initial difficulties in measuring MR parameters for *L. crispatus* ATCC33820.

Based on the moderate, positive linear correlation between CFUs in the slice and fraction of cells, we can estimate the average number of CFUs required to fill the Ultem well at any dilution factor (Figure 21). For example, if we were not diluting, but using 100% *L. crispatus*, the MR



slice would be comprised of  $\sim 9.51 \times 10^9$  CFUs, with  $\sim 2.85 \times 10^{10}$  CFUs needed to fill the entire well. Overall, these *L. crispatus* dilution experiments demonstrate that a commensal bacterium of the urogenital tract may be a good target for *in vivo* imaging of bacteria using MRI.

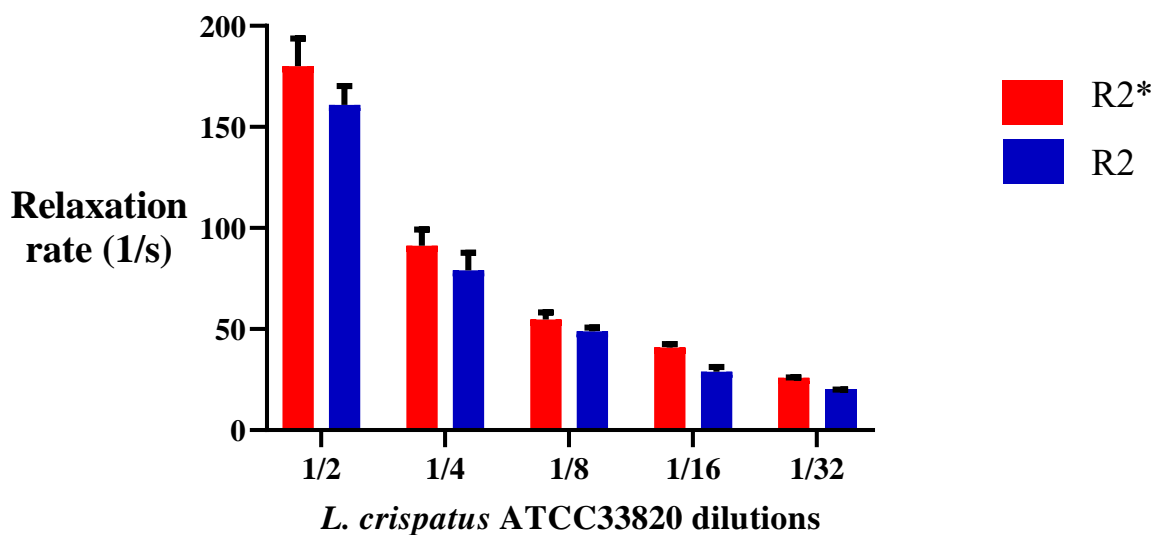


**Figure 18. Transverse relaxivity of serially diluted *L. crispatus* ATCC33820.** *Lactobacillus crispatus* displays high transverse relaxation rates after dilution in gelatin / PBS. Bar graphs show the mean +/- SEM (n = 5, except at 1/32 n = 2). Samples diluted 1/2 contain approximately  $2.02 \times 10^{10}$  CFUs within the MR slice; the 1/4 dilution contains  $\sim 1.01 \times 10^{10}$  CFUs / slice; the 1/8 dilution contains  $\sim 5.05 \times 10^9$  CFUs / slice; the 1/16 dilution contains  $\sim 2.53 \times 10^9$  CFUs / slice; and 1/32 diluted samples contain  $\sim 7.83 \times 10^7$  CFUs / slice.

**Table 9. Longitudinal relaxation rates for serially diluted *L. crispatus* ATCC33820**

<b>Sample <sup>a</sup></b>	<b>Average CFUs / MR slice</b>	<b><sup>^</sup> R1 (s<sup>-1</sup>)</b>	<b>SEM (s<sup>-1</sup>)</b>	<b>n-value</b>
<b>1/2 <i>L. crispatus</i></b>	2.02 x 10 <sup>10</sup>	3.74 ab	0.25	4
<b>1/4 <i>L. crispatus</i></b>	1.01 x 10 <sup>10</sup>	4.06 a	0.14	5
<b>1/8 <i>L. crispatus</i></b>	5.05 x 10 <sup>9</sup>	3.22 b	0.11	5
<b>1/16 <i>L. crispatus</i></b>	2.53 x 10 <sup>9</sup>	1.94 c	0.06	5

<sup>a</sup> All samples were serially diluted in 4% gelatin / PBS

<sup>^</sup> Mean R1 values followed by the same letter are not significantly different ( $\alpha = 0.05$ ) based on Tukey's test.

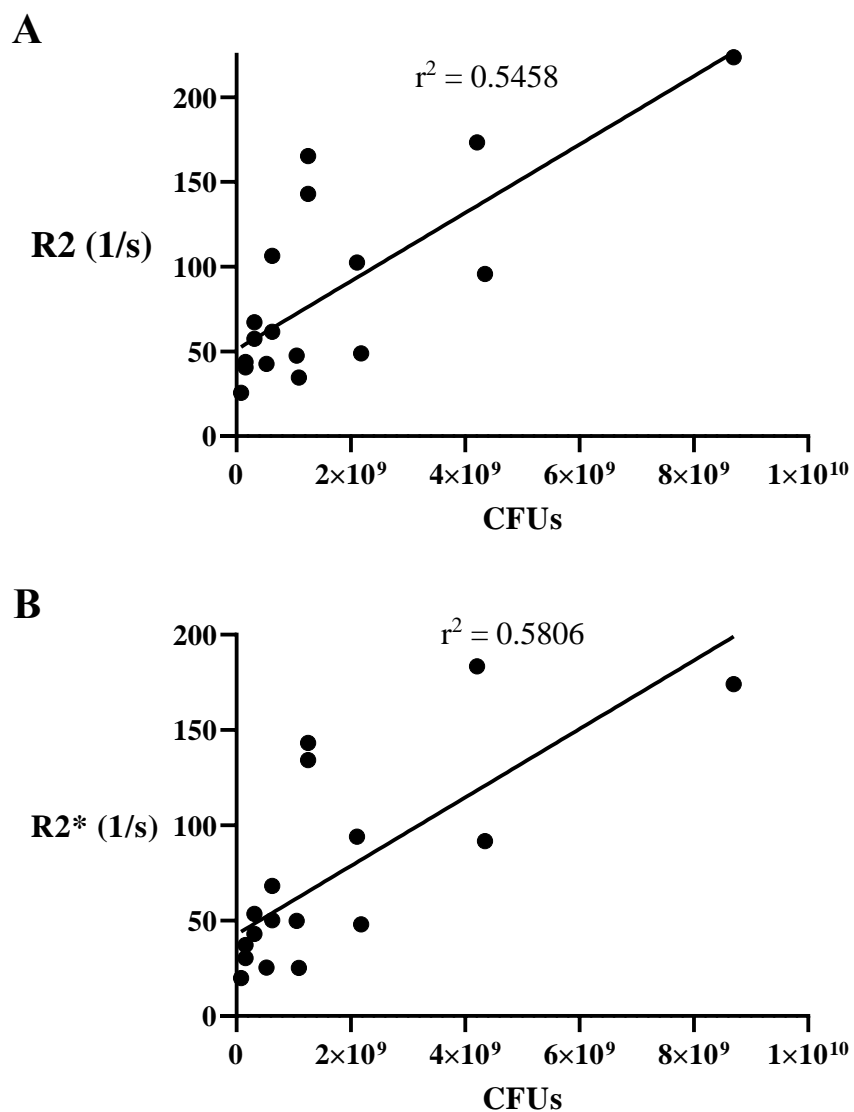


**Figure 19. MR measures of *L. crispatus* ATCC33820 are moderately correlated to number of live cells.** Plots of R2 (A) and R2\* (B) show individual MR measures and cell number expressed as CFUs within each MR slice. For both R2 and R2\*, Pearson's line of best fit provides a moderately positive linear correlation between number of CFUs and transverse relaxation rate ( $p < 0.001$ ).

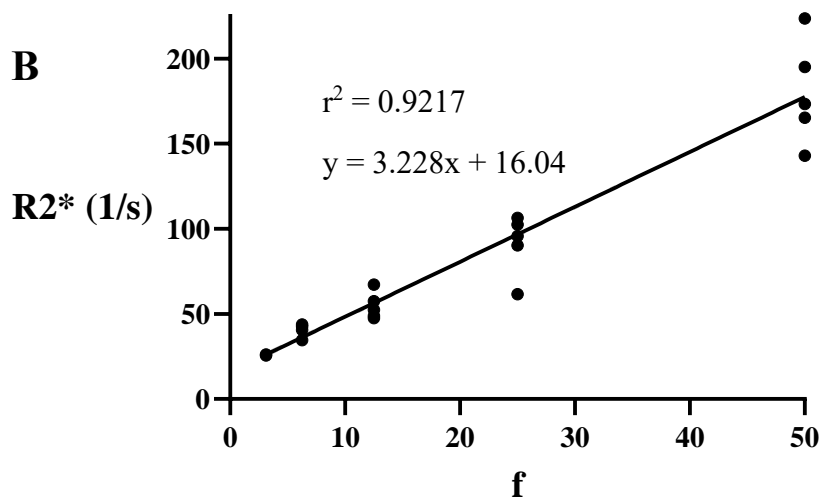
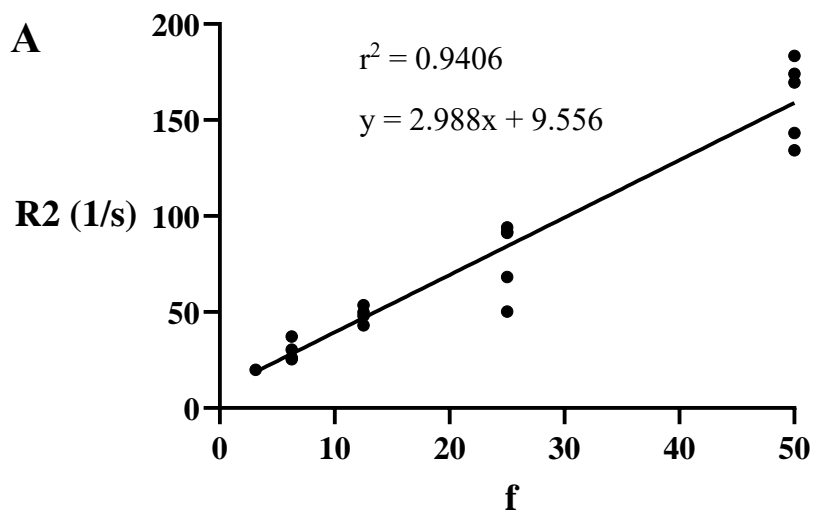


**Figure 20. MR measures vs. fraction of cells (f) for serially diluted *L. crispatus* ATCC33820.** Fraction of *L. crispatus* cells (f), shown as a percentage, is strongly correlated to R2 (A) and R2\* (B) measurements ( $p < 0.001$ ).

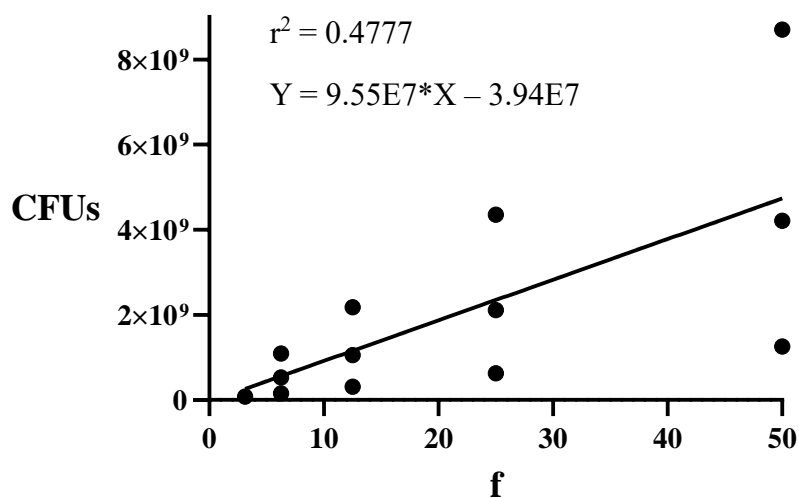


**Figure 21 Percent of *L. crispatus* ATCC33820 cells (f) are moderately correlated to number of live cells.** Circles show colony forming unit counts (CFUs) within the MR slice (21 voxels in a 3 mm slice through the well  $\approx 38 \text{ mm}^3$ ) of individual samples as a function of the percentage of cells (f) loaded into the wells after serial dilution in gelatin/PBS. The line represents a moderate, positive linear correlation between CFUs and f ( $p < 0.01$ ). The scatter plot shows the range in number of live cells that may contribute to the MR signal in any given well of the cell phantom, irrespective of dilution factor. The line of best fit shows the average number of live cells required to fill the MR slice at any given dilution factor.

### 3.3.4 MRI signal from mixtures of human bladder cells and *L. crispatus*

To explore the potential for distinguishing MR relaxivity in two distinct cell types within a single sample, we examined mixtures of human 5637 bladder cells and *L. crispatus* ATCC33820 at varying ratios. From the decay curves, it is apparent that transverse relaxivity in these mixed samples is mono-exponential and not bi-exponential (Figure 22). These data show that, using our MR sequences and analysis techniques, we were unable to resolve the bacterial and mammalian MR signals (Figure 22).

In addition, the mono-exponential decay of these mammalian and bacterial cell mixtures shows that  $R2^*$  values are similar to those of *L. crispatus* alone, diluted in gelatin. However,  $R2$  values are markedly lower than those measured in purely bacterial phantoms (compare Figures 18 and 23). Thus, while *L. crispatus* diluted in gelatin has little to no  $R2'$  component, when diluted in the presence of bladder cells, the  $R2^*$  signal consists of approximately half  $R2$  (the irreversible component of transverse relaxivity) and half  $R2'$  (the reversible component of transverse relaxivity).

$R2^*$ ,  $R2$  and  $R2'$  of human 5637 bladder cells alone are also quite substantial ( $R2^* = 22.01 \text{ s}^{-1}$ ). For comparison, human melanoma MDA-MB-435 cells have  $R2^*$  of  $13.70 \text{ s}^{-1}$ <sup>32</sup> and mouse embryonic adenocarcinoma P19 cells have  $R2^*$  of  $13.5 \text{ s}^{-1}$ <sup>34</sup>. These are nevertheless much lower than transverse relaxation rates of the lactobacilli, with  $R2^*$  of  $180 \text{ s}^{-1}$  when diluted 1/2 in gelatin. Raw transverse relaxation rate measurements are shown in Appendix 15.

$R2$ ,  $R2^*$  and  $R2'$  are strongly linearly correlated to the fraction of *L. crispatus* ATCC33820 cells in mixed samples (Figure 24). When comparing the linear regression slope of transverse relaxivity with fraction of *L. crispatus* either diluted in gelatin or in 5637 bladder cells,  $R2$ , but not  $R2^*$ , signal attenuation by bladder cells is demonstrated by the moderate slope of the mixed sample compared to the steep slope of the gelatin-diluted *L. crispatus* (Figure 25).  $R2/R2^*$  ratios of *L. crispatus* diluted in bladder cells are significantly lower than those diluted in gelatin (Table 11;  $p < 0.001$ ). Longitudinal relaxation rates of mixed bladder cell and *L. crispatus* samples (Table 10) are also attenuated in comparison to *L. crispatus* diluted in gelatin (Table 9).

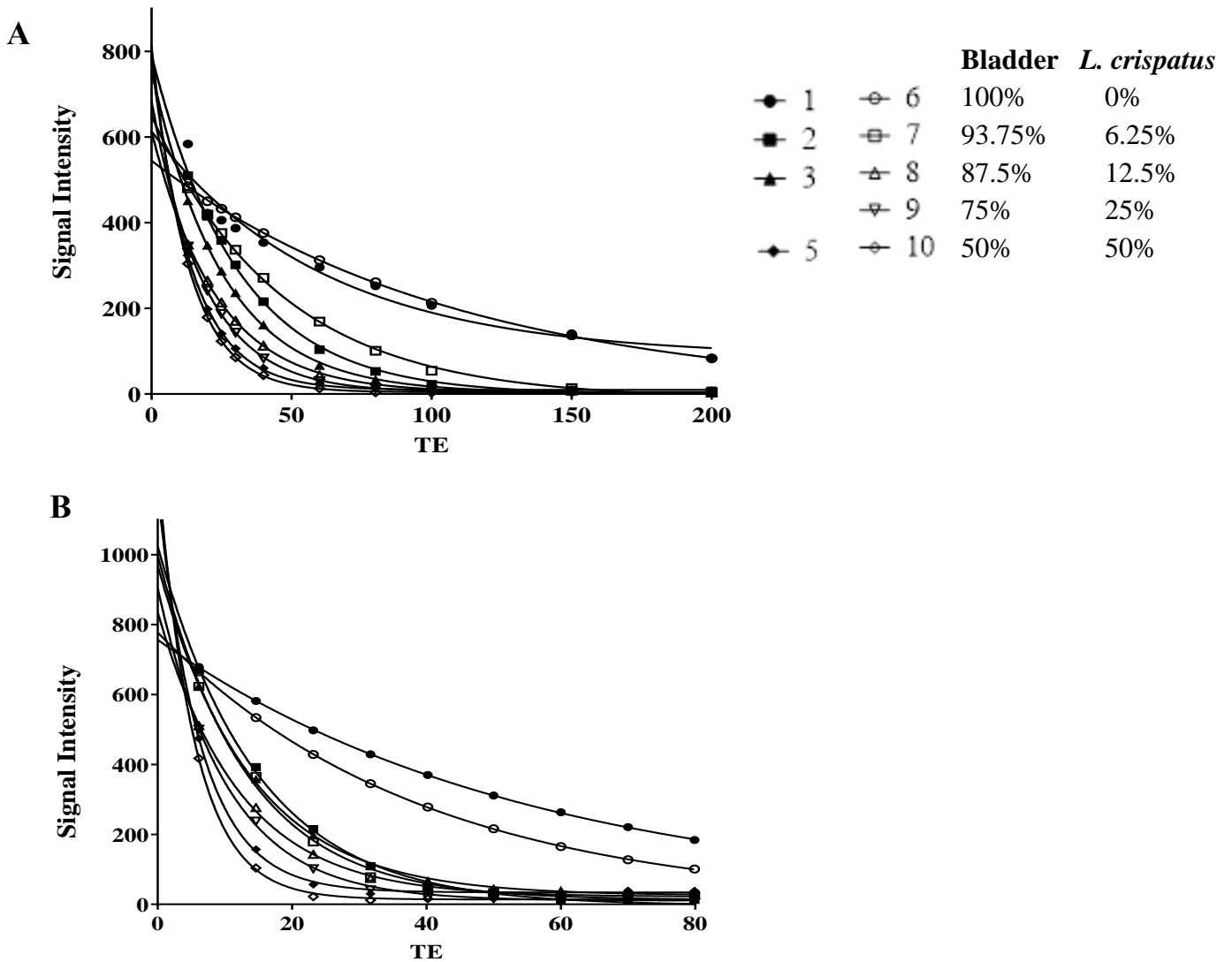


**Figure 22. Signal intensity decays mono-exponentially with echo time (TE) in mixed samples of 5637 bladder cells and *L. crispatus* ATCC33820.** The decay of T2 (A) and T2\* (B) fits a mono-exponential curve, providing little or no distinction between mammalian and bacterial MR contributions. Open and closed circles (lines 1 and 6) show the signal decaying in bladder cells alone; open and closed squares (lines 2 and 7) show the signal decaying in bladder cells mixed with 1/16 *L. crispatus*; open and closed triangles (lines 3 and 8) show the signal decaying in bladder cells mixed with 1/8 *L. crispatus*; inverted triangles (line 9) show the signal decaying in bladder cells mixed with 1/4 *L. crispatus*; open and closed diamonds (lines 5 and 10) show the signal decaying with equal amounts of mammalian and bacterial cells (i.e. 1/2 *L. crispatus*).



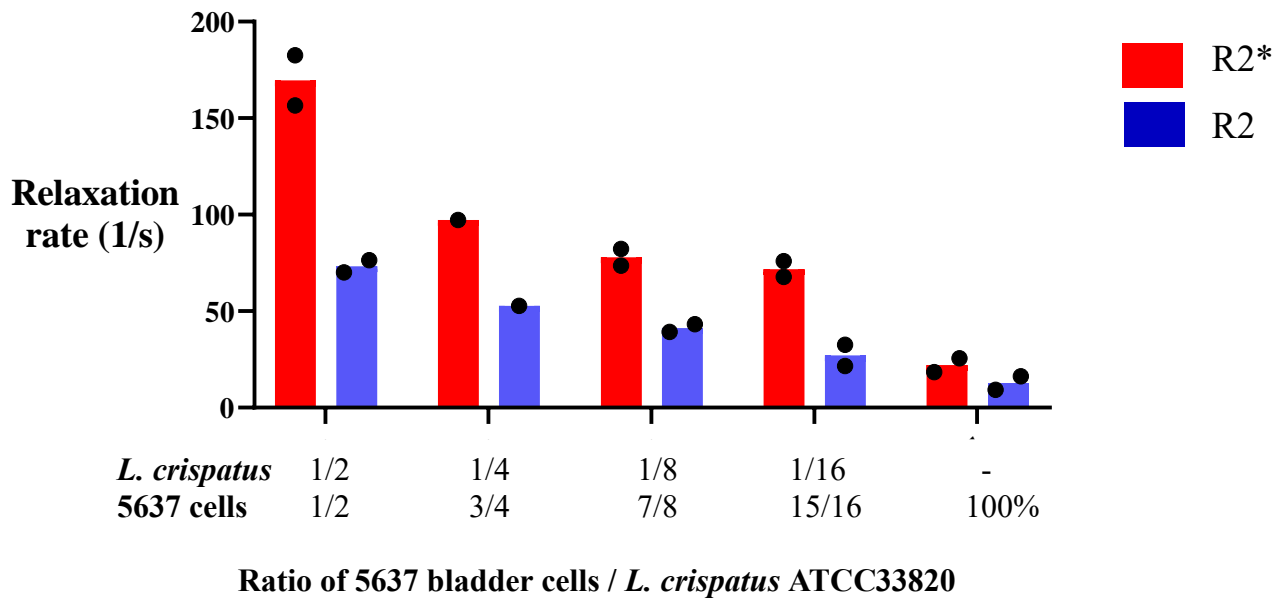


**Figure 23. Transverse relaxation rates in serial dilutions of 5637 bladder cells and *L. crispatus* ATCC33820.** Cultured cells were resuspended in PBS before serially diluting *L. crispatus* cells in human bladder cells. Cell mixtures were packed into Ultem wells by centrifugation and mounted in a cell phantom for MRI at 3T. Bar graphs show the influence of increasing proportions of *L. crispatus* on bladder cell transverse relaxation rates. Irrespective of dilution, R2 (blue bar) measurements are approximately half of the R2\* signal (red bar) compared to *L. crispatus* alone (Figure 17). In this respect, *L. crispatus* appear to contribute more to the total transverse relaxation rate (R2\*) than to the irreversible component (R2). Bar graphs show the mean transverse relaxivity; individual relaxation rate values are indicated with black circles (n = 1 – 2). For a 1/2 dilution, the mean *L. crispatus* CFUs in the MR slice is  $3.46 \times 10^8$ ; for 1/4, it is  $1.99 \times 10^8$  CFUs / slice; for 1/8, it is  $1.07 \times 10^7$  CFUs / slice; for 1/16, it is  $6.39 \times 10^7$  CFUs / slice. Median number of bladder cells in the slice for a 1/2 diluted sample is  $6.03 \times 10^6$  cells / slice; the 3/4 sample contains  $7.54 \times 10^6$  bladder cells; the 7/8 sample contains  $8.48 \times 10^6$  bladder cells; the 15/16 sample contains  $1.05 \times 10^7$  bladder cells; and the 100% bladder cell sample contains  $2.14 \times 10^7$  cells.

**Table 10. Longitudinal relaxation rates of mixed samples of 5637 bladder cell and *L. crispatus* ATCC33820**

Sample	<sup>a</sup> <i>L. crispatus</i> CFUs / slice	<sup>a</sup> 5637 cells / slice	R1 values (s <sup>-1</sup> )	
			Sample 1	Sample 2
<b>1/2 <i>L. crispatus</i>, 1/2 5637 cells</b>	346 x 10 <sup>6</sup>	6.03 x 10 <sup>6</sup>	2.43	2.41
<b>1/4 <i>L. crispatus</i>, 3/4 5637 cells</b>	199 x 10 <sup>6</sup>	7.54 x 10 <sup>6</sup>	2.41	2.41
<b>1/8 <i>L. crispatus</i>, 7/8 5637 cells</b>	107 x 10 <sup>6</sup>	8.48 x 10 <sup>6</sup>	1.79	1.87
<b>1/16 <i>L. crispatus</i>, 15/16 5637 cells</b>	63.9 x 10 <sup>6</sup>	10.5 x 10 <sup>6</sup>	1.77	1.38
<b>5637 cells alone</b>	0	21.4 x 10 <sup>6</sup>	0.69	0.70

<sup>a</sup> Counts are displayed as the median of 2 replicates.

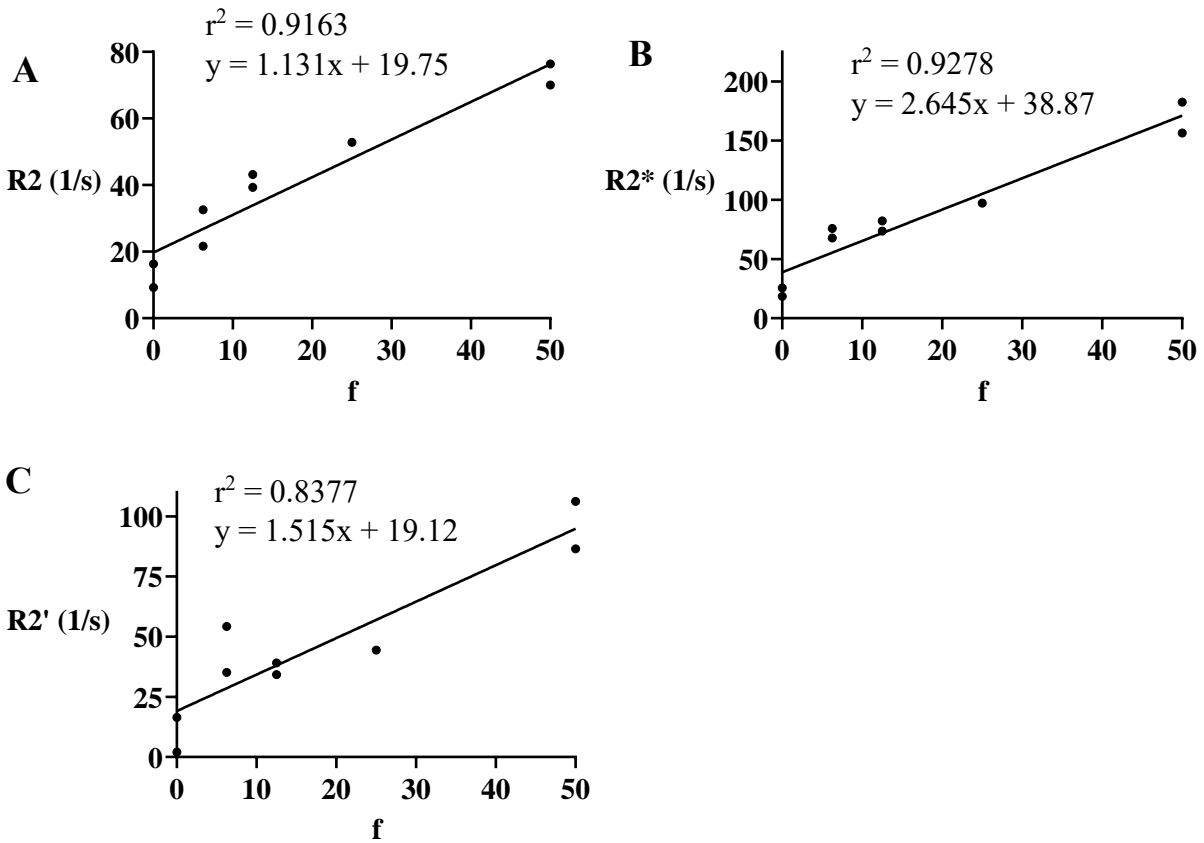


**Figure 24. Transverse relaxivity vs. fraction of bacterial cells (f) for *L. crispatus* ATCC33820 serially diluted in 5637 bladder cells. Fraction of *L. crispatus* cells is strongly positively correlated to R2 (A), R2\* (B) and R2' (C) measurements.**

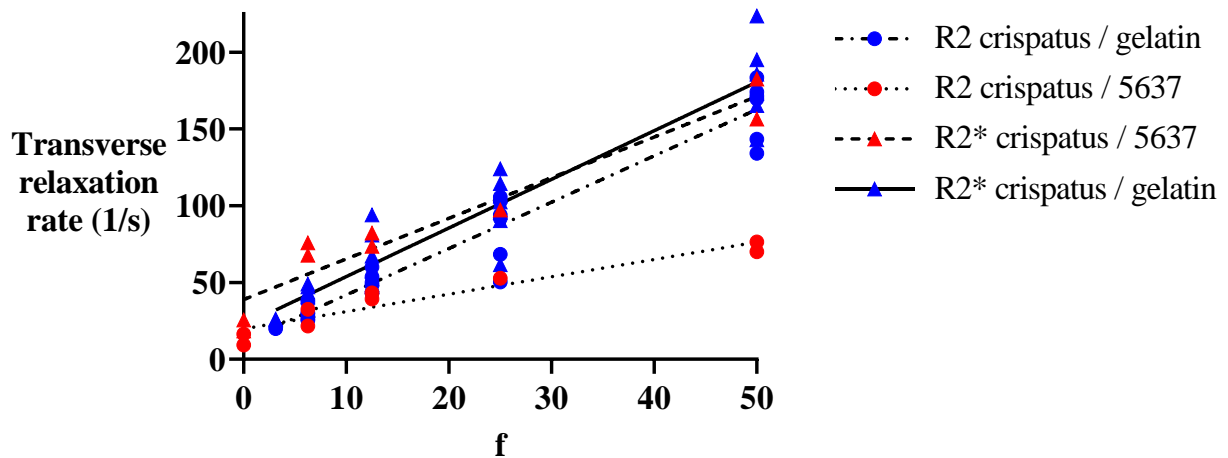


**Figure 25. R2\* and R2 vs. fraction of bacterial cells (f) for *L. crispatus* ATCC33820 serially diluted in 5637 bladder cells or gelatin.** Fraction of *L. crispatus* is strongly correlated to MR measures: R2\* (squares) and R2 (circles). Red symbols denote mixed samples of *L. crispatus* and 5637 cells; blue symbols denote *L. crispatus* diluted in gelatin. Lines demonstrate the linear regression within each sample type and MR measure. Individual Pearson correlation coefficients can be found in Figures 18 A and B as well as Figure 23 A and B, though all  $r^2 > 0.91$ . Fraction of live *L. crispatus* cells is strongly positively correlated to transverse relaxivity whether diluted in gelatin or bladder cells. In the presence of bladder cells, R2, but not R2\* relaxivity is attenuated, giving rise to a prominent R2' component.

**Table 11. R2/R2\* ratios for *L. crispatus* ATCC33820 dilutions**

<i>L. crispatus</i> <sup>a</sup>	50%	25%	12.5%	6.25%	3.125%	<sup>d</sup> Mean R2 / R2*	SD	p-value
<b>Gelatin</b> <sup>b</sup>	1.06	0.92	1.05	0.60	0.78	0.84	0.13	< 0.001
	0.78	0.96	0.98	0.73	0.77			
	0.87	1.01	0.96	0.61	-			
	0.94	0.64	0.80	0.85	-			
	0.87	0.82	0.75	0.75	-			
<b>5637 cells</b> <sup>c</sup>	0.45	0.54	0.53	0.48	0.89	0.50	0.17	
	0.42	-	0.52	0.29	0.36			

<sup>a</sup> *L. crispatus* samples are displayed as the percent bacterial cells within the sample.

<sup>b</sup> *L. crispatus* cells were serially diluted in gelatin/PBS (n = 22)

<sup>c</sup> *L. crispatus* cells were serially diluted in 5637 bladder cells (n = 9)

<sup>d</sup> R2/R2\* ratios between *L. crispatus*/gelatin and *L. crispatus*/5637 cells were compared using the unpaired Mann-Whitney test.

### **3.3.5 Effect of iron acquisition mutations on MR relaxation rates and cellular iron and manganese content**

To explore how iron storage in the form of ferritin contributes to MR relaxation rates of bacteria, we examined *S. aureus* USA300 and two related iron acquisition mutants. We assessed wildtype (WT) USA300 as well as a mutant deficient in the siderophores staphyloferrin A and staphyloferrin B ( $\Delta sfa/\Delta sbn$ ). In addition, we examined a ferritin A deletion mutant bearing the siderophore deficient background ( $\Delta sfa/\Delta sbn/\Delta ftnA$ ). All 3 bacterial strains were grown in iron-replete and iron depleted media.

Both *S. aureus* iron mutants displayed similar MR relaxation rates as the wild type when grown in iron-rich broth (Figure 26A). Under conditions of iron starvation, the transverse relaxivity did not change (Figure 26A and B). Longitudinal relaxivity was likewise unchanged in both iron replete and iron depleted media (Table 12). Neither siderophore deficiency nor lack of ferritin A storage protein altered the MR relaxation rates (Figure 26B, Table 12), suggesting that other forms of iron uptake and storage may be compensating for these mutations. Iron content may vary between these *S. aureus* mutants (Figure 27A), with little or no change in total cellular manganese content under iron depleted conditions (Figure 27B). Raw MR and ICP-MS data are available in Appendices 16 and 17 respectively.

Overall these data indicate that defects in ferritin iron storage and transient redox active iron do not affect MR relaxation rates in *S. aureus*.

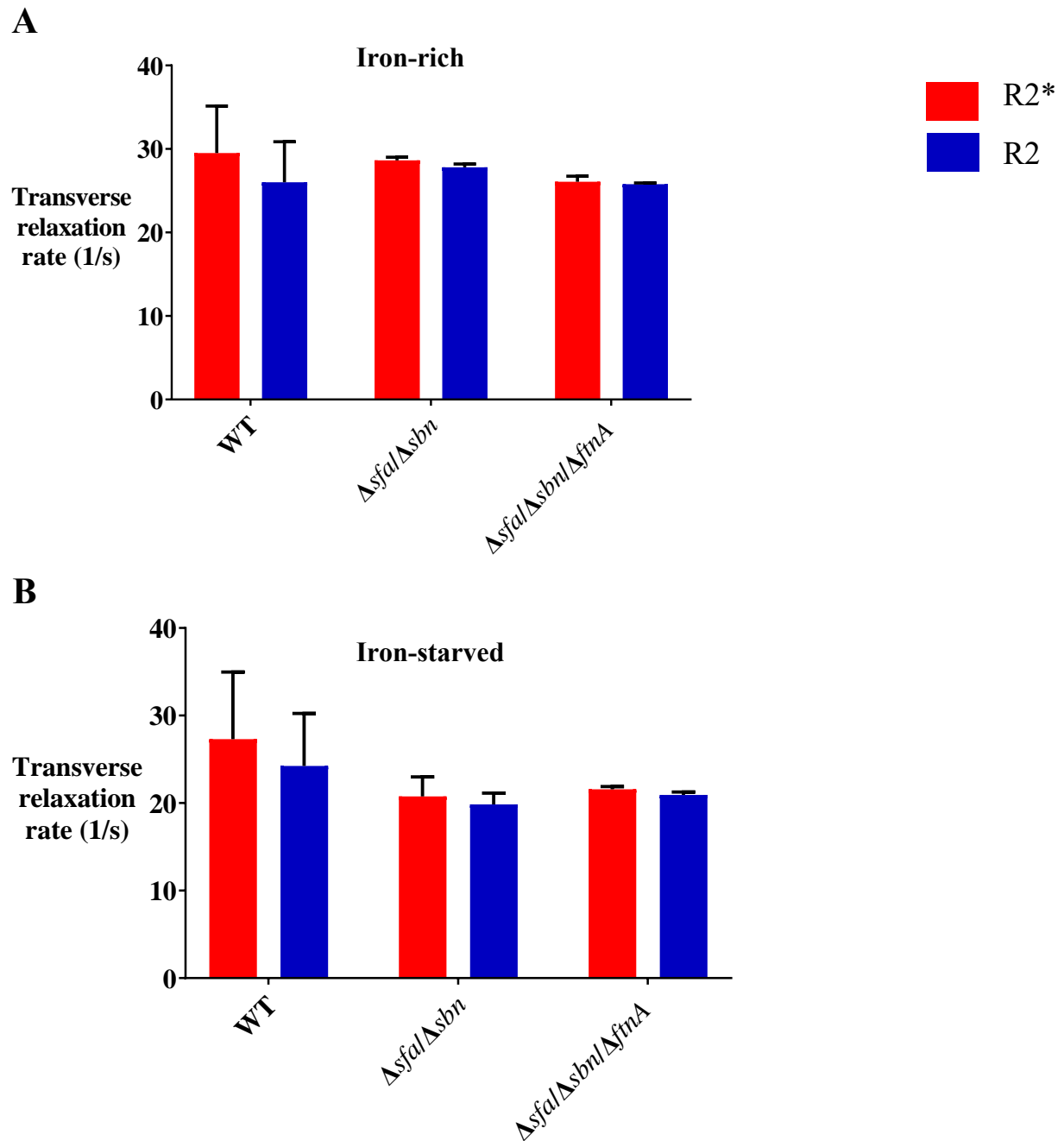


**Figure 26. Transverse relaxation rates for *S. aureus* USA300 iron mutants grown under iron-replete and iron depleted conditions.** Wildtype (WT), siderophore deficient ( $\Delta sfa/\Delta sbn$ ) and siderophore deficient, ferritin A deletion ( $\Delta sfa/\Delta sbn/\Delta ftnA$ ) mutants were grown in either iron-replete (A) or iron depleted (B) medium and examined by MRI. Mutations in these select iron acquisition genes do not alter transverse relaxation rates in *S. aureus* USA300 (n = 3, except for mutants in the iron-replete condition where n = 2).

**Table 12. Longitudinal relaxation rates for *S. aureus* USA300 and iron acquisition mutants**

<b>Strain</b>	<b>R1 (s<sup>-1</sup>)</b>	<b>SEM (s<sup>-1</sup>)</b>	<b>n-value</b>
WT <sup>a</sup>	1.37	0.10	3
WT <sup>b</sup>	1.22	0.06	3
<i>Δsfa/Δsbn</i> <sup>b</sup>	1.20	0.06	3
<i>Δsfa/Δsbn/ΔftnA</i> <sup>b</sup>	1.32	0.09	3

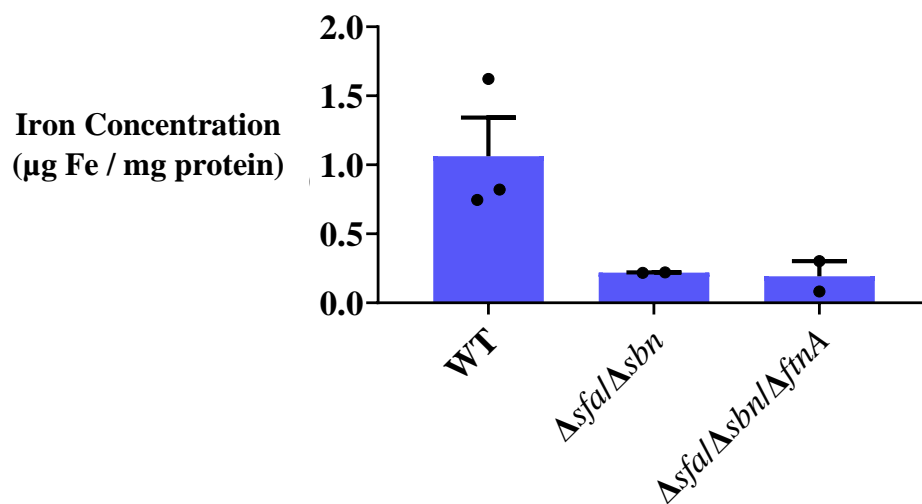
<sup>a</sup> Bacteria were cultured in iron-replete medium.

<sup>b</sup> Bacteria were cultured in iron depleted medium.

WT, wildtype



**A**



**B**

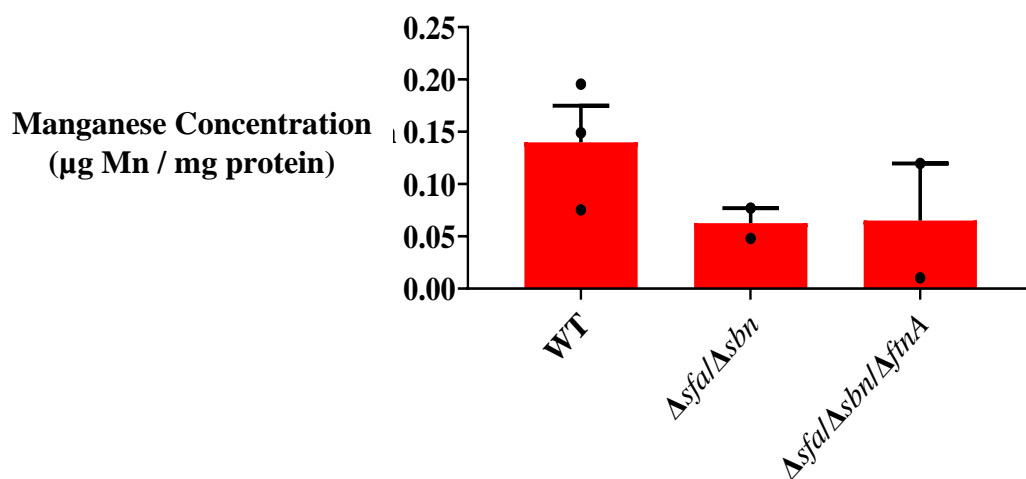


**Figure 27. Iron and manganese content in *S. aureus* USA300 iron acquisition mutants grown in iron depleted conditions.** Staphyloferrin A and B deficiency ( $\Delta sfa/\Delta sbn$ ) and ferritin deletion, siderophore deficient ( $\Delta sfa/\Delta sbn/\Delta ftnA$ ) mutants grown in iron-starved conditions may have lower total cellular iron content but similar manganese content than wildtype (WT) bacteria when grown in iron-rich conditions (n = 2 – 3).

### **3.4 Discussion**

Using a gelatin cell phantom, we explored the MR relaxation rates of various commensal, probiotic and pathogenic bacteria encountered in the urogenital tract. We found high variability in transverse relaxivity, with MR signatures of *Lactobacillus* spp. dominating. Overall, there was little variability in iron content, but large variability in manganese content between bacterial species. The commensal and probiotic lactobacilli were characterized by extremely high manganese content which may be contributing to high transverse relaxivity since iron content in these species was below the ICP-MS detection limit.

Regardless of the high variability in transverse relaxivities among different species of bacteria, many of these measures are much higher than previously recorded in mammalian cells<sup>32, 34</sup>. Interestingly, all bacteria examined display little to no R2' component (R2\* - R2). We suggest that exploring differences in the form of metals (protein-bound, sequestered metals compared to free redox active forms) within a cell may be informative and help us fully understand the breakdown of transverse relaxivity components. As discussed in section 2.4, the SE and GRE sequences we used may contain systematic errors that led to R2\* < R2. In future work further refinement of the pulse sequence parameters as well as comparison with other MR sequences should be considered prior to making measurements aimed to define differences in R2 and R2\* relaxivity of bacteria.

High transverse relaxation rates of *L. crispatus* ATCC33820 may allow easier detection of this bacterium even at lower MRI field strength, since R2 and R2\* are generally proportional to field strength<sup>35</sup>. Furthermore, given the moderate positive correlation between MR parameters and number of CFUs, *in vivo* imaging of *L. crispatus* ATCC33820 and estimation of the number of live cells within an ROI should be feasible. For example, fewer than 10<sup>8</sup> CFUs of *L. crispatus* within an ~38 mm<sup>3</sup> ROI provides a measurable MR signal (greater than most mammalian tissues but low enough to enable relaxivity measurements), with estimated R2 values above 25 s<sup>-1</sup> and within the detectable range of current 3T clinical scanners. Using our current MR sequences it would be near impossible to directly measure transverse relaxivity of undiluted *L. crispatus* as its signal intensity decays within milliseconds, with estimated R2 exceeding 300 s<sup>-1</sup>. This would be a problem rarely encountered in healthy individuals *in vivo* where bacteria are more

homogeneously distributed within their niches. In the future, technological advancements in MRI should enable even better resolution for detection of fewer bacteria and newer sequences like ultrashort echo time (UTE) sequences may be useful in visualizing the fast signal decay for bacteria with large  $R_2$ <sup>36</sup>.

Iron levels vary widely between bacteria, but undetectably low iron was seen in all lactobacilli. Likely, this is because *Lactobacillus* spp. don't generally use iron as a cofactor<sup>27, 31, 37</sup>. This provides a growth advantage to them in the low iron environments of the urogenital tract. However, during menses when iron levels are increased, some lactobacilli such as *Lactobacillus iners* continue to thrive, whereas *L. crispatus* levels generally decrease and recover only as iron levels decrease<sup>38, 39</sup>. Previous research suggests that low molecular weight species of manganese play a role in blocking the production of reactive oxygen species and prevent lipid peroxidation, allowing lactobacilli to safely accumulate high levels of intracellular Mn<sup>31, 40</sup>. Large amounts of iron, on the other hand, lead to increased production of free radicals which can lead to DNA damage and lipid peroxidation which are harmful to cells<sup>41</sup>. Thus, it is not surprising that there is high manganese uptake in all our examined lactobacilli, as their growth medium, MRS, contains approximately 330  $\mu\text{M}$  Mn<sup>31</sup> whereas manganese levels in LB are approximately 1000-fold less (closer to 200 nM<sup>42</sup>). While manganese is a required cofactor in many bacteria, including lactobacilli<sup>30, 37</sup>, high Mn in our samples may be bound externally to the cell membrane or peptidoglycan as well as internalized. Lactobacilli are known to bind some heavy metals like cadmium, lead and mercury<sup>16</sup>. The possibility that manganese is also externally bound cannot be discerned from our study though this has not been previously observed in these bacteria. A preliminary genome search of *L. crispatus* ATCC33820 indicates the presence of non-specific metal transporters which may have the ability to import Mn (data not shown). There is also a manganese transporter, MtsA, conserved across *Streptococcus* spp. among others, including some *Lactobacillus* strains<sup>30, 43</sup>.

Although we hypothesize that high Mn content in lactobacilli is promoting high MR relaxivity, there is a discrepancy between elemental Mn levels and transverse relaxation rates in the species tested. For example, *L. gasseri* ATCC33323 has an  $R_2$  value of approximately 75 s<sup>-1</sup> while *L. rhamnosus* GR-1 has a lower  $R_2$  of ~48 s<sup>-1</sup>, although these MR signatures are not significantly different, total cellular Mn content varies significantly with that of GR-1 approximately 50-fold

higher than that of *L. gasseri* (~53  $\mu\text{g Mn / mg protein}$  versus ~1  $\mu\text{g Mn / mg protein}$ , respectively). Since higher manganese does not necessarily equate to higher transverse relaxivity, and we see that iron content is negligible, other factors appear to be at play. These factors may include, but are not limited to, bacterial size and morphology relating to the density of packed cells within an ROI, water content of samples, as well as the presence of other MR sensitive elements that we did not assess, including nickel, cobalt and gadolinium. Although gadolinium is not typically found in bacteria, genomes of certain species including *Salmonella enterica*, *Campylobacter jejuni* and *Bacillus subtilis* are known to encode nickel and/or cobalt transport genes<sup>44</sup>.

*In vivo*, MRI voxels will generally contain both bacterial and mammalian cells since few bacteria are free floating within the human microbiota and bacteria can adhere to mammalian tissues via pili as well as biofilm formation on mammalian structures and abiotic materials such as catheters or stents<sup>45</sup>. Although microbial diversity varies between each microenvironment<sup>46</sup>, all clinical microbiota samples are mixed, as various species live symbiotically. Therefore, it is important to assess how MR relaxivity changes in response to mixed bacterial samples and bacterial/mammalian mixtures compared to single strain cultures. In this study, we assessed mixed samples of *L. crispatus* ATCC33820 and human 5637 bladder cells using an MRI cell phantom, however, using single echo SE and GRE MR sequences, we were unable to distinguish the bacterial signal decay from mammalian signal decay: all curves were monoexponential. Within our mixed samples we found that total transverse relaxivity was extremely high, with  $R2^*$  values of bacterial/mammalian cell mixtures similar to the  $R2^*$  of *L. crispatus*/gelatin (170  $\text{s}^{-1}$  vs. 180  $\text{s}^{-1}$  respectively in 1/2 dilutions). However,  $R2$  was greatly attenuated by the addition of bladder cells compared to the gelatin/PBS background (73.2  $\text{s}^{-1}$  vs. 161  $\text{s}^{-1}$  respectively) which is easily visualized by the change in slope of the line of best fit demonstrating the relationship between transverse relaxivity and fraction of *L. crispatus* cells. Comparison of  $R2/R2^*$  ratio in *L. crispatus*/gelatin versus *L. crispatus*/bladder samples (0.89 and 0.43 respectively for 1/2 *L. crispatus* dilutions) can also demonstrate the  $R2$  attenuation by bladder cells. Although the  $R2^*$  signal remained similar, the  $R2$  signal attenuation led to a significant increase in  $R2'$  potentially related to differences in water diffusion in gelatin compared to bladder cells. Further examination of the effects of mixed cultures is warranted as well as viability assessments for the bladder cells to determine whether the cells are intact and viable.

Finally, we used *S. aureus* USA300 and related siderophore and ferritin mutants to model how iron storage contributes to MR relaxivity in bacteria. However, in this species we detected no changes in MR measures despite changes in the availability of extracellular iron and key iron handling proteins. Due to low sample size, we are unable to confirm changes in iron content, though the invariant MR measures suggest the potential decrease in iron content may be insignificant for MR purposes. There are redundancies in iron import and storage pathways that work to maintain iron homeostasis in *S. aureus* including the *isd*, *feo*, *sir*, *sst*, and *fhu* systems<sup>47</sup>, though staphyloferrin A and B are the major siderophores present in this species<sup>26, 48, 49</sup>. This redundancy promotes survival by ensuring that bacteria get the iron required for growth in iron-replete or iron-deplete conditions. Ferritin A is the main iron storage protein of *Staphylococci* but the Dps homologue *mrgA* also encodes another iron storage protein, though MrgA in *S. aureus* is suspected of playing a larger role in DNA binding as opposed to iron storage<sup>50, 51</sup>. Nonetheless, this alternative iron storage protein may compensate for the iron storage needs of an  $\Delta sfa/\Delta sbn/\Delta ftnA$  mutant. Redundancies in iron handling genes as well as the lethality of iron starvation provide a barrier to understanding how iron storage contributes to transverse relaxivity in bacteria.

### **3.5 Conclusions**

We assessed 12 distinct bacterial isolates and found that MR relaxation rates in all species may be influenced by total cellular iron and manganese contents, among other factors. Each bacterium has a unique and replicable MR signature which we suggest is a property of the bacteria due to their intrinsic metal handling capabilities. Using bacteria with extremely high transverse relaxivity at various dilution factors, we were able to relate MR measures to the quantity of live bacterial cells *in vitro*. Though we were unable to separate distinct transverse relaxivities of bacterial and mammalian cells within a mixed sample, bacterial R2 relaxivity was attenuated by the addition of bladder cells. Due to redundancies in both iron acquisition and storage in *S. aureus*, it is difficult to assess how the form of iron can influence MR relaxivity. Our findings suggest that detection of bacteria using MRI is feasible, especially for imaging lactobacilli with high MR relaxivity. Future applications involving *in vivo* bacterial cell detection

and potentially tracking within the human host will depend on the possible additive or attenuating effects of mixed cultures and the potential for differentiating individual MR signatures within these complex cultures.

### **3.6 References**

- [1] Gao Y.-D., Zhao Y., and Huang J. (2014) Metabolic modeling of common *Escherichia coli* strains in human gut microbiome, *BioMed Res Int* 2014, Article ID 694967.
- [2] McDonald J. A. K., Schroete K., Fuentes S., Heikamp-deJong I., Khursigara C. M., de Vos W. M., and Allen-Vercoe E. (2013) Evaluation of microbial community reproducibility, stability and composition in a human distal gut chemostat model, *J Microbiol Methods* 95, 167–174.
- [3] Yan W., Sun C., Zheng J., Wen C., Ji C., Zhang D., Chen Y., Hou Z., and Yang N. (2019) Efficacy of fecal sampling as a gut proxy in the study of chicken gut microbiota, *Front Microbiol* 10, article 2126.
- [4] Stearns J. C., Lynch M. D., Senadheera D. B., Tenenbaum H. C., Goldberg M. B., Cvitkovitch D. G., Croitoru K., Moreno-Hagelsieb G., and Neufeld J. D. (2011) Bacterial biogeography of the human digestive tract, *Sci Rep* 1, 170.
- [5] Welch J. L. M., Hasegawaa Y., McNulty N. P., Gordon J. I., and Borisy G. G. (2017) Spatial organization of a model 15-member human gut microbiota established in gnotobiotic mice, *PNAS*, E9105–E9114.
- [6] Boursi B., Werner T. J., Gholami S., Houshmand S., Mamtani R., Lewis J. D., Wu G. D., Alavi A., and Yang Y-X. (2018) Functional imaging of the interaction between gut microbiota and the human host: A proof of-concept clinical study evaluating novel use for <sup>18</sup>F-FDG PET-CT, *PLoS ONE* 13(2): e0192747.

- [7] Bourdeau R. W., Lee-Gosselin A., Lakshmanan A., Farhadi A., Kumar S. R., Nety S. P., and Shapiro M. G. (2018) Acoustic reporter genes for noninvasive imaging of microorganisms in mammalian hosts, *Nat Lett* 553, 86-90.
- [8] Hoerr V., Tuchscher L., Huve J., Nippe N., Loser K., Glyvuk N., Tsytsyura Y., Holtkamp M., Sunderkotter C., Karst U., Klingauf J., Peters G., Loffler B., and Faber C. (2013) Bacteria tracking by *in vivo* magnetic resonance imaging, *BMC biology* 11, 63.
- [9] Hill P. J., Stritzker J., Scadeng M., Geissinger U., Haddad D., Basse-Lusebrink T. C., Gbureck U., Jakob P., and Szalay A. A. (2011) Magnetic resonance imaging of tumors colonized with bacterial ferritin-expressing *Escherichia coli*, *PLoS ONE* 6(10): e25409.
- [10] Andronesi O. C., Mintzopoulos D., Righi V., Psychogios N., Kesarwani M., He J., Yasuhara S., Dai G., Rahme L. G., and Tzika A. A. (2010) Combined off-resonance imaging and T2 relaxation in the rotating frame for positive contrast MR imaging of infection in a murine burn model, *J Magn res Imaging* 32, 1172-1183.
- [11] Brandt C. T., Simonsen H., Liptrot M., Sogaard L. V., Lundgren J. D., Ostergaard C., Fridodt-Moller N., and Rowland I. J. (2008) *In vivo* study of experimental pneumococcal meningitis using magnetic resonance imaging, *BMC Med Imaging* 8(1), doi:10.1186/1471-2342-8-.
- [12] Does M. D., and Gore J. C. (2002) Compartmental study of T1 and T2 in rat brain and trigeminal nerve *in vivo*, *Magn Reson Med* 47, 274–283.
- [13] Moran G. R., and Prato F. S. (2001) Modeling tissue contrast agent concentration: a solution to the tissue homogeneity model using a simulated arterial input function, *Magn Reson Med* 45, 42-45.
- [14] Moran G. R., and Prato F. S. (2004) Modeling <sup>1</sup>H exchange: an estimate of the error introduced in MRI by assuming the fast exchange limit in bolus tracking, *Magn Reson Med* 51, 816-827.
- [15] Istratov A. A., and Vyvenko O. F. (1999) Exponential analysis in physical phenomena, *Rev Sci Instrum* 70, 1233-1257.
- [16] Daisley B. A., Monachese M., Trinder M., Bisanz J. E., Chmiel J. A., Burton J. P., and Reid G. (2018) Immobilization of cadmium and lead by *Lactobacillus rhamnosus* GR-1

- mitigates apical-to-basolateral heavy metal translocation in a Caco-2 model of the intestinal epithelium, *Gut microbes*, doi:10.1080/19490976.2018.1526581.
- [17] Haley K. P., and Skaar E. P. (2012) A battle for iron: host sequestration and *Staphylococcus aureus* acquisition, *Microbes Infect* 14, 217-227.
- [18] Ma L., Terwilliger A., and Maresso A. W. (2015) Iron and zinc exploitation during bacterial pathogenesis, *Metallomics* 15, 1541-1554.
- [19] Gao Q., Wang X., Xu H., Xu Y., Ling J., Zhang D., Gao S. and Liu X. (2012) Roles of iron acquisition systems in virulence of extraintestinal pathogenic *Escherichia coli*: salmochelin and aerobactin contribute more to virulence than heme in a chicken infection model, *BMC microbiol* 12, 143-154.
- [20] Skaar E. P., and Raffatellu M. (2015) Metals in infectious diseases and nutritional immunity, *Metallomics* 7, 926-928.
- [21] Abdul-Tehrani H., Hudson A. J., Chang Y.-S., Timms A. R., Hawkins C., Williams J. M., Harrison P. M., Guest J. R., and Andrews S. C. (1999) Ferritin mutants of *Escherichia coli* are iron deficient and growth impaired, and fur mutants are iron deficient, *J Bacteriol* 181, 1415-1428.
- [22] Uebe R., Voigt B., Schweder T., Albrecht D., Katzmann E., Lang C., Bottger L., Matzanke B., and Schuler D. (2010) Deletion of a fur-Like gene affects iron homeostasis and magnetosome formation in *Magnetospirillum gryphiswaldense*, *J Bacteriol* 192, 4192–4204.
- [23] Subashchandrabose S., and Mobley H. L. T. (2015) Virulence and fitness determinants of uropathogenic *Escherichia coli*, *Microbiol Spectr* 3(4).
- [24] Ikeda J. S., Janakiraman A., Kehres D. G., Maguire M. E., and Slauch J. M. (2005) Transcriptional regulation of sitABCD of *Salmonella enterica* serovar *Typhimurium* by MntR and Fur, *J Bacteriol* 187, 912-922.
- [25] Beasley F. C., and Heinrichs D. E. (2010) Siderophore-mediated iron acquisition in the staphylococci, *Journal of inorganic biochemistry* 104, 282-288.



- [26] Beasley F. C., Vinés E., Grigg J. C., Zheng Q., Liu S., Lajoie G. A., Murphy M. E. P., and Heinrichs D. E. (2009) Characterization of staphyloferrin A biosynthetic and transport mutants in *Staphylococcus aureus*, *Mol Microbiol* 72, 947-963.
- [27] Archibald F. (1983) *Lactobacillus plantarum*, an organism not requiring iron *FEMS Microbiol Lett* 19, 29-32.
- [28] Archibald F. S., and Duong M. N. (1984) Manganese acquisition by *Lactobacillus plantarum*, *J Bacteriol* 158, 1-8.
- [29] Hao Z., Reiske H. R., and Wilson D. B. (1999) Characterization of cadmium uptake in *Lactobacillus plantarum* and isolation of cadmium and manganese uptake mutants, *Appl Environ Microbiol* 65, 4741-4745.
- [30] Groot M. N., Klaassens E., de Vos W. M., Delcour J., Hols P., and Kleerebezem M. (2005) Genome-based in silico detection of putative manganese transport systems in *Lactobacillus plantarum* and their genetic analysis, *Microbiology* 151, 1229-1238.
- [31] Archibald F. (1986) Manganese: Its acquisition by and function in the lactic acid bacteria, *CRC Critical Reviews in Microbiology* 13, 63-109.
- [32] Sengupta A., Quiaoit K., Thompson R., Prato F., Gelman N., and Goldhawk D. (2014) Biophysical features of MagA expression in mammalian cells: implications for MRI contrast, *Front Microbiol* 5, article 29.
- [33] Smith P. K., Krohn R., Hermanson G. T., Mallia A. K., Gartner F. H., Provenzano M. D., Fujimoto E. K., Goeke N. M., Olson B. J., and Klenk D. C. (1985) Measurement of protein using bicinchoninic acid, *Anal Biochem* 150, 76-85.
- [34] Liu L., Alizadeh K., Donnelly S. C., Dassanayake P., Hou T. T., McGirr R., Thompson R. T., Prato F. S., Gelman N., Hoffman L., and Goldhawk D. E. (2019) MagA expression attenuates iron export activity in undifferentiated multipotent P19 cells, *PLoS ONE* 14(6): e0217842.
- [35] Gossuin Y., Muller R. N., and Gillis P. (2004) Relaxation induced by ferritin: a better understanding for an improved MRI iron quantification, *NMR biomed* 17, 427-432.
- [36] Bydder G. (2010) Imaging of short and ultrashort T2 and T2\* tissues using clinical MRI systems, *Imag Med* 2, 225-233.

- [37] Imbert M., and Blondeau R. (1998) On the iron requirement of lactobacilli grown in chemically defined medium, *Curr Microbiol* 37, 64-66.
- [38] Santiago G. L., Cools P., Verstraelen H., Trog M., Missine G., El Aila N., Verhelst R., Tency I., Claeys G., Temmerman M., and Vanechoutte M. (2011) Longitudinal study of the dynamics of vaginal microflora during two consecutive menstrual cycles, *PLoS ONE* 6(11): e28180.
- [39] Srinivasan S., Liu C., Mitchell C. M., Fiedler T. L., Thomas K. K., Agnew K. J., Marrazzo J. M., and Fredricks D. N. (2010) Temporal variability of human vaginal bacteria and relationship with bacterial vaginosis, *PLoS ONE* 5, e10197.
- [40] Sobota J. M., and Imlay J. A. (2011) Iron enzyme ribulose-5-phosphate 3-epimerase in *Escherichia coli* is rapidly damaged by hydrogen peroxide but can be protected by manganese, *PNAS* 108, 5402-5407.
- [41] Keyer K., and Imlay J. A. (1996) Superoxide accelerates DNA damage by elevating free-iron levels, *PNAS* 93, 13635-13640.
- [42] Martin J. E., Waters L. S., Storz G., and Imlay J. A. (2015) The *Escherichia coli* small protein MntS and exporter MntP optimize the intracellular concentration of manganese, *PLoS Genet* 11, e1004977.
- [43] Hanks T. S., Liu M., McClure M. J., Fukumura M., Duffy A., and Lei B. (2006) Differential regulation of iron- and manganese-specific MtsABC and heme-specific HtsABC transporters by the metalloregulator MtsR of group A *Streptococcus*, *Infection and immunity* 74, 5132-5139.
- [44] Rodionov D. A., Hebbeln P., Gelfand M. S., and Eitinger T. (2006) Comparative and functional genomic analysis of prokaryotic nickel and cobalt uptake transporters: evidence for a novel group of ATP-binding cassette transporters, *J Bacteriol* 188, 317-327.
- [45] Ferrières L., Hancock V., and Klemm P. (2007) Specific selection for virulent urinary tract infectious *Escherichia coli* strains during catheter-associated biofilm formation, *FEMS Immunol Med Microbiol* 51, 212-219.

- [46] Huttenhower C., *et al.* (2012) Structure, function and diversity of the healthy human microbiome, *Nat* 486, 207-214.
- [47] Madsen J. L., Johnstone T. C., and Nolan E. M. (2015) Chemical synthesis of Staphyloferrin B affords insight into the molecular structure, iron chelation, and biological activity of a polycarboxylate siderophore deployed by the human pathogen *Staphylococcus aureus*, *J Am Chem Soc* 137, 9117-9127.
- [48] Cheung J., Beasley F. C., Liu S., Lajoie G. A., and Heinrichs D. E. (2009) Molecular characterization of staphyloferrin B biosynthesis in *Staphylococcus aureus*, *Mol Microbiol* 74, 594-608.
- [49] Hammer N. D., and Skaar E. P. (2011) Molecular mechanisms of *Staphylococcus aureus* iron acquisition, *Annu Rev Microbiol* 65, 129-147.
- [50] Chiancone E., and Ceci P. (2010) The multifaceted capacity of Dps proteins to combat bacterial stress conditions: Detoxification of iron and hydrogen peroxide and DNA binding, *Biochem Biophys Acta* 1800, 798–805.
- [51] Morrissey J. A., Cockayne A., Brummell K., and Williams P. (2004) The staphylococcal ferritins are differentially regulated in response to iron and manganese and via PerR and Fur, *Infect Immun* 72, 972-979.

## **Chapter 4: Summary**

### **4.1 Summary**

In this study we examined the MR relaxation rates of bacteria that may be encountered in the human urogenital or gut microbiome. Most, if not all bacteria we imaged displayed high transverse relaxivity, much higher than that of mammalian cell lines examined using the same MR sequences<sup>1-3</sup>. This transverse relaxivity was dominated by R2, with little to no R2' contribution. These findings may be associated with the form of metals within the cell. It has been previously found that 99% of all intracellular iron in *E. coli* is stored in protein aggregates to limit DNA and cellular damage<sup>4,5</sup>.

There was little to no variation in longitudinal relaxivity between bacterial strains or species, likely due to low basal R1 values. Though the MR measures did not distinguish between commensal or pathogenic bacterial groups, bacterial strains exhibited differences in transverse relaxivity.

We found that MR measures for *L. crispatus* are proportional to the number of live cells within the imaged sample (Figure 19). In addition, MR measures varied between strains of *E. coli* and between various species of bacteria in part due to differential metal handling, with MR relaxivities of *Lactobacillus* spp. dominating. Overall, there was little variability in iron content, but large variability in manganese content between bacterial species. The commensal and probiotic lactobacilli were characterized by extremely high manganese content which may explain the high transverse relaxivity despite undetectable levels of iron. Potentially, bacterial size and morphology as well as the presence of other MR sensitive elements may contribute to MR relaxivity.

Since iron content is positively correlated to transverse relaxation rates in iron-supplemented MagA-expressing mammalian cells<sup>1,2,6</sup>, we assessed the impact of MagA expression in *E. coli* on MR relaxivity. MagA-expressing cells displayed iron-associated cytotoxicity. Since iron is

tightly regulated in *E. coli* to prevent toxicity<sup>4</sup>, future MagA expression studies may need to introduce tighter regulatory systems involving repressors of transcription. While MagA expression offered no advantage in our laboratory model, the inherently high R2 of untransformed *E. coli* strains among other bacteria suggests that contrast enhancement may be unnecessary for visualizing bacteria by MRI when they are present in sufficient quantities. For *L. crispatus* ATCC33820, potentially as few as  $\sim 26 \times 10^6$  CFUs per mm<sup>3</sup> may be visible by MRI at clinical field strength. The linear correlation between MR transverse relaxation rates and number of *L. crispatus* ATCC33820 CFUs demonstrates the potential to estimate number of live bacteria within a region of interest for future *in vivo* imaging applications.

High bacterial transverse relaxivity may be useful in differentiating the MR signal of bacteria from human tissue and provides a potentially important foundation for future studies using *in vivo* MRI to detect bacteria and observe their interactions. *In vivo*, pure single-strain bacterial niches are not expected, and MR regions of interest may contain both bacterial and mammalian cells. Therefore, we assessed how MR relaxivity changes in response to bacterial/mammalian mixtures compared to single strain cultures. Using our MR sequences, we were unable to distinguish bacterial signal decay from the mammalian bladder cell signal based on the monoexponential fit of the decay curve. Nonetheless, R2 was greatly attenuated by the addition of bladder cells compared to a pure bacterial sample, leading to a significant increase in R2' when bacteria were mixed with mammalian cells as well as lower R2/R2\* ratios. This change in R2\* composition may allow us to identify prokaryotic/eukaryotic interfaces *in vivo* from luminal regions of interest containing predominantly bacteria.

Finally, MR relaxivity was unchanged by iron availability in *S. aureus* USA300 and related siderophore and ferritin mutants, while potential changes in iron content must be assessed further. Though staphyloferrin A and B are the key siderophores present in *S. aureus*<sup>7-9</sup> with ferritin as the main iron storage protein, there are alternative pathways for these bacteria to import and store iron. Redundancies in iron handling genes as well as the lethality of iron starvation provide a barrier to understanding how iron storage contributes to transverse relaxivity in bacteria.

## **4.2 Future Directions**

Although bacteria exhibit high transverse relaxivity, it would still be useful to explore alternative forms of MR contrast enhancement aside from MagA to improve detection, enable reporter gene expression of molecular activity, and increase the sensitivity of our imaging technique. Multi-modality imaging will likely be important for accurate bacterial detection and tracking *in vivo*. This could be achieved by externally labeling bacteria of interest with radioisotopes for simultaneous positron emission tomography (PET)/MR imaging (Biomedical Imaging of Bacteria and Viruses worldwide patent L-21-002). Ultrasound probes, such as those developed in previous bacterial studies<sup>10</sup>, also provide promising candidates for multi-modality imaging applications. Nonetheless, the high spatial resolution and high sensitivity provided by current MRI systems make it an ideal modality to pursue. With future technological advancements we expect to see more powerful MRI systems with higher sensitivity, better resolution, as well as new pulse sequences that improve signal-to-noise ratios and signal acquisition times. Although cost is currently a major barrier in the widespread implementation of MRI (among other modalities), as imaging becomes the standard of care costs will likely decrease and allow for greater accessibility and promote even more interdisciplinary applications of imaging. The utility of the sequences we employed to assess bacterial MR relaxation rates must also be assessed in future studies. As mentioned in sections 2.4 and 3.4, flip angle errors in these sequences or inconsistent application of echo-spacing may have led to inaccuracies in R2 and R2\* measurements that make it difficult to compare these values directly. In some cases, we found R2 values appeared greater than R2\*, which we know cannot be the case. We propose comparing the R2\* values obtained from the multi-echo GRE sequence used to a single-echo GRE sequence in a future cell phantom experiment to demonstrate the measurement variation. In future studies we may also explore ultrashort echo time (UTE) sequences to improve transverse relaxivity measurements for bacteria.

To further corroborate our findings of intrastain MR variability, we would like to examine other *L. crispatus* strains, especially strains like *L. crispatus* 20 which lacks the MtsA metal transport gene. Could MtsA protein be responsible for large quantities of Mn uptake, thus promoting unique MR signatures of lactobacilli? Since high manganese content may be associated with high MR signal for many lactobacilli, it would also be interesting to culture these bacteria in

varying manganese titers, including saturation of Mn uptake to assess whether further manganese loading might improve the detection limit of lactobacilli by MRI. This could be achieved by growing the lactobacilli in a Mn deplete medium and adding Mn back as previous studies have shown: intracellular Mn should be proportional to Mn supplementation up to  $150 \mu\text{M}$ <sup>11</sup>. We note that the deMan, Rogosa and Sharpe (MRS) medium we used in the present study contains more than double that concentration of manganese, with  $330 \mu\text{M}$  Mn<sup>12</sup>. Perhaps Mn supplementation could be used to selectively enhance the MR relaxivity of lactobacilli, permitting specific detection of these commensal bacteria through their Mn uptake abilities which far supersede that of other bacterial species examined in this thesis.

Further evaluation of mixed prokaryotic/eukaryotic samples is necessary. It would be interesting to assess whether transverse relaxivity in mixtures of 5637 bladder cells and *L. crispatus* ATCC33820 could be accurately measured using larger fractions of bacterial cells (60-90%). Even if R2\* measurements were not possible due to rapid signal decay, a measurable decrease in R2 might still be obtained in the presence of fewer mammalian cells (10-40%). This would be important for understanding MRI in microbiotas of lower bacterial diversity, for example those with largely lactobacilli like the vagina or the bladder<sup>13, 14</sup>. How MR relaxation rates change in response to diseases like bacterial vaginosis or UTI is currently unknown. It is crucial to assess complex bacterial cultures *in vitro*, potentially those from fecal or chemostat samples, to understand the implications of *in vivo* bacterial detection and the limitations that may be encountered.

### **4.3 References**

- [1] Sengupta A., Quiaoit K., Thompson R., Prato F., Gelman N., and Goldhawk D. (2014) Biophysical features of MagA expression in mammalian cells: implications for MRI contrast, *Frontiers in Microbiology* 5, article 29.
- [2] Liu L., Alizadeh K., Donnelly S. C., Dassanayake P., Hou T. T., McGirr R., Thompson R. T., Prato F. S., Gelman N., Hoffman L., and Goldhawk D. E. (2019) MagA expression

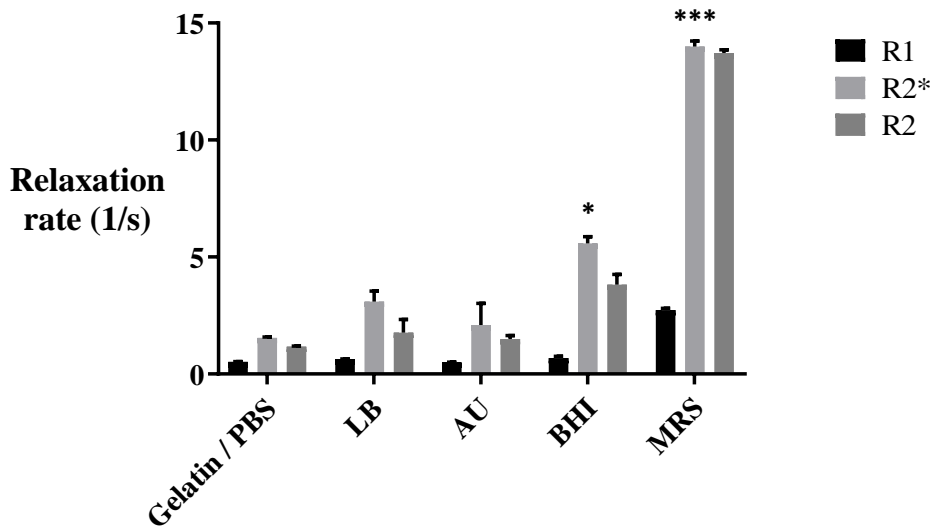
attenuates iron export activity in undifferentiated multipotent P19 cells, *PLoS ONE* 14(6): e0217842

- [3] Quiaoit K. (2015) Towards the development of a MagA reporter gene expression construct for magnetic resonance imaging, *Western University, London, Canada, Scholarship@Western Electronic Thesis and Dissertation Repository*.
- [4] Abdul-Tehrani H., Hudson A. J., Chang Y.-S., Timms A. R., Hawkins C., Williams J. M., Harrison P. M., Guest J. R., Andrews S. C. (1999) Ferritin mutants of *Escherichia coli* are iron deficient and growth impaired, and fur mutants are iron deficient, *J Bacteriol* 181, 1415-1428.
- [5] Bauminger E. R., Cohen S. G., Dickson D. P. E., Levy A., Ofer S., and Yariv J. (1980) Mossbauer spectroscopy of *Escherichia coli* and its iron-storage protein, *Biochim Biophys Acta* 623, 237-242.
- [6] Goldhawk D., Gelman N., Sengupta A., and Prato F. (2015) The interface between iron metabolism and gene-based iron contrast for MRI, *Magn Reson Insights* 8, 9-14.
- [7] Madsen J. L., Johnstone T. C., and Nolan E. M. (2015) Chemical synthesis of Staphyloferrin B affords insight into the molecular structure, iron chelation, and biological activity of a polycarboxylate siderophore deployed by the human pathogen *Staphylococcus aureus*, *J Am Chem Soc* 137, 9117-9127.
- [8] Cheung J., Beasley F. C., Liu S., Lajoie G. A., and Heinrichs D. E. (2009) Molecular characterization of staphyloferrin B biosynthesis in *Staphylococcus aureus*, *Mol Microbiol* 74, 594-608.
- [9] Beasley F. C., Vinés E., Grigg J. C., Zheng Q., Liu S., Lajoie G. A., Murphy M. E. P., and Heinrichs D. E. (2009) Characterization of staphyloferrin A biosynthetic and transport mutants in *Staphylococcus aureus*, *Mol Microbiol* 72, 947-963
- [10] Bourdeau R. W., Lee-Gosselin A., Lakshmanan A., Farhadi A., Kumar S. R., Nety S. P. and Shapiro M. G. (2018) Acoustic reporter genes for noninvasive imaging of microorganisms in mammalian hosts, *Nat Lett* 553, 86-90.



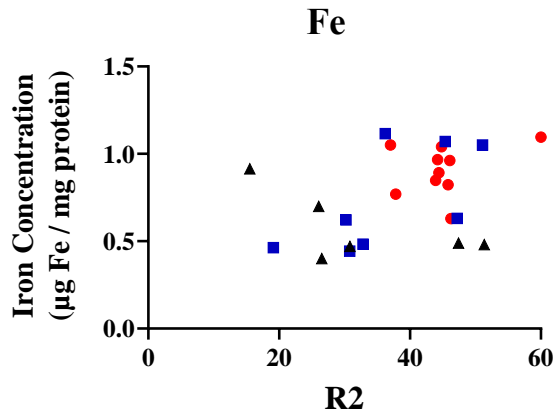
- [11] Archibald F. S., and Duong M. N. (1984) Manganese acquisition by *Lactobacillus plantarum*, *J Bacteriol* 158, 1-8.
- [12] Archibald F. (1986) Manganese: Its acquisition by and function in the lactic acid bacteria, *CRC Critical Reviews in Microbiology* 13, 63-109.
- [13] Thomas-White K., Forster S. C., Kumar N., Van Kuiken M., Putonti C., Stares M. D., Hilt E. E., Price T. K., Wolfe A. J., and Lawley T. D. (2018) Culturing of female bladder bacteria reveals an interconnected urogenital microbiota, *Nat Commun* 9, DOI: 10.1038/s41467-018-03968-5.
- [14] Komesu Y. M., Dinwiddie D. L., Richter H. E., Lukacz E. S., Sung V. W., Siddiqui N. Y., Zyczynski H. M., Ridgeway B., Rogers R. G., Arya L. A., Mazloomdoost D., Levy J., Carper B., and Gantz M. G. (2020) Defining the relationship between vaginal and urinary microbiomes, *Am J Obstet Gynecol* 222, e1-10.

## Appendices

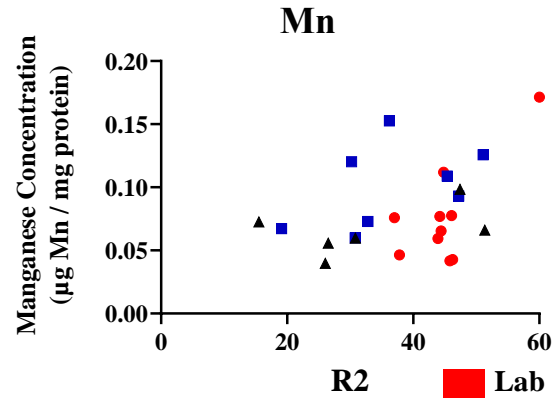


**Appendix 1. Impact of bacterial growth media on MR measures.** The bar graph compares longitudinal (R1) and transverse (R2\*, R2) relaxation rates +/- SEM of various growth media mounted in a gelatin phantom and scanned at 3T. Bacteria were excluded from each broth: LB, lysogeny broth; AU, artificial urine; BHI, brain-heart infusion; and MRS, deMan, Rogosa, Sharpe. While the signals from LB and AU are comparable to gelatin/PBS, BHI and MRS significantly increased relaxation rates (n = 3 – 4, except n = 2 for AU; \* p < 0.05, \*\*\* p < 0.001).

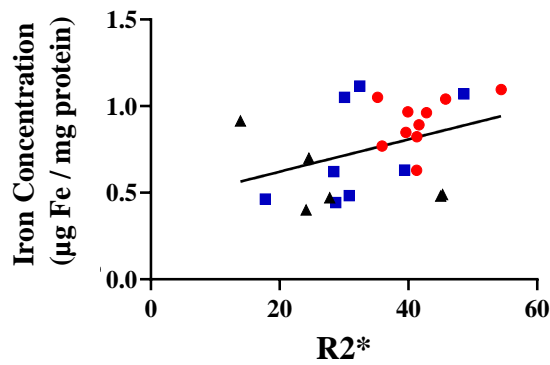
A



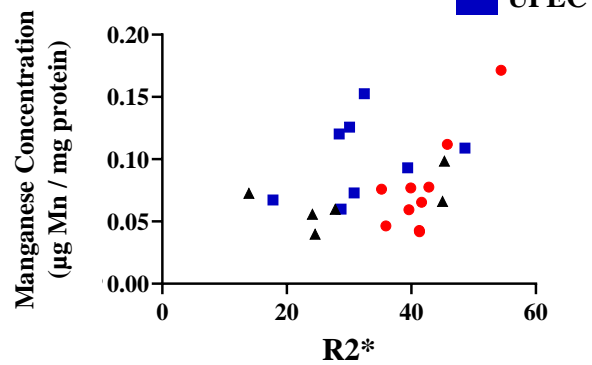
B



C

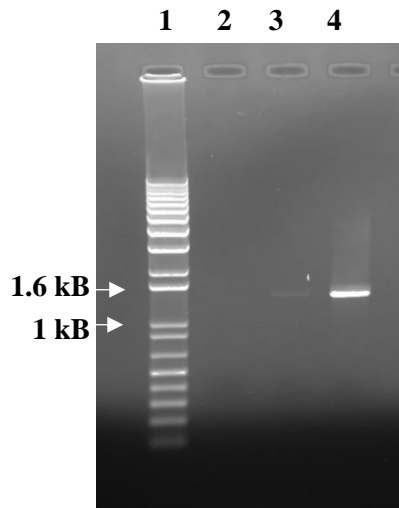


D



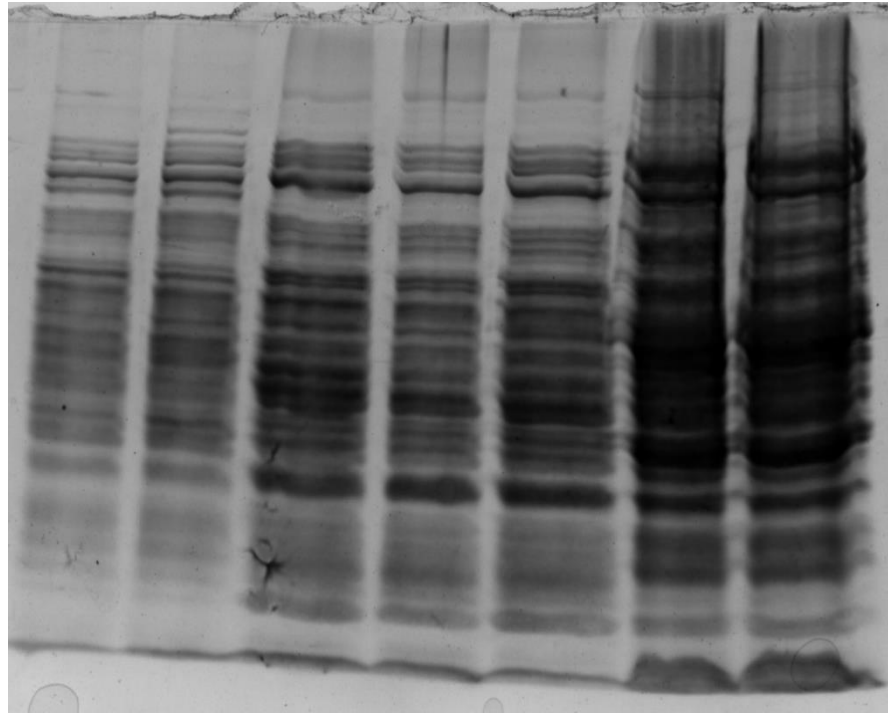
## Appendix 2. Total cellular iron and manganese do not reliably predict transverse

**relaxivity.** Elemental iron and manganese content of various *E. coli* strains was measured by ICP-MS and related to matched MR relaxation rates. Based on Spearman's test, iron (A) and manganese (B) do not correlate to R2 measurements. Iron (C) has a weak positive correlation to R2\* measurements ( $r^2 = 0.141$  respectively,  $p < 0.05$ ) while manganese (D) does not correlate to R2\* measurements. No correlations exist within individual classification groups.



**Appendix 3. Amplified *HA-magA-myc*.** The insert *HA-magA-myc* DNA was amplified from pcDNA3.1*MycHisA*<sup>+</sup>/*HA-magA* by PCR using a 56 °C annealing temperature and 30 cycles. Primers are listed in Table 3. Lane 1 contains a 1 Kb DNA ladder. Lane 2 contains a Taq polymerase negative control with no *HA-magA-myc* amplification. Lanes 3 and 4 contain amplified *HA-magA-myc* (1467 bp) using either 1 or 10 ng/ $\mu$ L template, respectively. The conditions in lane 4 were chosen for all subsequent PCR amplifications.

	<u>Untransformed</u>		<u>Vector</u>	<u>MagA</u>			
<b>IPTG</b>	-	+	-	-	-	+	+
<b>Fe</b>	-	-	-	-	+	-	+



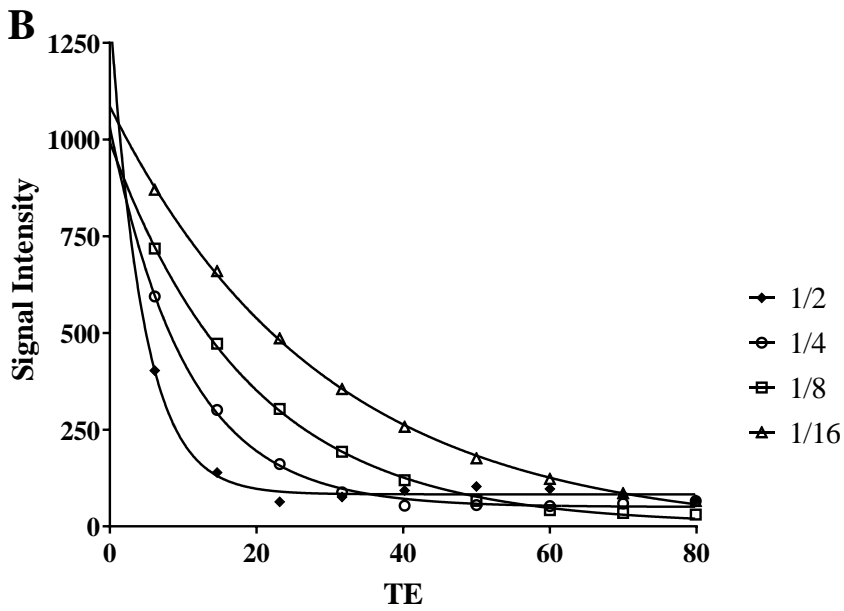
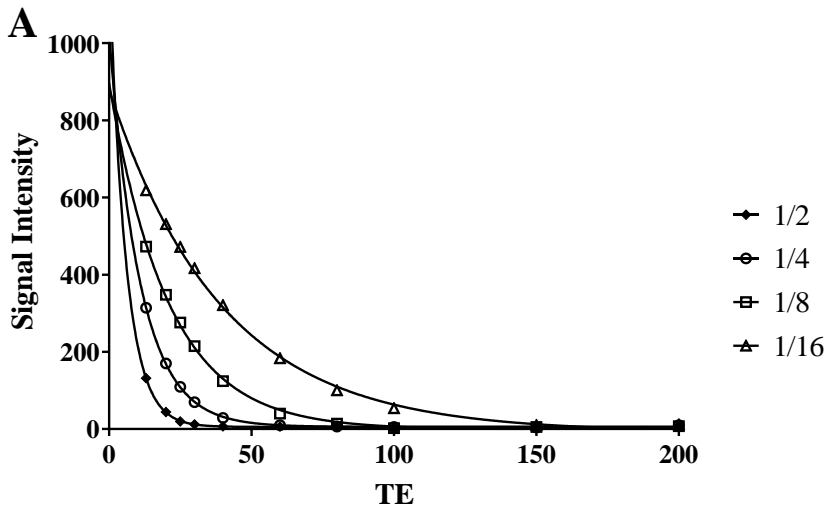
**Appendix 4. Qualitative differential protein expression following induction of MagA expression in *E. coli* BL21(DE3).** Total protein was isolated from bacterial cells untransformed (lanes 1–2), transformed with pET28a<sup>+</sup> (lane 3) or pET28a<sup>+</sup>/*HA-magA-myc* (lanes 4–7). Samples were separated on a denaturing gel under reducing conditions and stained with Coomassie Blue. Coomassie staining was not sensitive enough to detect protein from molecular weight standards for estimating protein masses. Untransformed cells (lanes 1–2) are compared to those transformed with either the empty vector (lane 3) or the hybrid construct (lanes 4–7). After induction of MagA-transformed cells with IPTG, Coomassie-stained protein increases relative to both uninduced and untransformed cells; however, treatment with an extracellular iron supplement did not drastically alter protein expression. The estimated MW of HA-MagA-Myc is ~54 kDa.

**Appendix 5. Longitudinal relaxation rates for MagA expressing *E. coli* BL21(DE3)**

<b>Sample</b>	<b>R1 (s<sup>-1</sup>)<sup>a</sup></b>	<b>SEM (s<sup>-1</sup>)</b>	<b>n-value</b>
<b>BL21(DE3)</b>	1.70 a	0.06	5
<b>BL21(DE3)/pET28a<sup>+</sup></b>	1.68 a	0.00	3
<b>BL21(DE3)/magA + Fe</b>	1.92 b	0.04	3
<b>BL21(DE3)/magA + IPTG</b>	1.33 c	0.02	3
<b>BL21(DE3)/magA + Fe + IPTG</b>	1.33 c	0.04	3

<sup>a</sup> Letters designate statistically significant differences in R1 values between transformed *E. coli* strains where values followed by the same letter are not significantly different based on a one-way ANOVA and Tukey's test.

R1 of untransformed BL21(DE3) is significantly higher than that of vector-transformed, or induced magA-transformed BL21(DE3) +/- Fe ( $p < 0.001$ ). Induced MagA-transformed bacteria have lower longitudinal relaxivity than empty vector or uninduced MagA-transformed *E. coli* ( $p < 0.05$ ).



**Appendix 6. Representative transverse relaxation decay curves for *L. crispatus* ATCC33820 diluted in gelatin.** Signal intensity was plotted against echo time (TE) to obtain R2 (A) and R2\* (B) decay curves for *L. crispatus* serially diluted 1/2 in gelatin.

**Appendix 7. Transverse and longitudinal relaxation rates for washed or unwashed *E. coli* BL21(DE3)**

<b>R2 Relaxation Rate (s<sup>-1</sup>)</b>						<b>Mean</b>	<b>SD</b>	<b>SEM</b>
BL21(DE3) / LB	45.82	37.82	43.93	44.43	44.81	43.36	3.17	1.42
BL21(DE3) / PBS	46.25	37.01	46.08	44.23	-	43.39	4.35	2.18
Gelatin / LB	0.55	1.09	2.74	2.71	-	1.77	1.12	0.56
Gelatin / PBS	1.19	1.21	1.10	1.17	-	1.17	0.05	0.02

<b>R2* Relaxation Rate (s<sup>-1</sup>)</b>						<b>Mean</b>	<b>SD</b>	<b>SEM</b>
BL21(DE3) / LB	41.32	35.92	39.63	41.66	45.77	40.86	3.57	1.59
BL21(DE3) / PBS	41.29	35.21	42.81	39.91	-	39.80	3.28	1.64
Gelatin / LB	2.71	2.43	4.39	2.87	-	3.10	0.88	0.44
Gelatin / PBS	1.54	1.52	1.63	1.50	-	1.55	0.06	0.03

<b>R1 Relaxation Rate (s<sup>-1</sup>)</b>						<b>Mean</b>	<b>SD</b>	<b>SEM</b>
BL21(DE3) / LB	1.55	1.58	1.85	1.78	1.75	1.70	0.13	0.06
BL21(DE3) / PBS	1.66	1.52	2.11	1.94	-	1.77	0.27	0.13
Gelatin / LB	0.62	0.62	0.65	0.64	-	0.63	0.02	0.01
Gelatin / PBS	0.51	0.51	0.53	0.53	-	0.52	0.01	0.01



**Appendix 8. Transverse and longitudinal relaxation rates of *E. coli* strains**

<b>R2 Relaxation Rate (s<sup>-1</sup>)</b>						<b>Mean</b>	<b>SD</b>	<b>SEM</b>
BL21(DE3)	45.82	37.82	43.93	44.43	44.81	43.36	3.17	1.42
MG1655	51.34	51.88	47.41	-	-	50.21	2.44	1.41
Nissle	26.52	28.91	30.83	-	-	28.75	2.16	1.25
25922	15.50	25.96	26.05	-	-	22.50	6.07	3.50
67	30.20	39.58	36.23	-	-	35.34	4.75	2.74
AD110	30.77	25.18	19.11	-	-	25.02	5.83	3.37
GR-12	32.83	46.33	47.21	-	-	42.12	8.06	4.65
536	51.08	31.88	33.14	-	-	38.70	10.74	6.20
J96	45.39	51.35	52.84	-	-	49.86	3.94	2.28

<b>R2* Relaxation Rate (s<sup>-1</sup>)</b>						<b>Mean</b>	<b>SD</b>	<b>SEM</b>
BL21(DE3)	41.32	35.92	39.63	41.66	45.77	40.86	3.57	1.59
MG1655	45.01	47.58	45.53	-	-	46.04	1.36	0.78
Nissle	24.13	29.77	27.77	-	-	27.22	2.86	1.65
25922	13.91	24.18	24.56	-	-	20.88	6.04	3.49
67	28.42	36.15	32.45	-	-	32.34	3.87	2.23
AD110	28.70	22.36	17.78	-	-	22.95	5.48	3.17
GR-12	30.82	41.91	39.41	-	-	37.38	5.82	3.36
536	46.45	30.07	32.37	-	-	36.30	8.87	5.12
J96	38.66	48.61	48.93	-	-	45.40	5.84	3.37

<b>R1 Relaxation Rate (s<sup>-1</sup>)</b>						<b>Mean</b>	<b>SD</b>	<b>SEM</b>
BL21(DE3)	1.55	1.58	1.85	1.78	1.75	1.70	0.13	0.06
MG1655	1.52	1.74	1.72	-	-	1.66	0.12	0.07
Nissle	1.29	1.45	1.53	-	-	1.42	0.12	0.07
25922	1.07	1.31	1.29	-	-	1.22	0.13	0.08
67	1.45	1.76	1.69	-	-	1.63	0.16	0.09
AD110	1.33	1.38	1.22	-	-	1.31	0.08	0.05
GR-12	1.40	1.72	1.91	-	-	1.68	0.26	0.15
536	1.81	1.53	1.57	-	-	1.64	0.15	0.09
J96	1.70	1.99	1.95	-	-	1.88	0.16	0.09

**Appendix 9. ICP-MS iron and manganese content of *E. coli* strains**

Fe content ( $\mu\text{g Fe / mg protein}$ )							Mean	SD	SEM
BL21(DE3)	0.824	0.770	0.848	0.892	1.040	0.561	0.823	0.157	0.064
MG1655	0.480	0.489	0.530	-	-	-	0.500	0.027	0.015
Nissle	0.400	0.471	0.423	0.437	-	-	0.433	0.030	0.015
25922	0.914	0.700	0.807	-	-	-	0.807	0.107	0.062
67	0.622	1.116	0.450	0.628	-	-	0.704	0.287	0.143
AD110	0.443	0.463	0.492	-	-	-	0.466	0.025	0.014
GR-12	0.630	0.483	0.346	-	-	-	0.486	0.142	0.082
536	1.050	0.581	0.507	-	-	-	0.713	0.294	0.170
J96	1.070	0.729	0.671	-	-	-	0.823	0.216	0.124

<b>Mn content (<math>\mu\text{g Mn} / \text{mg protein}</math>)</b>							<b>Mean</b>	<b>SD</b>	<b>SEM</b>
BL21(DE3)	0.042	0.046	0.059	0.065	0.112	0.093	0.070	0.028	0.011
MG1655	0.066	0.098	0.095	-	-	-	0.086	0.018	0.010
Nissle	0.056	0.060	0.072	0.047	-	-	0.059	0.010	0.005
25922	0.073	0.040	0.070	-	-	-	0.061	0.018	0.011
67	0.120	0.153	0.120	0.223	-	-	0.154	0.049	0.024
AD110	0.060	0.067	0.084	-	-	-	0.070	0.012	0.007
GR-12	0.093	0.073	0.071	-	-	-	0.079	0.012	0.007
536	0.126	0.115	0.174	-	-	-	0.138	0.031	0.018
J96	0.109	0.107	0.141	-	-	-	0.119	0.019	0.011

**Appendix 10. Transverse and longitudinal relaxation rates of MagA-expressing *E. coli* BL21(DE3)**

<b>R2 Relaxation Rate (s<sup>-1</sup>)</b>						<b>Mean</b>	<b>SD</b>	<b>SEM</b>
Untransformed	45.82	37.82	43.93	44.43	44.81	43.36	3.17	1.42
Untransformed + Fe	60.00	60.29	50.47	-	-	56.92	5.59	3.23
Vector	33.81	39.75	41.73	-	-	38.43	4.12	2.38
MagA + Fe	41.07	39.91	45.40	-	-	42.13	2.89	1.67
MagA + IPTG	28.38	31.12	30.86	-	-	30.12	1.51	0.87
MagA + Fe + IPTG	30.30	28.73	32.11	-	-	30.38	1.69	0.98

<b>R2* Relaxation Rate (s<sup>-1</sup>)</b>						<b>Mean</b>	<b>SD</b>	<b>SEM</b>
Untransformed	41.32	35.92	39.63	41.66	45.77	40.86	3.57	1.59
Untransformed + Fe	54.40	52.70	43.79	-	-	50.30	5.70	3.29
Vector	33.96	39.38	39.13	-	-	37.49	3.06	1.77
MagA + Fe	38.26	37.61	40.65	-	-	38.84	1.60	0.92
MagA + IPTG	26.85	31.66	32.77	-	-	30.43	3.15	1.82
MagA + Fe + IPTG	27.42	26.83	34.21	-	-	29.49	4.10	2.37

<b>R1 Relaxation Rate (s<sup>-1</sup>)</b>						<b>Mean</b>	<b>SD</b>	<b>SEM</b>
Untransformed	1.55	1.58	1.85	1.78	1.75	1.70	0.13	0.06
Untransformed + Fe	2.06	2.09	2.00	-	-	2.05	0.05	0.03
Vector	1.69	1.68	1.68	-	-	1.68	0.01	0.00
MagA + Fe	1.93	1.85	1.99	-	-	1.92	0.07	0.04
MagA + IPTG	1.3	1.37	1.33	-	-	1.33	0.04	0.02
MagA + Fe + IPTG	1.3	1.41	1.28	-	-	1.33	0.07	0.04

**Appendix 11. ICP-MS iron and manganese content of MagA-expressing *E. coli* BL21(DE3)**

Fe content ( $\mu\text{g Fe} / \text{mg protein}$ )							Mean ^	SD	SEM
Untransformed	0.824	0.770	0.848	0.892	1.040	0.561	0.823	0.157	0.064
Untransformed + Fe	1.096	1.398	0.487	0.543	-	-	0.881	0.441	0.220
Vector	1.457	0.406	0.965	-	-	-	0.943	0.526	0.304
MagA + Fe	1.140	1.163	1.019	-	-	-	1.107	0.077	0.045
MagA + IPTG	0.652	0.734	0.653	-	-	-	0.680	0.047	0.027
MagA + Fe + IPTG	0.891	0.764	-	-	-	-	0.828	-	-

^ Median is displayed for samples where  $n < 3$ .

Mn content ( $\mu\text{g Mn} / \text{mg protein}$ )							Mean	SD	SEM
BL21(DE3)	0.042	0.046	0.059	0.065	0.112	0.093	0.070	0.028	0.011
Untransformed + Fe	0.171	0.088	0.044	0.133	-	-	0.109	0.055	0.028
Vector	0.319	0.108	0.104	-	-	-	0.177	0.123	0.071
MagA + Fe	0.160	0.186	0.148	-	-	-	0.165	0.019	0.011
MagA + IPTG	0.019	0.032	0.027	-	-	-	0.026	0.007	0.004
MagA + Fe + IPTG	0.019	0.019	0.015	-	-	-	0.018	0.002	0.001



**Appendix 12. Transverse and longitudinal relaxation rates of various bacterial species**

<b>R2 Relaxation Rate (s<sup>-1</sup>)</b>					<b>Mean</b>	<b>SD</b>	<b>SEM</b>
<i>P. aeruginosa</i> PA01	33.48	30.63	31.76	-	31.96	1.44	0.83
<i>S. epidermidis</i> ATCC35984	25.84	26.33	29.59	-	27.25	2.04	1.18
<i>K. pneumoniae</i> 280	28.50	31.39	30.22	-	30.04	1.45	0.84
<i>E. faecalis</i> ATCC33186	37.98	32.85	22.82	-	31.22	7.71	4.45
<i>P. mirabilis</i> 296	16.71	16.86	17.51	21.92	18.25	2.47	1.24
<i>S. aureus</i> USA300	31.93	29.70	18.54	-	26.72	7.17	4.14
<i>S. aureus</i> Newman	6.68	15.26	11.12	-	11.02	4.29	2.48
<i>L. gasseri</i> ATCC33323	86.92	89.50	58.05	63.65	74.53	16.00	8.00
<i>L. reuteri</i> RC-14	28.99	29.33	28.28	-	28.87	0.54	0.31
<i>L. rhamnosus</i> GR-1	44.08	48.39	52.69	-	48.39	4.31	2.49

<b>R2* Relaxation Rate (s<sup>-1</sup>)</b>					<b>Mean</b>	<b>SD</b>	<b>SEM</b>
<i>P. aeruginosa</i> PA01	28.67	27.86	29.81	-	28.78	0.98	0.57
<i>S. epidermidis</i> ATCC35984	28.77	32.62	31.21	-	30.87	1.95	1.12
<i>K. pneumoniae</i> 280	26.09	31.22	27.96	-	28.42	2.60	1.50
<i>E. faecalis</i> ATCC33186	38.17	32.50	22.95	-	31.21	7.69	4.44
<i>P. mirabilis</i> 296	18.85	17.40	15.63	22.96	18.71	3.12	1.56
<i>S. aureus</i> USA300	37.37	32.56	18.61	-	29.51	9.74	5.63
<i>S. aureus</i> Newman	8.46	17.78	12.48	-	12.91	4.67	2.70
<i>L. gasseri</i> ATCC33323	75.48	84.21	55.97	57.97	68.41	13.70	6.85
<i>L. reuteri</i> RC-14	26.75	26.89	24.65	-	26.10	1.25	0.72
<i>L. rhamnosus</i> GR-1	41.17	44.75	46.96	-	44.29	2.92	1.69

<b>R1 Relaxation Rate (s<sup>-1</sup>)</b>					<b>Mean</b>	<b>SD</b>	<b>SEM</b>
<i>P. aeruginosa</i> PA01	0.63	1.22	1.17	1.15	1.04	0.27	0.14
<i>S. epidermidis</i> ATCC35984	1.38	1.46	1.43	1.69	1.49	0.14	0.07
<i>K. pneumoniae</i> 280	1.26	1.25	1.25	-	1.25	0.01	0.00
<i>E. faecalis</i> ATCC33186	1.87	2.21	2.04	-	2.04	0.17	0.10
<i>P. mirabilis</i> 296	0.83	0.92	1.02	-	0.92	0.09	0.05
<i>S. aureus</i> USA300	1.49	1.46	1.17	-	1.37	0.18	0.10
<i>S. aureus</i> Newman	1.47	0.76	1.34	1.12	1.17	0.31	0.15
<i>L. gasseri</i> ATCC33323	2.80	4.59	3.31	2.93	3.34	0.72	0.32
<i>L. reuteri</i> RC-14	2.65	2.64	2.50	-	2.60	0.08	0.05
<i>L. rhamnosus</i> GR-1	1.80	4.38	4.43	4.47	3.77	1.31	0.66

**Appendix 13. ICP-MS iron and manganese content of various bacterial species**

<b>Fe content (µg Fe / mg protein)</b>				<b>Mean ^</b>	<b>SD</b>	<b>SEM</b>
<i>P. aeruginosa</i> PA01	0.673	0.632	0.646	0.650	0.021	0.012
<i>S. epidermidis</i> ATCC35984	0.675	1.728	0.821	1.075	0.570	0.329
<i>K. pneumoniae</i> 280	1.271	0.691	2.005	1.322	0.659	0.380
<i>E. faecalis</i> ATCC33186	0.192	0.239	0.332	0.254	0.071	0.041
<i>P. mirabilis</i> 296	1.541	0.706	0.341	0.863	0.615	0.355
<i>S. aureus</i> USA300	1.622	0.822	0.746	1.063	0.485	0.280
<i>S. aureus</i> Newman	2.052	1.419	2.206	1.892	0.417	0.241

^ Median is displayed for samples where n < 3.

<b>Mn content (<math>\mu\text{g Mn} / \text{mg protein}</math>)</b>				<b>Mean</b>	<b>SD</b>	<b>SEM</b>
<i>P. aeruginosa</i> PA01	0.027	0.024	0.035	0.029	0.006	0.003
<i>S. epidermidis</i> ATCC35984	0.064	0.188	0.258	0.170	0.098	0.057
<i>K. pneumoniae</i> 280	0.030	0.027	0.034	0.030	0.004	0.002
<i>E. faecalis</i> ATCC33186	0.041	0.681	0.688	0.470	0.372	0.215
<i>P. mirabilis</i> 296	0.018	0.014	0.003	0.012	0.008	0.004
<i>S. aureus</i> USA300	0.196	0.075	0.149	0.140	0.061	0.035
<i>S. aureus</i> Newman	0.217	0.286	0.371	0.291	0.077	0.045
<i>L. gasseri</i> ATCC33323	0.140	1.345	1.720	1.068	0.826	0.477
<i>L. reuteri</i> RC-14	20.21	16.93	18.91	18.68	1.652	0.954
<i>L. rhamnosus</i> GR-1	71.16	43.26	45.37	53.26	15.54	8.969
<i>L. crispatus</i> ATCC33820	44.99	33.45	111.9	63.45	42.36	24.46

**Appendix 14. Transverse and longitudinal relaxation rates of *L. crispatus* ATCC33820 diluted in gelatin**

<b>Fraction of <i>L. crispatus</i></b>	<b>R2 Relaxation Rate (s<sup>-1</sup>)</b>					<b>Mean ^</b>	<b>SD</b>	<b>SEM</b>
1/2	183.4	174.0	169.5	134.2	143.3	160.9	21.06	9.42
1/4	94.00	91.81	91.31	68.25	50.31	79.14	19.23	8.60
1/8	49.90	48.13	50.06	53.66	43.13	48.98	3.84	1.72
1/16	25.45	25.28	26.21	37.21	30.36	28.90	5.09	2.27
1/32	19.95	20.06	-	-	-	20.01	-	-

^ Median is displayed for samples where n < 3.

<b>Fraction of <i>L. crispatus</i></b>	<b>R2* Relaxation Rate (s<sup>-1</sup>)</b>					<b>Mean ^</b>	<b>SD</b>	<b>SEM</b>
1/2	173.4	223.6	195.0	142.9	165.2	180.02	30.68	13.72
1/4	102.4	95.78	90.30	106.4	61.59	91.29	17.71	7.92
1/8	47.56	48.87	52.41	67.24	57.43	54.70	7.98	3.57
1/16	42.74	34.52	42.71	43.81	40.62	40.88	3.74	1.67
1/32	25.67	26.15	-	-	-	25.91	-	-

^ Median is displayed for samples where n < 3.

<b>Fraction of <i>L. crispatus</i></b>	<b>R1 Relaxation Rate (s<sup>-1</sup>)</b>					<b>Mean</b>	<b>SD</b>	<b>SEM</b>
1/2	3.14	3.62	4.33	3.86	-	3.74	0.50	0.25
1/4	4.09	4.16	4.41	3.55	4.07	4.06	0.31	0.14
1/8	3.63	3.29	3.11	3	3.05	3.22	0.26	0.11
1/16	1.93	2.01	2.11	1.91	1.74	1.94	0.14	0.06

**Appendix 15. Transverse relaxation rates of *L. crispatus* ATCC33820 diluted in 5637 bladder cells**

<b>Fraction of <i>L. crispatus</i></b>	<b>Fraction of 5637 cells</b>	<b>R2 Relaxation Rate (s<sup>-1</sup>)</b>		<b>Median</b>
1/2	1/2	70.05	76.39	73.22
1/4	3/4	52.81	-	52.81
1/8	7/8	39.33	43.17	41.25
1/16	15/16	32.58	21.66	27.12
-	1/1 (100% 5637 cells)	16.32	9.22	12.77

<b>Fraction of <i>L. crispatus</i></b>	<b>Fraction of 5637 cells</b>	<b>R2* Relaxation Rate (s<sup>-1</sup>)</b>		<b>Median</b>
1/2	1/2	156.5	182.6	169.6
1/4	3/4	97.21	-	97.21
1/8	7/8	73.59	82.26	77.92
1/16	15/16	67.70	75.84	71.77
-	1/1 (100% 5637 cells)	18.38	25.64	22.01



<b>Fraction of <i>L. crispatus</i></b>	<b>Fraction of 5637 cells</b>	<b>R2' Relaxation Rate (s<sup>-1</sup>)</b>		<b>Median</b>
1/2	1/2	86.45	106.21	96.33
1/4	3/4	44.4	-	44.4
1/8	7/8	34.26	39.09	36.68
1/16	15/16	35.12	54.18	44.65
-	1/1 (100% 5637 cells)	2.06	16.42	9.24

**Appendix 16. Transverse and longitudinal relaxation rates of *S. aureus* USA300 iron acquisition and storage mutants in iron-replete and iron-deplete growth conditions**

<i>S. aureus</i> USA300 mutants	Iron conditions †	R2 Relaxation Rate (s <sup>-1</sup> )			Mean ^	SD	SEM
WT	High	31.93	29.70	16.40	26.01	8.40	4.85
WT	Low	36.17	17.29	19.25	24.24	10.38	5.99
$\Delta sfa/\Delta sbn$	High	27.41	28.20	-	27.80	-	-
$\Delta sfa/\Delta sbn$	Low	22.41	18.67	18.45	19.84	2.23	1.28
$\Delta sfa/\Delta sbn/\Delta ftnA$	High	25.63	25.93	-	25.78	-	-
$\Delta sfa/\Delta sbn/\Delta ftnA$	Low	21.38	21.12	20.31	20.94	0.56	0.32

^ Median is displayed for samples where n < 3.

<i>S. aureus</i> USA300 mutants	Iron conditions †	R2* Relaxation Rate (s <sup>-1</sup> )			Mean ^	SD	SEM
WT	High	37.37	32.56	18.61	29.51	9.74	5.63
WT	Low	42.60	18.67	20.64	27.30	13.28	7.67
$\Delta sfa/\Delta sbn$	High	28.23	29.02	-	28.63	-	-
$\Delta sfa/\Delta sbn$	Low	25.19	18.16	18.96	20.77	3.85	2.22
$\Delta sfa/\Delta sbn/\Delta ftnA$	High	25.43	26.73	-	26.08	-	-
$\Delta sfa/\Delta sbn/\Delta ftnA$	Low	21.37	22.18	21.18	21.58	0.53	0.31

^ Median is displayed for samples where n < 3.

<i>S. aureus</i> USA300 mutants	Iron conditions †	R1 Relaxation Rate (s <sup>-1</sup> )			Mean ^	SD	SEM
WT	High	1.49	1.46	1.17	1.37	0.18	0.10
WT	Low	1.34	1.13	1.18	1.22	0.11	0.06
$\Delta sfa/\Delta sbn$	High	1.46	1.44	-	1.45	-	-
$\Delta sfa/\Delta sbn$	Low	1.31	1.15	1.14	1.20	0.10	0.06
$\Delta sfa/\Delta sbn/\Delta ftnA$	High	1.40	1.36	-	1.38	-	-
$\Delta sfa/\Delta sbn/\Delta ftnA$	Low	1.31	1.34	1.32	1.32	0.02	0.01

^ Median is displayed for samples where n < 3.

**Appendix 17. ICP-MS iron and manganese content of *S. aureus* USA300 iron acquisition and storage mutants in iron-replete and iron-deplete growth conditions**

<i>S. aureus</i> USA300 mutants	Iron conditions †	Fe content (µg Fe / mg protein)			Mean ^	SD	SEM
WT	High	1.622	0.822	0.746	1.063	0.485	0.280
WT	Low	0.213	-	-	0.213	-	-
$\Delta sfa/\Delta sbn$	High	0.990	-	-	0.990	-	-
$\Delta sfa/\Delta sbn$	Low	0.217	0.220	-	0.218	-	-
$\Delta sfa/\Delta sbn/\Delta ftnA$	High	0.789	-	-	0.789	-	-
$\Delta sfa/\Delta sbn/\Delta ftnA$	Low	0.083	0.302	-	0.192	-	-

^ Median is displayed for samples where n < 3.

<i>S. aureus</i> USA300 mutants	Iron conditions †	Mn content (µg Mn / mg protein)			Mean ^	SD	SEM
WT	High	0.196	0.075	0.149	0.140	0.061	0.035
WT	Low	0.072	-	-	0.072	-	-
$\Delta sfa/\Delta sbn$	High	0.096	-	-	0.096	-	-
$\Delta sfa/\Delta sbn$	Low	0.048	0.077	-	0.062	-	-
$\Delta sfa/\Delta sbn/\Delta ftnA$	High	0.093	-	-	0.093	-	-
$\Delta sfa/\Delta sbn/\Delta ftnA$	Low	0.010	0.120	-	0.065	-	-

^ Median is displayed for samples where n < 3.

# Curriculum Vitae

**Sarah Catherine Donnelly**

## **Education**

2013 – 2017 Honours Specialization in Interdisciplinary Medical Science  
Western University, London, ON, Canada  
4-year Honors Bachelor of Medical Science (BMSc) Degree

2017 – 2020 Microbiology and Immunology  
Collaborative Molecular Imaging Program  
Western University, London, ON, Canada  
Master of Science (MSc) Degree

## **Research Experience**

Feb 2013 – June 2013 Partners in Experiential Learning Co-operative Education  
(PEL Co-op) student, Medical Biophysics, Goldhawk lab,  
Lawson Health Research Institute, London, ON

- Co-op placement for 30 hours / week
- Assisted graduate student with molecular cloning, electrophoresis
- Produced a plasmid for reporter gene expression of *magA* to visualize cellular and molecular activity by MR contrast
- Attended weekly Medical Biophysics Graduate student seminars

July 2013 – Sep 2014 Volunteer Research Assistant, Medical Biophysics,  
Goldhawk lab, Lawson Health Research Institute,  
London, ON

- Volunteered 30 hours / week during summer, 5 hours / week during school year
- Solution making, protein assays, cell culture, co-immunoprecipitations
- Prepared MR gelatin phantoms containing cell samples for contrast signal measurements, and analyzed this data

- May 2015 – Sep 2015      Summer Student, Medical Biophysics, Goldhawk lab,  
Lawson Health Research Institute, London, ON
- Paid position for 35 hours / week
  - Cell culture of multiple cell lines and collected lysates for inductively coupled plasma mass spectrometry (ICP-MS) analysis, protein assays
  - MR phantom preparation and analysis
- May 2016 – Aug 2016      Summer Student, Medical Biophysics, Goldhawk lab,  
Lawson Health Research Institute, London, ON
- Paid position for 30 hours / week
  - Cell culture of multiple cell types
  - MR phantom preparation and analysis
  - PCR of bacterial genomic DNA followed by subcloning
  - Transfection and fluorescence microscopy
- Sep 2017 – Present      Graduate Student, Microbiology and Immunology,  
Western University, Burton and Goldhawk labs,  
Lawson Health Research Institute, London, ON
- Full-time paid position
  - Bacterial cell culture and cloning for applications in detecting bacteria *in vivo* using MRI
  - MR phantom preparation and analysis
  - Attended weekly seminars

## **Work Experience**

- 2009 – 2017      Waitress, Shanghai Restaurant, London, ON
- Working as a team, training new employees, interacting with customers
  - Time management

## **Publications**

Liu L, Alizadeh K, **Donnelly SC**, Dassanayake P, Hou TT, McGirr R, Thompson RT, Prato FS, Gelman N, Hoffman L, Goldhawk DE. (2019) MagA expression attenuates iron export activity in undifferentiated multipotent P19 cells. PLoS ONE 14(6): e0217842.

## **Presentations and Abstracts**

**Donnelly S.** My PEL co-op experience. 10<sup>th</sup> Annual CIHR/CaRTT Department of Oncology Research and Education Day; 2013 June 21; London, ON, Oral Presentation.

Alizadeh K, McGuire T, **Donnelly S**, Liu L, Thompson T, Prato F, Hoffman L, Gelman N, and Goldhawk D. MagA-derived MR contrast persists despite cellular differences in iron metabolism; 14<sup>th</sup> Annual Imaging Network of Ontario Symposium; 2016 March 30-31; Toronto, ON. Poster.

Alizadeh K, McGuire T, **Donnelly S**, Liu L, Thompson T, Prato F, Hoffman L, Gelman N, and Goldhawk D. MagA-derived MR contrast persists despite cellular differences in iron metabolism; London Health Research Day; 2016 March 29; London, ON. Poster.

Alizadeh K, **Donnelly SC**, McGuire T, Thompson RT, Prato FS, Gelman N, and Goldhawk DE. Influence of hepcidin on magnetic resonance contrast in P19 cells; 9<sup>th</sup> Annual Meeting of the World Molecular Imaging Congress; 2016 September 7-10; New York, NY. Poster.

Sun Q, **Donnelly SC**, and Goldhawk DE. Using the magnetosome to model gene-based iron contrast for magnetic resonance imaging; 5<sup>th</sup> International Magnetotactic Bacteria Meeting; 2016 September 11-15; Marseille, France. Poster.

Sun Q, **Donnelly SC**, Prato, FS, and Goldhawk DE. Using magnetosome genes for MRI reporter gene expression; 32<sup>nd</sup> International Union of Radio Science General Assembly & Scientific Symposium; 2017 August 19-26; Montreal, QC. Oral Presentation by Goldhawk DE.

**Donnelly SC**, Thompson RT, Prato FS, Gelman N, Burton JP and Goldhawk DE. Magnetic resonance imaging of the microbiome using MagA-expressing bacteria; Lawson's Talks on Fridays; 2018 March 16; London, ON. Oral Presentation by Donnelly SC.

**Donnelly SC**, Thompson RT, Prato FS, Gelman N, Burton JP and Goldhawk DE. Magnetic resonance imaging of the microbiome using MagA-expressing bacteria; 16<sup>th</sup> Annual Imaging Network of Ontario Symposium; 2018 March 28-29; Toronto, ON. Oral Presentation by Donnelly SC.

**Donnelly SC**, Thompson RT, Prato FS, Gelman N, Burton JP and Goldhawk DE. Magnetic resonance imaging of the microbiome using MagA-expressing *Escherichia coli*; 2<sup>nd</sup> Annual Cellular and Molecular Imaging Symposium; 2018 May 1; London, ON. Poster.

**Donnelly SC**, Thompson RT, Prato FS, Gelman N, Burton JP and Goldhawk DE. Magnetic resonance imaging of the microbiome using MagA-expressing *Escherichia coli*; London Health Research Day; 2018 May 10; London, ON. Poster.

**Donnelly SC**, Thompson RT, Prato FS, Gelman N, Burton JP and Goldhawk DE. Magnetic resonance imaging of microbiome *in vitro* using MagA-expressing *Escherichia coli*; 11<sup>th</sup> Annual Meeting of the World Molecular Imaging Congress; 2018 September 12-15; Seattle, WA, USA. Poster.

**Donnelly SC**, Thompson RT, Prato FS, Gelman N, Burton JP and Goldhawk DE. Characterization of clinical bacterial isolates using magnetic resonance imaging and potential for contrast enhancement with MagA expression; Lawson's Talks on Fridays; 2019 January 11; London, ON. Oral Presentation by Donnelly SC.

**Donnelly SC**, Thompson RT, Prato FS, Gelman N, Burton JP and Goldhawk DE. Magnetic resonance imaging of commensal and pathogenic bacteria; 17<sup>th</sup> Annual Imaging Network of Ontario Symposium; 2019 March 27-28; London, ON. Poster.

**Donnelly SC**, Thompson RT, Prato FS, Gelman N, Burton JP and Goldhawk DE. Magnetic resonance imaging of commensal and pathogenic bacteria with potential for contrast enhancement; London Health Research Day; 2019 April 30; London, ON. Poster.

**Donnelly SC**, Thompson RT, Prato FS, Gelman N, Goldhawk DE and Burton JP. Using magnetic resonance imaging to visualize probiotic and urogenital bacteria; 2019 International



Scientific Association of Probiotics and Prebiotics Annual Meeting; 2019 May 14-16; Antwerp, Belgium. Poster.

## **Patents**

Goldhawk D, Burton J, Silverman M, Prato F, **Donnelly SC**, Thompson RT, Foster S, and Zhang M. 2020. Biomedical Imaging of Bacteria and Viruses. U.S. Provisional Patent # L-21-002, filed on April 28<sup>th</sup>, 2020.

## **Awards and Honours**

- Dean's Honor List 2016
- Dean's Honor List 2017
- Western Graduate Research Scholarship 2017-2018 (\$1000)
- Western Graduate Research Scholarship 2018-2019 (\$3000)
- FW Luney Entrance Scholarship 2017 (\$2000)
- Lawson Internal Research Fund Studentship 2017 (\$15,000)
- Dr. FW Luney Graduate Travel Award in Microbiology & Immunology (\$2000)
- Molecular Imaging program travel award 2018 (\$450)
- Microbiome and Probiotic Research Student Award (\$12,125)
- International Scientific Association for Probiotics and Prebiotics Students and Fellows Association travel award (\$450 USD)
- Molecular Imaging program travel award 2019 (\$300)
- International Scientific Association for Probiotics and Prebiotics Students and Fellows Association Outstanding Poster Award (\$100 USD)